UiT
THE ARCTIC
UNIVERSITY
OF NORWAY

Faculty of Science and Technology
Department of Mathematics and Statistics

A Complex Contour based Perfectly Matched Layer applied to a Pattern Generating Model Equation.

—

Amund Jenssen

MAT -3900 Master thesis in Applied Mathematics, February 2017

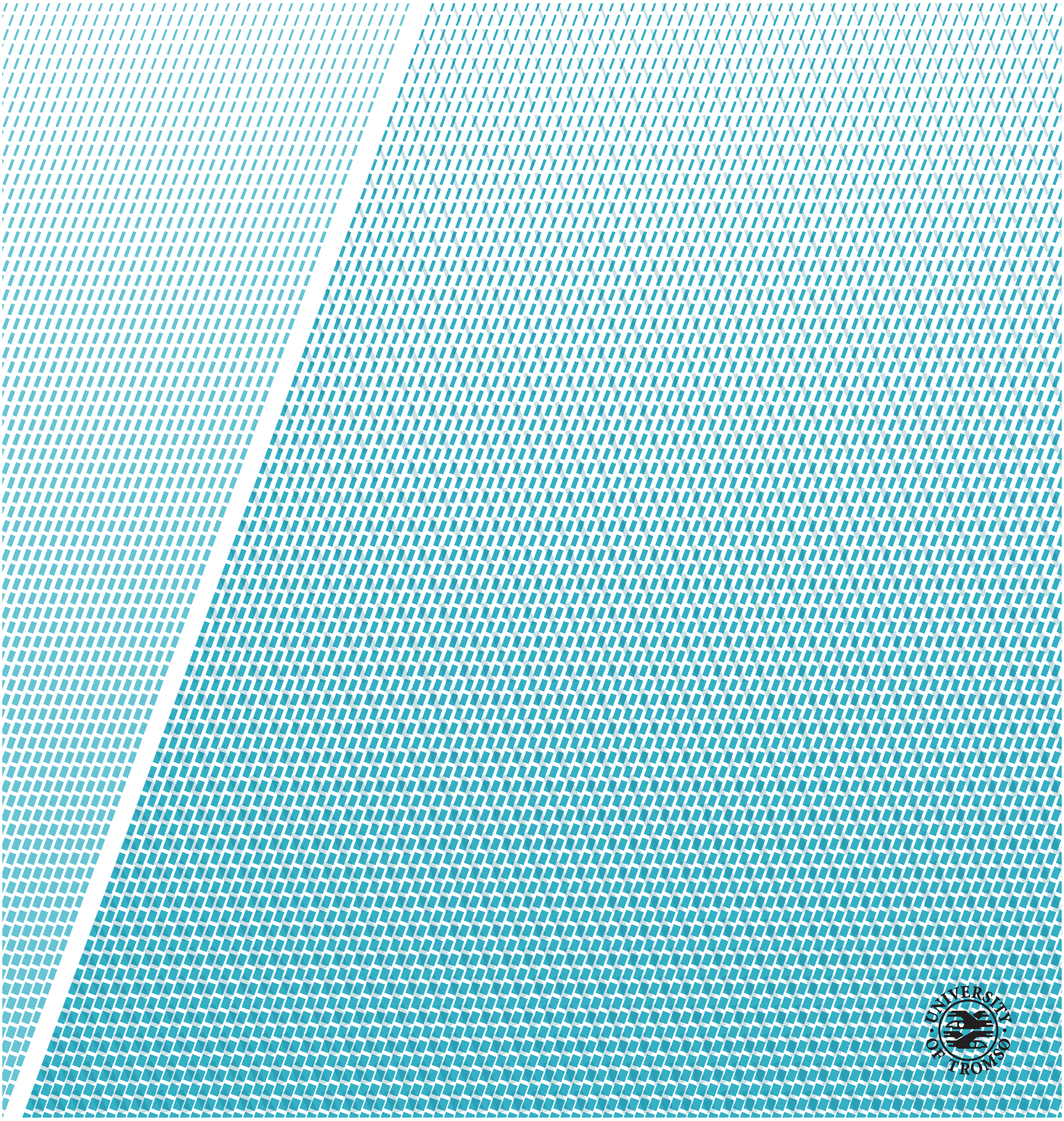

This thesis document was typeset using the *UiT Thesis LaTeX Template*.

To Galina and Roy.

Only one of you were right.

“They read all the books, but they can’t find the answers.”
–John Mayer

Abstract

The observable universe consists of several non equilibrium systems that generate spatiotemporal behaviour in the form of various patterns. As the elementary laws of physics and chemistry are unable to explain the pattern forming behaviour of such systems, scientists have turned to desktop experiments and model equations to gain further insight. The model equations that generate numerical solutions similar to real world systems are computationally intensive, and this thesis discusses the possibility of designing a numerical scheme which are to reduce the computation time for a specific model equation.

The design is based on the perfectly matched layer (PML), a mathematical-numerical technique that works as an artificial absorbing layer within the discretized grid boundaries.

The thesis discuss how to impose a PML version of the model equation into the numerical method of lines(MOL) procedure, and various numerical and mathematical techniques are discussed in order to build this scheme.

The numerical simulations for the PML-equation fail to produce the correct spatiotemporal behaviour, and the discussed analysis states that a PML does not apply to the model equation discussed in the thesis.

Acknowledgements

I would like to thank my supervisor, Professor Per Kristen Jakobsen for his great advice, ideas, patience, and very much appreciated input throughout this thesis project. Our discussions have been very inspirational, and your way of thinking has made me a better man of science. The thesis project would not have been realized without you and your expertise.

To my many brothers and sisters in arms at the scientific department, thanks for all the relevant and irrelevant discussions, laughs, advice, and tea breaks throughout the years. Those of you that have been around the last year should know that your appearance have been of great importance to me, and that the office hours would have been utterly dull without you. Some of you have contributed to the thesis project with discussions and direct input concerning mathematics, physics, programming, TeX-support and proof reading, and for that I am sincerely grateful. No one mentioned, no one forgotten, but you know who you are.

To my family: your continuous support has been utmost appreciated.

Friends and loved ones, I look forward to see you all again after this mind boggling time consuming months of work.

Contents

List of Figures

List of Tables

List of Listings

List of Abbreviations

BDM backward difference method

CDM center difference method

cPMLSHE constant perfectly matched layer version of the Swift - Hohenberg equation

DFT discrete Fourier transform

FDM forward difference method

GLE Ginzburg - Landau equation

IDFT inverse discrete Fourier transform

MOL method of lines

ODE ordinary differential equation

PDE partial differential equation

PML perfectly matched layer

PMLSHE perfectly matched layer version of the Swift - Hohenberg equation

rSE reduced Schrödinger equation

SHE	Swift - Hohenberg equation
SODM	system operator differential matrix

1

Introduction

When we look at the surrounding universe and its diverse components ranging from large galaxies to smaller structures within our own terrestrial spheres, the number of apparent patterns are in many ways striking. Several physical systems have a tendency to generate patterns seemingly out of nowhere, and many of them are filled with interesting underlying features. The spiralling arms of a galaxy, the similar stripes and spots on animals, and the crystalline structure of snowflakes are just a few examples of such appearing patterns.

Where people throughout history have wondered "why is there *something*?", the study of natural patterns concerns the question "why does the *something* look and behave like it does?". The elementary laws of physics and chemistry does neither describe the appearing pattern forming structures, or the similarity between many of them. For example, we might wonder: why does zebra stripes resemble ripples in desert sand, or how can Jupiter's stormy "Red Eye" coexist together with the highly turbulent striped flow in its atmosphere? Such unanswered questions have led to a branch of science which includes fields within mathematics, physics and computation, where the aim is to investigate pattern forming systems.

The stated intrinsic pattern feature of mother nature, and the desire to understand its realisation mechanisms, constitutes the overall theme for this thesis. To introduce the field of pattern formation, we take the tour from observable to experimental patterns, which in turn leads to model equations of pattern forming systems. Note that the presented material in section 1.1 through 1.3 is similarly discussed in Cross and Greenside[1].

1.1 Natural patterns

As scientists we are driven by questioning the observable universe. To be able to answer questions regarding "the why" of natural pattern formation, we must specify the interesting features of real world patterns. We will therefore consider three systems on very different spatial scales, where we are to highlight some characteristics and relevant questions.

Figure 1.1 illustrates the 30 million light years distant M51 galaxy, where the appearing pattern is defined by two large spiralling arms. The spirals are slowly whirling around its gravitational center with a certain rotational frequency and pitch. The underlying cause for those features are not known, but they must have a corresponding explanation. Why some galaxies develop such spiralling patterns is poorly understood, and it is to date an open question within the field of astronomy.

The striped pattern in figure 1.2 describes the approximately periodic ripples found in some terrestrial environments covered by water or air. Such patterns appear on sand dunes or at the beach, and the driving mechanisms for those patterns are readily understood as driven-dissipative systems. However, the stripes do not have a well defined average wavelength, and the wavelength

Figure 1.1: The M51 galaxy with spiralling arms(from the national optical astronomy observatory - NOAH).

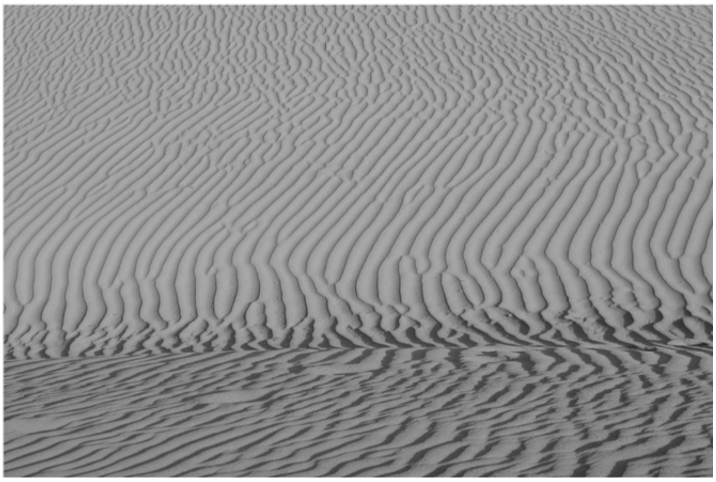

Figure 1.2: Striped pattern in desert sand dunes(from [1]).

is observed to slowly grow with time. The latter is exemplified by the Martian sand dunes in figure 1.3, where kilometre long wavelengths have been observed.

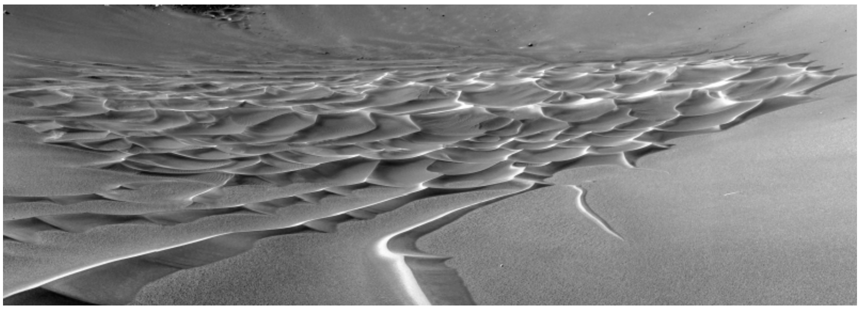

Figure 1.3: Sand dunes on Mars(from NASA).

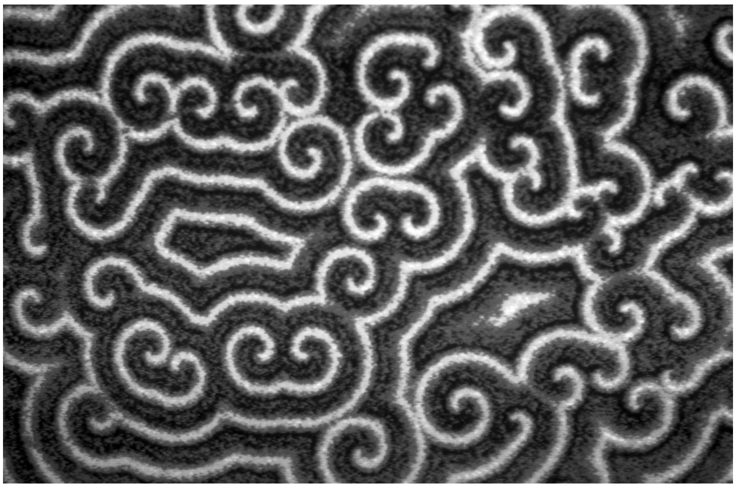

Figure 1.4: A slime mold colony named Dictyostelium discoideum(from [1]).

Figure 1.4 depicts a snapshot of an aggregation state for a starving slime-mold colony found on various forest floors. The lighter regions corresponds to elongated cells that moves with a speed of approximately 10 $\mu m/s$, while the darker regions show stationary cells. A secrete is leaked into the system as a consequence of the starvation, which in turn triggers the organism to generate the chaotic pattern of propagating spiralling waves. Chemical gradients are shown to be the driving force of the system, and we argue that the interesting features are the frequencies and velocities of the spiralling waves, and how they vary with different system states.

The systems illustrated on the previous pages are systems which are driven by the ever expanding universe and its continuous non equilibrium state, where patterns emerge as a response to the everlasting drive. Systems with pattern forming nature must therefore be defined and analysed in terms of non equilibrium dynamics, and to be able to understand and usefully investigate such systems we turn to controllable desktop experiments.

1.2 Desktop experiments

We will in this section present patterns generated from desktop experiments, but to establish a precise vocabulary for our forthcoming observations and investigations, we will begin by exploring a controllable non equilibrium system: a Rayleigh-Bénard convection experiment.

1.2.1 Rayleigh-Benard convection

Figure 1.5a outlines the concept of a Rayleigh-Bénard convection experiment, which in short is nothing more than a special squared box filled with some fluid. The horizontal plates consists of a heat conducting material rigged to take on different temperatures T_1^{warm} and T_2^{cold}, and all side walls are made from a substance with poor conductivity. $\Delta T = T_1 - T_2$ denotes the temperature difference between the conducting plates, and the initial state of the system is given by $\Delta T = 0$ and thermodynamic equilibrium. The lateral width of the horizontal plates is denoted L, and the relation $L >> d$ dictates the internal height d.

This setup allows us to drive the system out of equilibrium by increasing T_1 to a fixed value $T_1^* > T_1$, such that $\Delta T > 0$ remains the same throughout the experiment. Small parcels of fluid near the bottom plate will then expand and decrease in density as they gain energy from the hot plate, while the contrary applies to parcels of fluid at the cold top plate. Buoyancy forces will then come into play and accelerate the less dense warm parcels upwards in the fluid, while the denser cold parcels move downwards. This behaviour is

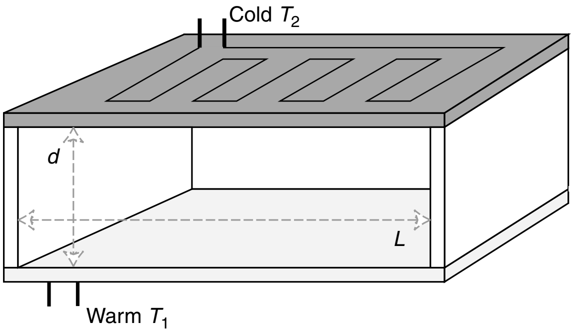

(a) A Rayleigh-Benard convection apparatus.

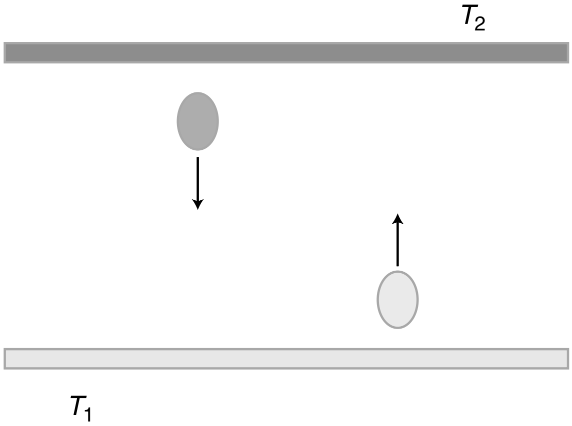

(b) Small parcels inside the Rayleigh-Benard experiment box .

Figure 1.5: Rayleigh-Benard convection(from [1]).

illustrated in figure 1.5b.

However, the buoyancy induced acceleration is opposed by both the friction from the fluid viscosity, and heat diffusion between warm and cold regions of the fluid. The system might therefore stall in this slightly tuned state, without generating spatiotemporal behaviour. On the other hand, if ΔT is larger that some critical value ΔT_c, the buoyancy forces may overcome the dissipative effects, such that the parcels are free to move, and the system may generate spatiotemporal dynamics.

It turns out that the Rayleigh-Benard convection experiment is able to produce a wide range of patterns depending on certain physical parameters like the box height d, the initial temperature T_1, the viscosity, and the thermal expansion coefficient of the fluid. We will not discuss these in details here, but in general it is possible to express the system state with the single parameter relation

$$r(\Delta T) = \beta \Delta T \, , \tag{1.1}$$

where β is a dimensionless constant that contains the stated physical properties. Hence, the behaviour of the entire system varies linearly with ΔT, which we are able to control at any time.

As a side note we remark that patterns generated in a Rayleigh-Benard convection experiment are visualized through an advanced scientific shadow play named shadowgraphy, which involves a transparent top plate, a mirroring bottom plate, a camera, LED lights and a complex composition of lenses.

The presented experiment illustrates the three main features of many pattern forming non equilibrium systems:

- The system state is determined from a single dimensionless parameter r, which we refer to as the control parameter.

- The system generates interesting non equilibrium behaviour when $r > r_c$, where r_c is defined as the critical parameter value.

- The spatial extent of the system is large compared to the interesting characteristics generated during non equilibrium.

1.2.2 Experimental patterns

To illustrate the wide range of pattern forming desktop experiments, we introduce three different systems by presenting snapshot pictures of the patterns formed under certain conditions. We discuss each experiment briefly, but we will not emphasise details and underlying causes for each case.

Figure 1.6a depicts a disordered many-spiralled state of a chemical Belusov-Zhabotinsky experiment in a Petri-like dish. The pattern is a result of an excitable reaction of two chemical reagents in a shallow layer of fluid, where the patterns becomes time independent after a transient state.

In figure 1.6b the striped state of a so called granular crispation experiment is illustrated. The experiment consists of a box filled with a granular media which contains thousands of tiny brass balls, where a varying frequency is shaking the box in the vertical direction. When the shaking amplitude is sufficiently large, the granular material is thrown into the air with different velocities, while the bottom plate moves upwards. Since the balls have different velocities, some will hit the bottom plate while others are up in the air. This process can be rigged to result in an alternating pattern, in which peaks and valleys of balls formed in one cycle, becomes valleys and peaks at the next cycle.

Figure 1.6c illustrates a rotating three spiralled state of a Rayleigh-Benard convection experiment, where the white and dark regions corresponds to descending colder, and rising warm fluid respectively. Note that the spirals terminate long before they reach the lateral wall by merging into three topological defects, which is refferd to as dislocations.

As a remark we point out the single parameter that controls the outcome of the non linear dynamics for each experiment:

- The Belusov-Zhabotinsky reaction is controlled by one of the reagents, such that one is placed in the Petri dish, while the other is added afterwards.

- The crispation experiment is controlled by varying the shaking frequency.

- The Rayleigh-Benard convection experiment is controlled by ΔT.

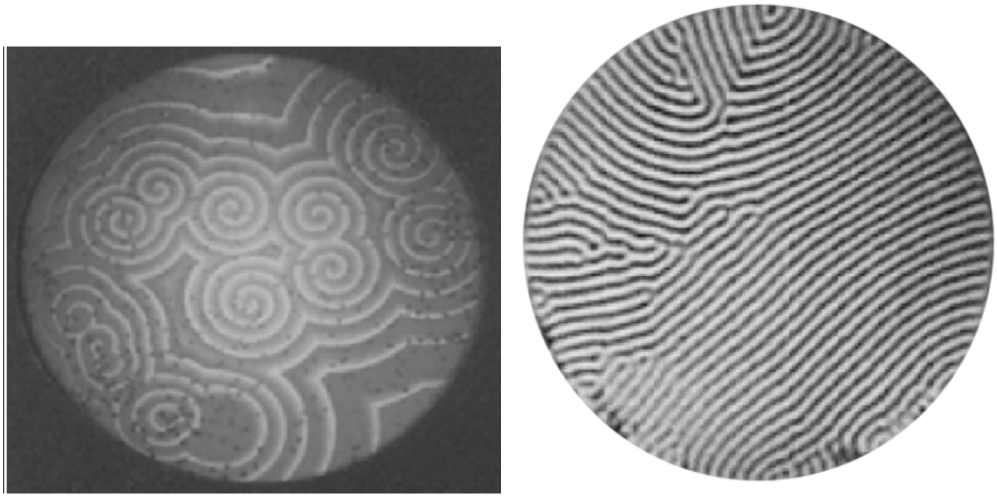

(a) Spiral state of a Belusov- Zhabotinsky excitable reaction.

(b) Stripes in a granular crispation experiment.

(c) Three armed spiral pattern from Rayleigh-Benard convection.

Figure 1.6: Experimentally generated patterns (from [1]).

1.3 Modelling patterns

As illustrated in the previous sections, non equilibrium systems with a pattern forming behaviour are very complex, even though their nature depends on a single controllable parameter. However, non equilibrium systems varies in space and time, and within the fields of mathematics and physics spatiotemporal varying behaviour is described by partial differential equations. It is therefore possible to model real life non linear systems by those equations, in order to investigate them from a theoretical point of view. The equations that models patten forming systems are visually very different, but many of them are derived from fluid-similar equations, or from a derivation where oscillatory solutions are assumed.

We will therefore introduce two pattern forming model equations, and illustrate numerical solutions of those equations.

The general SHE reads

$$u_t = ru - (1 + \nabla^2)^2 u + N(u) \tag{1.2}$$

where where $N(u)$ is some nonlinear term, r the control parameter, and $u = u(x, y, z, t)$ is a scalar field. A striped state solution of the SHE is presented in figure 1.7a, and we remark the similarity between the numerical solution and the real life systems 1.6b and 1.2.

A variant of the the complex Ginzburg - Landau equation (GLE) is given by the formula

$$\overline{A}_t = (1 - ic_3)A + \nabla^2 A - (1 - ic_1)|A|^2 A \tag{1.3}$$

where $A = (x, y, t)$ defines a complex field. Both c_1 and c_3 are control parameters. Figure 1.7b and 1.7c depicts the numerical solutions, and by comparison with the previously presented natural and desktop patterns in figure 1.1, 1.4 and 1.6, we observe that the complex GLE is well suited to model real life systems.

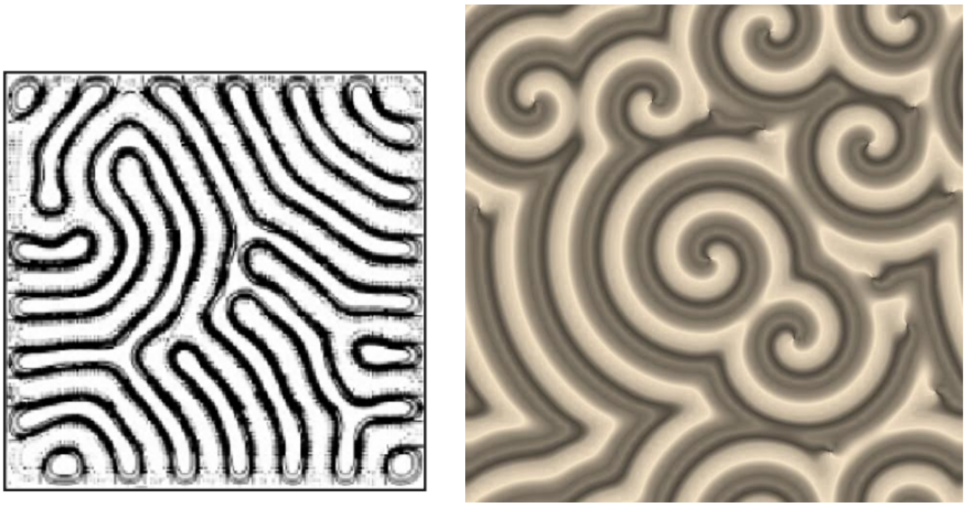

(a) Striped solutions of the SHE (from [1]).

(b) Tied spiral solution of GLE (from umd.edu).

(c) Single spiral solution of the GLE (from [1]).

Figure 1.7: Experimentally generated patterns.

1.4 The Perfectly Matched Layer

Whenever one tries to solve partial differential equation (PDE)s numerically by some discretization, one must truncate the computational grid. This leads to the possible problem of boundary reflections, and if such phenomena occurs, we are always in need of a way to minimize or eliminate the boundary and reflectory effects. While some PDEs have a behaviour where one can apply periodic or zero boundary conditions, or use a sufficently large grid if the solution decays rapidly in space, problems which involves waves and oscillatory solutions demands a more advanced approach to eliminate such effects. A way to get around this issue is by the perfectly matched layer (PML), a numerical method that acts as an absorbing layer within the discretized grid boundaries. Figure 1.8 [5] illustrates the overall idea of an absorbing layer in two dimensions.

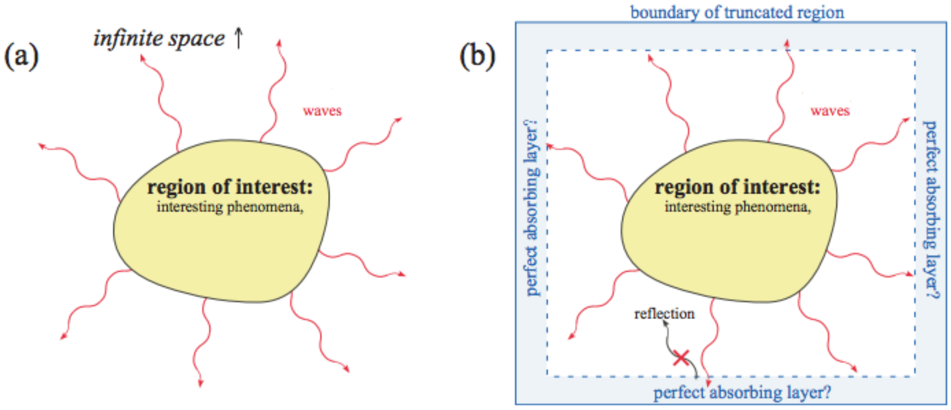

Figure 1.8: A perfectly matched layer in two dimensions.

A real world example of a PML might be a room with so called "absorbing walls". Such walls can be found in recording studios and consists of geometrical structures that are designed to "capture" incoming sound waves. When trapped, the sound waves bounces back and forth within the geometric structures, and never re-enters the room. A slightly less physical example of the PML analogous to figure 1.8 is to imagine a very large pool where pebbles are thrown into the center with a varying frequency, where our intention is to study the wavy pattern around the center. The region of interest is in this case around the center, while the reflecting boundary waves from the pool edges are the problem we want to eliminate. To solve this we insert a "mystical frame" inside the pool edges that "absorb and flattens" the wave fronts as they hit the frame, such that one may study the center region without interference from disturbing waves.

Although this illustration is highly unphysical, it is possible to handle this concept mathematically. In short, we manipulate our initial problem with some complex analysis to formulate a new problem, where the real and physical part of the solution is "zeroed out" at the PML.

1.5 Motivation and outline

1.5.1 Motivation

The objective of this thesis is to apply a complex contour based PML to a pattern generating PDE, and to argue why it is relevant and useful to endeavour this, we present the following arguments:

As briefly stated in section 1.3, model equations like the SHE or the GLE are PDEs designed to possess a oscillatory nature in order to imitate pattern forming systems. Alternatively, model equations may be a result of some mathematical procedure applied to other physical models with spatiotemporal fluid-like dynamical behaviour. In that manner, a PML is a useful method to apply on such equations, since it allows us to study the spatiotemporal behaviour without unwanted boundary interference.

More importantly, a fully functioning PML routine for a model equation would require less computational power and therefore produce solutions faster compared to standard numerical routines for a regular model equation. In general PDEs are computationally intensive, but model equations like the

SHE and the GLE are additionally time consuming since the spatial extent of pattern forming systems must be significantly larger than the length scale of the pattern characteristics. In other words, the computational grid must very large when we want to solve model equations numerically, which imply time consuming algorithms. However, if we are able to implement a PML into the solution routine, the spatial domain only has to be reasonably larger than the pattern characteristics, since the solutions are zeroed out at the PML. Hence, a model equation with a fully functioning PML are to produce the same spatio-temporal characteristics as the regular equation, but the PML solutions are faster to compute.

1.5.2 Outline

Chapter 2 introduces a numerical method named method of lines, and how to apply a PML on a variant of the Schrodinger equation. It also covers how to numerically approximate differential operators with and without a PML, and how to include boundary conditions into the numerical scheme.

Chapter 3 discuss a particular model equation, how to transform it into a model equation with a PML, how to implement the PML scheme for the modele equation. Numerical solutions are also presented.

Chapter 4 serves as an analysis of the results obtained in chapter 3.

Chapter 5 summarizes the relevant findings from chapter 4 and discuss future work.

2

Methods and concepts

To get a feel for the different methods, concepts and techniques we are to apply in our investigation of pattern forming equations, we need a toolbox with certain mathematical and computational tools. These routines are not straightforward to acquire or implement, so as a start, we concentrate on some simpler equations and a few numerical methods to develop some useful machinery.

2.1 A Schrödinger equation

We introduce the one dimensional reduced Schrödinger equation (rSE)

$$\begin{aligned} \phi_t &= i\phi_{xx} \\ \phi(x,t) &= 0 \qquad \text{when } x \to \infty \\ \phi(x,0) &= f(x) \end{aligned} \tag{2.1}$$

defined on the whole line with an initial condition $f(x)$ and zero boundary conditions, where $\phi = \phi(x,t)$. In this section we are to solve the rSE by testing two methods against each other: the numeric MOL versus an implemented analytical Fourier solution.

2.1.1 A Fourier method

We express a solution $\phi(x,t)$ of the rSE in terms of the Fourier transform

$$\widehat{\phi}(k,t) = \frac{1}{\sqrt{2\pi}} \int_{\mathbb{R}} \mathrm{d}x \; \phi(x,t) e^{-ikx} \;, \tag{2.2}$$

$$\phi(x,t) = \frac{1}{\sqrt{2\pi}} \int_{\mathbb{R}} \mathrm{d}k \; \widehat{\phi}(k,t) e^{ikx} \;, \tag{2.3}$$

where $\widehat{\phi}(k,t)$ denotes the inverse transform of $\phi(x,t)$. If we assume the relation

$$\widehat{\phi}(k,t) = \widehat{\phi}_0(k) e^{-i\omega t} \;, \tag{2.4}$$

and insert (2.3) into the rSE, the relation $\omega = k^2$ between the frequencies in the spatial and temporial domain falls out. This ensures a well defined analytical solution for $\phi(x,t)$ on the form

$$\phi(x,t) = \frac{1}{\sqrt{2\pi}} \int_{\mathbb{R}} \mathrm{d}k \; \widehat{\phi}_0(k) e^{-ik^2 t} e^{ikx} \,, \tag{2.5}$$

with a given initial condition $\widehat{\phi}_0(x)$ in the frequency domain. With the Gaussian initial frequency

$$\widehat{\phi}_0(k) = e^{-\frac{(k-k_0)^2}{\sigma}} \;, \tag{2.6}$$

where k_0 denotes a shift from the origin, and σ denotes the width of the bell shape, the spatial initial condition reads

$$f(x) = \frac{1}{\sqrt{2\pi}} \int_{\mathbb{R}} \mathrm{d}k \; e^{-\frac{(k-k_0)^2}{\sigma}} \; e^{ikx} \tag{2.7a}$$

$$= \frac{\sqrt{\sigma}}{\sqrt{2}} \, e^{\left(ik_0 x - \frac{\sigma x^2}{4}\right)} \;. \tag{2.7b}$$

2.1.2 Method of lines

The concept of method of lines (MOL) is way of solving PDEs in which all except one dimension, primarily time, is discretized. A MOL routine transforms a PDE into a large, coupled system of ordinary differential equations, which we are to solve with a standard, general-purpose ordinary differential equation (ODE) solver.

Figure 2.1[7] illustrates how the MOL discretizes space and converts the PDE of some scalar function $u(x,t)$

$$u_t = \mathcal{L}u \ , \tag{2.8}$$

with the corresponding differential operator $\mathcal{L}$, into the ODE system (2.9).

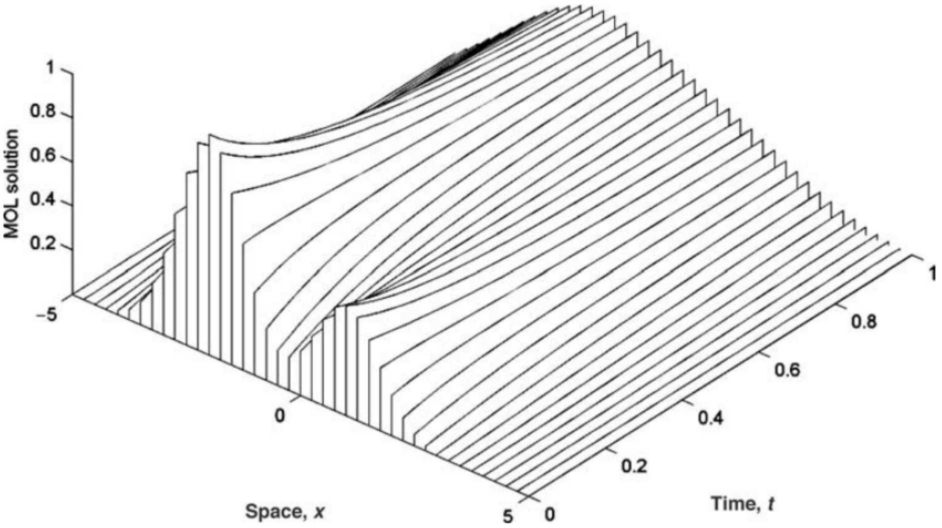

Figure 2.1: An illustration of the method of lines

$$\boldsymbol{u}' = L\boldsymbol{u} \tag{2.9}$$

$\boldsymbol{u}$ in (2.9) denotes the discretized spatial part of $u(x,t)$ by the vector

$$\boldsymbol{u} = \begin{bmatrix} u(x_0,t) & u(x_1,t) & \cdots & u(x_{m-1},t) & u(x_m,t) \end{bmatrix}^T \ , \tag{2.10}$$

defined on the spatial grid $x = [x_0, x_1, \cdots, x_{m-1}, x_m]$. The matrix L is a numerical approximation of $\mathcal{L}$ and constitutes the main problem of the MOL: establish the operator approximation.

If we implement the MOL routine in a object oriented programming language, the code will in general take the form as illustrated in listing 2.1, and at a timestep t_k equation (2.9) reads

$$u_i' = \sum_j L_{ij} u_j \tag{2.11}$$

where $j \in [0, m]$, and u_i denotes the vector $\boldsymbol{u}$ for $i \in [0, m]$.

Listing 2.1: Pseudo code of the MOL

```
def RHS(time, u)
        return dotproduct(D, u)

solution = odesolver(RHS, u_initial)

for timesteps in some_timegrid
        Do solution
```

For a time grid $t = \left[t_0, t_1, \cdots, t_p\right]$, the output of the MOL solution takes the form

$$u(x, t) = \left[u(x, t_0), \quad u(x, t_1), \quad \cdots, \quad u(x, t_p)\right] \ , \tag{2.12}$$

where each element in (2.12) corresponds to the solution over the discrete spatial domain at a certain time step.

The MOL for the rSE

To establish a differential operator for the rSE (2.1) we discretize the spatial grid by

$$\Delta x = \frac{x_{high} - x_{low}}{m} \,, \tag{2.13a}$$

$$x_j = x_{low} + j\Delta x \,, \qquad j \in [0, m] \,, \tag{2.13b}$$

where x_{low} and x_{high} denotes the endpoints of the grid, and $m + 1$ are the number of gridpoints. $\phi_j = \phi(x_j, t)$ describes the function value $\phi(x, t)$ at a gridpoint x_j for all timesteps t_k, as illustrated in figure 2.1. The second order spatial derivative at a gridpoint j is given by the formula

$$[\phi_{xx}]_j \approx \frac{1}{[\Delta x]^2}(\phi_{j-1} - 2\phi_j + \phi_{j+1}) \,, \tag{2.14}$$

where (2.14) is known as the CDM of second order accuracy [6].

Since ϕ_{j-1} and ϕ_{j+1} in (2.14) don't exist at the first and last gridpoints x_0 and x_m respectively, the CDM does not represent ϕ_{xx} with the same accuracy everywhere. To ensure the same precision we apply the second order forward difference method (FDM), and backward difference method (BDM) [2] at the endpoints x_0 and x_m with the standard rules

$$[\phi_{xx}]_{j=0} \approx \frac{1}{[\Delta x]^2}(2\phi_0 - 5\phi_1 + 4\phi_2 - \phi_3) \tag{2.15a}$$

$$[\phi_{xx}]_{j=m} \approx \frac{1}{[\Delta x]^2}(-\phi_{m-3} + 4\phi_{m-2} - 5\phi_{m-1} + 2\phi_m) \,. \tag{2.15b}$$

With the stated difference rules, the rSE turns into the ODE system

$$\frac{d}{dt}\begin{bmatrix} \phi(x_0,t) \\ \phi(x_1,t) \\ \\ \vdots \\ \vdots \\ \\ \phi(x_m,t) \end{bmatrix} = \frac{i}{[\Delta x]^2}\begin{bmatrix} 2 & -5 & 4 & -1 & 0 & \cdots & 0 \\ 1 & -2 & 1 & 0 & 0 & \cdots & 0 \\ 0 & 1 & -2 & 1 & \ddots & & \\ & \ddots & \ddots & \ddots & \ddots & \ddots & \\ & & \ddots & 1 & -2 & 1 & 0 \\ 0 & \cdots & 0 & 0 & 1 & -2 & 1 \\ 0 & \cdots & 0 & -1 & 4 & -5 & 2 \end{bmatrix}\begin{bmatrix} \phi(x_0,t) \\ \phi(x_1,t) \\ \\ \vdots \\ \vdots \\ \\ \phi(x_m,t) \end{bmatrix} \,, \tag{2.16}$$

which in a more compact form reads

$$\boldsymbol{\phi\prime} = iD_2\boldsymbol{\phi} \ , \tag{2.17}$$

where

$$D_2 = \frac{1}{[\Delta x]^2}\begin{bmatrix} 2 & -5 & 4 & -1 & 0 & \cdots & 0 \\ 1 & -2 & 1 & 0 & 0 & \cdots & 0 \\ 0 & 1 & -2 & 1 & \ddots & & \\ & \ddots & \ddots & \ddots & \ddots & \ddots & \\ & & \ddots & 1 & -2 & 1 & 0 \\ 0 & \cdots & 0 & 0 & 1 & -2 & 1 \\ 0 & \cdots & 0 & -1 & 4 & -5 & 2 \end{bmatrix} . \tag{2.18}$$

represents the second order spatial derivative.

Comparing solutions

Now we are to test these independent methods against each other. The analytical Fourier solution (2.5) can be found from brute force summation over a large spatiotemporal grid, and a built in integration routine for the k dependent integral. Moreover, the MOL solution is given by the matrix D_2, the initial condition (2.7b), and the same time grid applied to the Fourier solution.

For the constants in table 2.1 we get the result depicted in figure 2.2 for the real part of the solutions. As the figures illustrate, the analytical and numerical solution coincides and results in a travelling wave packet for the real part of the solution, witch we would expected since we are solving a Schroödinger equation [3]. Table 2.2 states the computational time for both methods, and it

k_0	k_{low}	k_{high}	x_{min}	x_{max}	Δx	t_{min}	t_{max}	Δt	σ
5	-100	100	-10	20	0.1	0	10	0.1	0.5

Table 2.1: Fourier and Difference comparison constants for the RSE

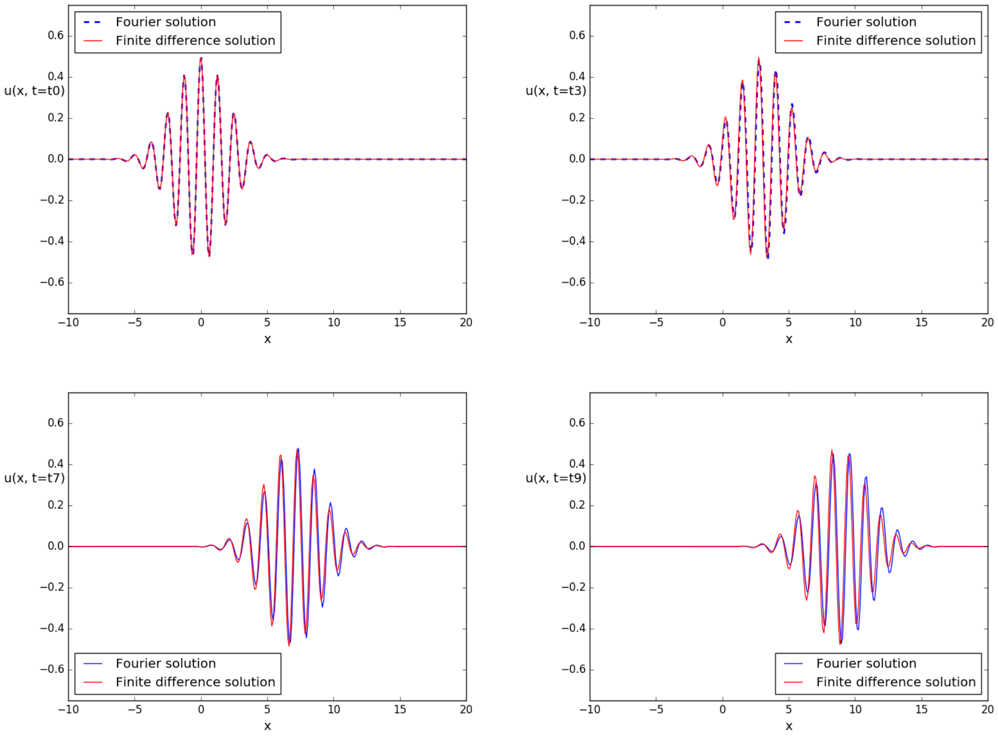

Figure 2.2: Two solutions methods for the RSE plotted against each other for 4 different time steps.

reveals that the MOL is significantly better compared to the time consuming analytic Fourier solution.

Method	**Computing time**
Fourier	621.6 s
Finite difference	2.31 s

Table 2.2: Computing time comparison for the Fourier integral and the MOL

2.2 Discrete approximation of derivatives

2.2.1 A procedure for generating difference rules

Where we in section 2.1.2 applied standard discretization rules for the second order spatial derivative, we now want to develop a somewhat general procedure to generate such difference rules. The following scheme is valid for any $s \geq d$ where:

- d express the order of the derivative we are approximating.
- x_i is the discrete gridpoint we are generating a difference rule around.
- s denotes the number of surrounding gridpoints to x_i, relative to the CDM

In the presented example we estimate the fourth derivative with four and five surrounding gridpoints for the CDM and boundary rules respectively, such that $d = 4$ and $s = 4$.

As a first step in this process we approximate a C^{d+1} function $\phi(x)$ around a point x_i by the series

$$\phi(x) \approx \sum_{l=0}^{s} a_l (x - x_i)^l \ , \tag{2.19}$$

for the CDM, and

$$\phi(x) \approx \sum_{l=0}^{s+1} a_l (x - x_i)^l \ , \tag{2.20}$$

for the boundary rules.

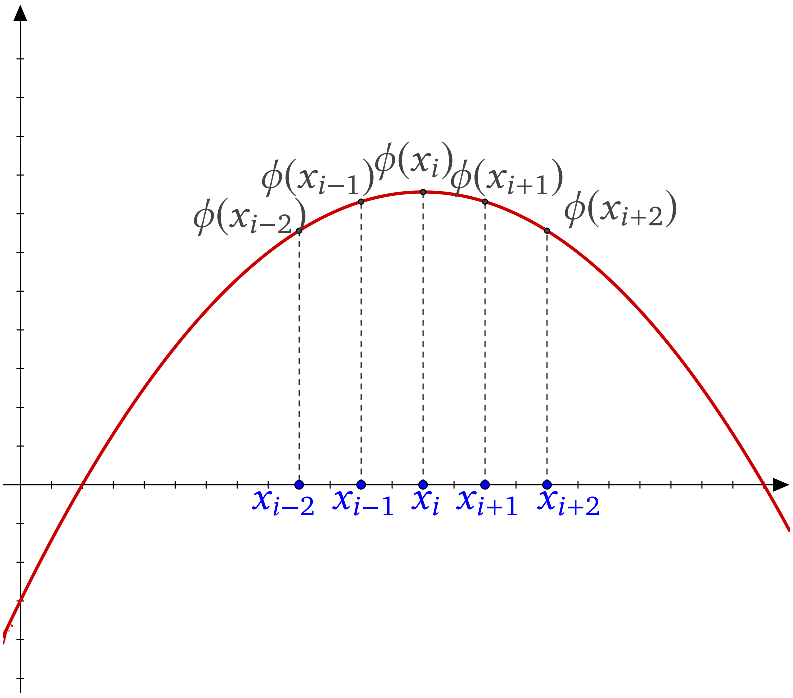

Figure 2.3: A difference routine of order 4

The interior points

Next we express our function and the desired derivative in terms of the approximation (2.19)

$$\phi(x) \approx a_0 + a_1(x - x_i) + a_2(x - x_i)^2 + a_3(x - x_i)^3 + a_4(x - x_i)^4 \ , \qquad (2.21)$$

$$\phi''''(x) \approx 24a_4 \ . \qquad (2.22)$$

These equations illustrate why $s \geq d$ for this procedure to work, since one would end up with 0 for the derivative otherwise. If we discretize the independent variable x by

$$\Delta x = \frac{x_{high} - x_{low}}{m} \ , \qquad (2.23a)$$

$$x_i = x_{low} + i\Delta x \ , \qquad i \in [0, m] \ , \qquad (2.23b)$$

we can center the approximation at any interior gridpoint x_i, as shown figure 2.3. Note that the forthcoming calculations are valid for other discretizations, since the presented procedure is useful as long one are able to keep track of each gridpoint, and have established Δx.

From the s surrounding gridpoints of x_i, the corresponding function values $\phi(x_i)$, and the approximation (2.21), we are able to put up the system of equations (2.24).

$$\begin{aligned}
\phi(x_{i-2}) &= a_0 + a_1(x_{i-2} - x_i) + a_2(x_{i-2} - x_i)^2 \\
&\quad + a_3(x_{i-2} - x_i)^3 + a_4(x_{i-2} - x_i)^4 && \text{(2.24a)} \\
\phi(x_{i-1}) &= a_0 + a_1(x_{i-1} - x_i) + a_2(x_{i-1} - x_i)^2 \\
&\quad + a_3(x_{i-1} - x_i)^3 + a_4(x_{i-1} - x_i)^4 && \text{(2.24b)} \\
\phi(x_i) &= a_0 && \text{(2.24c)} \\
\phi(x_{i+1}) &= a_0 + a_1(x_{i+1} - x_i) + a_2(x_{i+1} - x_i)^2 \\
&\quad + a_3(x_{i+1} - x_i)^3 + a_4(x_{i+1} - x_i)^4 && \text{(2.24d)} \\
\phi(x_{i+2}) &= a_0 + a_1(x_{i+2} - x_i) + a_2(x_{i+2} - x_i)^2 \\
&\quad + a_3(x_{i+2} - x_i)^3 + a_4(x_{i+2} - x_i)^4 && \text{(2.24e)}
\end{aligned}$$

Since the factors

$$(x_{i\pm k} - x_i) = \pm k\Delta x \qquad \text{for } k \in \{0, 1, 2\}\ , \tag{2.25}$$

the equations in (2.24) form a system with $s + 1$ equations and unknowns $\{a_0, \cdots, a_s\}$. The solution of (2.24) reads

$$\begin{aligned}
a_0 &= \phi_i \\
a_1 &= \frac{1}{12\Delta x}(\phi_{i-2} - 8\phi_{i-1} + 8\phi_{i+1} - \phi_{i+2}) \\
a_2 &= -\frac{1}{24\Delta \mathrm{x}^2}(\phi_{i-2} - 16\phi_{i-1} + 30\phi_i - 16\phi_{i+1} + \phi_{i+2}) \\
a_3 &= \frac{1}{12\Delta \mathrm{x}^3}(-\phi_{i-2} + 2\phi_{i-1} - 2\phi_{i+1} + \phi_{i+2}) \\
a_4 &= \frac{1}{24\Delta \mathrm{x}^4}(\phi_{i-2} - 4\phi_{i-1} + 6\phi_i - 4\phi_{i+1} + \phi_{i+2})\ ,
\end{aligned} \tag{2.26}$$

where we according to (2.22) need the a_4 coefficient to establish the desired difference rule for $\phi''''(x)$ as an expression of Δx and $\phi(x_{i\pm k}) = \phi_{i\pm k}$. Our

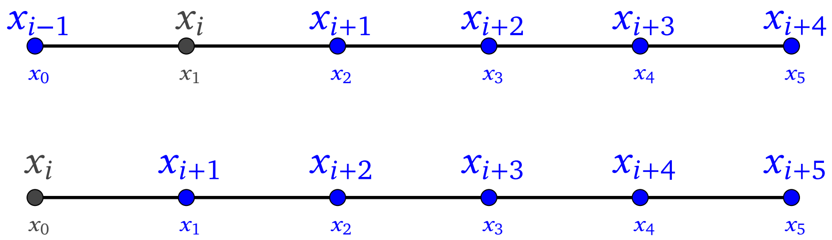

Figure 2.4: Difference rule discretization for the two first gridpoints for $\Phi''''(x)$.

CDM formula then reads

$$\phi''''(x_i) = \frac{1}{\Delta x^4}(\phi_{i-2} - 4\phi_{i-1} + 6\phi_i - 4\phi_{i+1} + \phi_{i+2}) \tag{2.27}$$

in standard form.

Boundary rules

By the same argument as in section 2.1.2, equation (2.27) does not represent $\phi''''(x)$ for the two[1] first and last gridpoints x_0, x_1, x_{m-1}, x_m, and to approximate the derivative at those points, we must modify the CDM setup.

Figure 2.4 highlights the key steps for of the boundary discretization:

- Askew centering for x_i, marked in black.
- The endpoint rules require one more gridpoint relative to the CDM.

Remark that figure only illustrates the leftmost part of the boundary for the FDM discretization, and that the concept apply symmetrically for the BDM at the opposite boundary. The first bullet point concerns the actual gridpoints we need to address difference rules to, while the second - as we will clarify in section 2.2.2 - is necessary to obtain the same order of accuracy for the boundary derivatives. Estimating $\phi(x)$ and $\phi''''(x)$ near the boundary

---

[1] In general there will be s gridpoints that need a modification, with $\frac{s}{2}$ points on each boundary.

gridpoints by (2.20), results in the derivative approximation at the boundary (2.28).

$$\phi''''(x) \approx 24a_4 + a_5 120(x - x_i) \tag{2.28}$$

Since we are skew centring the rules at the boundary gridpoints by $x = x_i$, the second term on the right hand side of (2.28) disappears, and we are again left with (2.22) for the derivative. By the same geometric argument as in figure 2.3 - only with a shifted centre and one more gridpoint - one can put up a $s + 2$ system of equations and unknowns analogous to (2.24), and solve for a_4. As an illustration, we display the system and its corresponding solution coefficient for the case $x_i = x_1$, while the remaining difference rules will be stated.

The equations for the case $x_i = x_1$ is given by

$$\begin{aligned}
\phi_0 &= a_0 + a_1(-\Delta x) + a_2(-\Delta x)^2 + a_3(-\Delta x)^3 + a_4(-\Delta x)^4 \\
\phi_1 &= a_0 \\
\phi_2 &= a_0 + a_1(\Delta x) + a_2(\Delta x)^2 + a_3(\Delta x)^3 + a_4(\Delta x)^4 \\
\phi_3 &= a_0 + a_1(2\Delta x) + a_2(2\Delta x)^2 + a_3(2\Delta x)^3 + a_4(2\Delta x)^4 \\
\phi_4 &= a_0 + a_1(3\Delta x) + a_2(3\Delta x)^2 + a_3(3\Delta x)^3 + a_4(3\Delta x)^4 \\
\phi_5 &= a_0 + a_1(4\Delta x) + a_2(4\Delta x)^2 + a_3(4\Delta x)^3 + a_4(4\Delta x)^4 \ ,
\end{aligned} \tag{2.29}$$

where the solution for a_4 reads

$$a_4 = \frac{1}{24\Delta x^4}(2\phi_0 - 9\phi_1 + 16\phi_2 - 14\phi_3 + 6\phi_4 - \phi_5) \ . \tag{2.30}$$

Assigning the same procedure for the remaining boundary points results in the difference rules

$$\phi''''(x_0) = \frac{1}{\Delta x^4}(3\phi_0 - 14\phi_1 + 26\phi_2 - 24\phi_3 + 11\phi_4 - 2\phi_5) \tag{2.31a}$$

$$\phi''''(x_1) = \frac{1}{\Delta x^4}(2\phi_0 - 9\phi_1 + 16\phi_2 - 14\phi_3 + 6\phi_4 - \phi_5) \tag{2.31b}$$

$$\phi''''(x_{m-1}) = \frac{1}{\Delta x^4}(-\phi_{m-5} + 6\phi_{m-4} - 14\phi_{m-3} + 16\phi_{m-2} - 9\phi_{m-1} + 2\phi_m) \tag{2.31c}$$

$$\phi''''(x_m) = \frac{1}{\Delta x^4}(-2\phi_{m-5} + 11\phi_{m-4} - 24\phi_{m-3} + 26\phi_{m-2} - 14\phi_{m-1} + 3\phi_m)\ . \tag{2.31d}$$

The CDM (2.27) and boundary rules (2.31) comprise the derivative at all spatial gridpoints, and we are to represent $\phi''''(x)$ as

$$\phi''''(x) = \frac{1}{[\Delta x]^4} \begin{bmatrix} 3 & -14 & 26 & -24 & 11 & -2 & 0 & \cdots & 0 \\ 2 & -9 & 16 & -14 & 6 & -1 & 0 & \ddots & 0 \\ 1 & -4 & 6 & -4 & 1 & 0 & & \ddots & \\ 0 & \ddots & \ddots & \ddots & \ddots & \ddots & \ddots & & 0 \\ & \ddots & 1 & -4 & 6 & -4 & 1 & \ddots & \\ 0 & & \ddots & \ddots & \ddots & \ddots & \ddots & \ddots & 0 \\ & & & 0 & 1 & -4 & 6 & -4 & 1 \\ 0 & \ddots & 0 & -1 & 6 & -14 & 16 & -9 & 2 \\ 0 & \cdots & 0 & -2 & 11 & -24 & 26 & -14 & 3 \end{bmatrix} \begin{bmatrix} \phi(x_0) \\ \phi(x_1) \\ \vdots \\ \vdots \\ \\ \vdots \\ \vdots \\ \phi(x_{m-1}) \\ \phi(x_m) \end{bmatrix} , \tag{2.32}$$

which in a more compact form reads

$$\boldsymbol{\phi}'''' = D_4 \boldsymbol{\phi}\ , \tag{2.33}$$

where D_4 defines the operator matrix of $\frac{d^4}{dx^4}$.

2.2.2 Order of accuracy

To determine the order of accuracy for the presented differential approximations, we Taylor expand the terms $\phi(x_{i\pm k})$ for required k around x_i with

$s + 2$ terms, and insert the expansions into the difference rules (2.27) and (2.31).

As the boundary rules states, we need the expansions

$$\begin{aligned}\phi(x_{i\pm1}) &= \phi(x_i) \pm \Delta x\phi'(x_i) + \frac{(\Delta x)^2}{2}\phi''(x_i) \pm \frac{(\Delta x)^3}{6}\phi'''(x_i)\\ &\quad + \frac{(\Delta x)^4}{24}\phi^{(4)}(x_i) \pm \frac{(\Delta x)^5}{120}\phi^{(5)}(x_i) + \frac{(\Delta x)^6}{720}\phi^{(6)}(x_i) \end{aligned} \tag{2.34a}$$

$$\begin{aligned}\phi(x_{i\pm2}) &= \phi(x_i) \pm 2\Delta x\phi'(x_i) + 2(\Delta x)^2\phi''(x_i) \pm \frac{4}{3}(\Delta x)^3\phi'''(x_i)\\ &\quad + \frac{2}{3}(\Delta x)^4\phi^{(4)}(x_i) \pm \frac{4}{15}(\Delta x)^5\phi^{(5)}(x_i) + \frac{4}{45}(\Delta x)^6\phi^{(6)}(x_i) \end{aligned} \tag{2.34b}$$

$$\begin{aligned}\phi(x_{i\pm3}) &= \phi(x_i) \pm 3\Delta x\phi'(x_i) + \frac{9}{2}(\Delta x)^2\phi''(x_i) \pm \frac{9}{2}(\Delta x)^3\phi'''(x_i)\\ &\quad + \frac{27}{8}(\Delta x)^4\phi^{(4)}(x_i) \pm \frac{81}{40}(\Delta x)^5\phi^{(5)}(x_i) + \frac{81}{80}(\Delta x)^6\phi^{(6)}(x_i) \end{aligned} \tag{2.34c}$$

$$\begin{aligned}\phi(x_{i\pm4}) &= \phi(x_i) \pm 4\Delta x\phi'(x_i) + 8(\Delta x)^2\phi''(x_i) \pm \frac{32}{3}(\Delta x)^3\phi'''(x_i)\\ &\quad + \frac{32}{3}(\Delta x)^4\phi^{(4)}(x_i) \pm \frac{128}{15}(\Delta x)^5\phi^{(5)}(x_i) + \frac{256}{45}(\Delta x)^6\phi^{(6)}(x_i)\,, \end{aligned} \tag{2.34d}$$

which inserted into (2.27) and (2.31) leads to the relations (2.35)

$$\phi''''(x_i) = \phi''''(x_i) + \frac{(\Delta x)^2}{6}\phi^{(6)}(x_i) \tag{2.35a}$$

$$\phi''''(x_i) = \phi''''(x_i) - \gamma\frac{(\Delta x)^2}{6}\phi^{(6)}(x_i) \tag{2.35b}$$

for the CDM and bondary rules respectively. We remark that $\gamma = 17$ for outmost gridpoints, while $\gamma = 5$ for the ones within.

According to [6], the second term on the right hand side in (2.35) defines the approximation error, and the corresponding exponent of Δx in the error term determines the order of approximation accuracy. Hence, D_4 represents a second order approximation of the operator $\frac{d^4}{dx^4}$.

The difference rules contained in D_4 are well known and presented in textbooks and articles on the topic[2], but the overall procedure is what we want to bring along within the landscape of pattern forming equations.

2.3 Properties of a discrete differential operator

Where we in section 2.1.2 did not reveal how to implement the boundary conditions of the RSE into the differential operator D_2, we will now discuss how to include such properties into a discrete approximation of a differential operator.

For simplicity we will work with the second order accuracy approximation of ∂_{xx} (2.18), which in a rewritten form reads

$$D_2 = \begin{bmatrix} \alpha_1 & \alpha_2 & \alpha_3 & \alpha_4 & 0 & \cdots & 0 \\ c_1 & c_2 & c_3 & 0 & \cdots & & 0 \\ 0 & c_1 & c_2 & c_3 & & & \vdots \\ \vdots & & \ddots & \ddots & \ddots & & \vdots \\ \vdots & & & c_1 & c_2 & c_3 & 0 \\ 0 & & \cdots & 0 & c_1 & c_2 & c_3 \\ 0 & \cdots & 0 & \alpha_4 & \alpha_3 & \alpha_2 & \alpha_1 \end{bmatrix} . \tag{2.36}$$

The factor $1/(\Delta x)^2$ in (2.18) is embedded into the matrix operator (2.36), and the dimension of D_2 is $(m+1)^2$.

We remark that the procedure presented in the upcoming paragraphs is similar for other orders of derivatives and accuracy, but involves more of the same ideas, and thereby more calculations.

2.3.1 Boundary conditions

Before we reveal how to include boundary conditions into a operator matrix, we must discuss how the MOL algorithm calculates its results. Rewriting (2.9) with the matrix operator (2.36) leads to the relation

$$\frac{d}{dt}\begin{bmatrix} u(x_1,t) \\ u(x_2,t) \\ u(x_3,t) \\ \vdots \\ \vdots \\ u(x_{m-1},t) \end{bmatrix} = \begin{bmatrix} u_0\alpha_1 + u_1\alpha_2 + u_2\alpha_3 + u_3\alpha_4 \\ u_0c_1 + u_1c_2 + u_2c_3 \\ u_1c_1 + u_2c_2 + u_3c_3 \\ u_2c_1 + u_3c_2 + u_4c_3 \\ \vdots \\ \vdots \\ u_{m-2}c_1 + u_{m-1}c_2 + u_mc_3 \\ u_{m-3}\alpha_4 + u_{m-2}\alpha_3 + u_{m-1}\alpha_2 + u_m\alpha_1 \end{bmatrix}, \tag{2.37}$$

where $\{u_0, \cdots, u_m\}$ denotes the values $\{u(x_0,t), \cdots, u(x_m,t)\}$.

Zero boundary conditions

To maintain zero boundary conditions for the system (2.9), we require that the relations

$$u(x_0,t) = 0 \quad \text{and} \quad u(x_m,t) = 0 \tag{2.38}$$

holds for all t in (2.37). One possibility to ensure so is to set the α-constants in (2.36) to zero, and implement $u(x_0,t) = u(x_m,t) = 0$ in the RHS illustrated in listing 2.1 to provide that the u_0 and u_m terms in (2.37) are zero for all t. An equivalent alternative, and the one we choose to apply, is to remove the first and last rows and columns of the operator matrix, while removing the points u_0 and u_m from our computational grid. In that manner, the modified matrix operator and the acting gridpoints produces a solution as if the boundary values were zero. This procedure results in the matrix illustrated in figure 2.5, and the MOL equation (2.39).

$$\frac{d}{dt}\begin{bmatrix} u(x_1,t) \\ u(x_2,t) \\ u(x_3,t) \\ \vdots \\ \vdots \\ u(x_{m-1},t) \end{bmatrix} = \begin{bmatrix} u_1c_2 + u_2c_3 \\ u_1c_1 + u_2c_2 + u_3c_3 \\ u_2c_1 + u_3c_2 + u_4c_3 \\ \vdots \\ \vdots \\ u_{m-2}c_1 + u_{m-1}c_2 \end{bmatrix}. \tag{2.39}$$

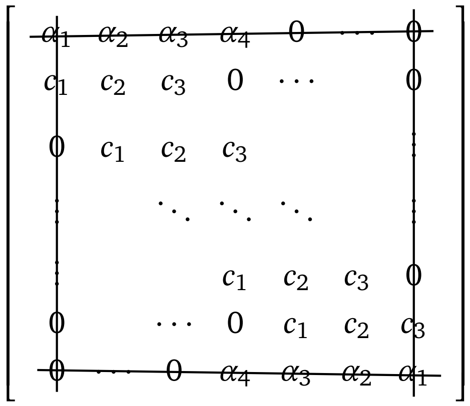

Figure 2.5: Modified operator matrix to sustain zero boundary conditions

$u(x,t) = 0$ and $u_x(x,t) = 0$ at the boundary

In order to sustain both $u_x(x,t) = 0$ and $u(x,t) = 0$ at the boundary, the reasoning and the manipulations from the previous subsection apply to the condition $u(x,t) = 0$. If $u_x(x,t) = 0$ are to be satisfied , some elements of the operator matrix need to be adjusted. To see why, we investigate the rules that describes the first order spatial derivative of second order accuracy at the endpoints[2] of the grid:

$$u'(x_0) = \frac{1}{2\Delta x}\left[-3u(x_0) + 4u(x_1) - u(x_2)\right] \tag{2.40a}$$

$$u'(x_m) = \frac{1}{2\Delta x}\left[u(x_{m-2}) - 4u(x_{m-1}) + 3u(x_m)\right] \ . \tag{2.40b}$$

For simplicity we have not included the time variable in the equations and imminent calculations, since the spatial calculations are the same for all t, relative to the MOL.

Since $u(x) = 0$ at the boundaries, the terms containing $u(x_0)$ or $u(x_m)$ in (2.40) disappears from the equations. To ensure a zero derivative on the boundaries we let $u'(x_0) = u'(x_m) = 0$ in (2.40) to obtain the relations

$$u(x_1) = \frac{u(x_2)}{4} \tag{2.41a}$$

$$u(x_{m-1}) = \frac{u(x_{m-2})}{4} \ . \tag{2.41b}$$

These equations are now the criteria we must implement into our operator matrix. To manage this, we put up the difference rules containing the left hand side terms of (2.41):

$$u'(x_1) = c_1 u(x_0) + c_2 u(x_1) + c_3 u(x_2) \tag{2.42a}$$
$$u'(x_2) = c_1 u(x_1) + c_2 u(x_2) + c_3 u(x_3) \tag{2.42b}$$
$$u'(x_{m-2}) = c_1 u_{m-3} + c_2 u_{m-2} + c_3 u(x_{m-1}) \tag{2.42c}$$
$$u'(x_{m-1}) = c_1 u_{m-2} + c_2 u_{m-1} + c_3 u(x_m) \ . \tag{2.42d}$$

Inserting (2.41) and (2.38) into the difference rules (2.42), they turn out as

$$u'(x_1) = u(x_2)\left(\frac{c_2}{4} + c_3\right) \tag{2.43a}$$
$$u'(x_2) = u(x_2)\left(\frac{c_1}{4} + c_2\right) + c_3 u(x_3) \tag{2.43b}$$
$$u'(x_{m-2}) = c_1 u(x_{m-3}) + u(x_{m-2})\left(c_2 + \frac{c_3}{4}\right) \tag{2.43c}$$
$$u'(x_{m-1}) = u(x_{m-2})\left(c_1 + \frac{c_2}{4}\right) \ . \tag{2.43d}$$

To incorporate this into the operator matrix we exclude two more rows and columns, while we build in the relations (2.43), as demonstrated in figure 2.6. This might seem as trickery since we are removing two more gridpoints from our computational grid, which could affect our solution. What saves the day, is that the equations (2.41) and (2.43) incorporates those gridpoints into the operator matrix, together with the boundary derivatives.

$u(x,t) = 0$ **and** $\mathrm{u_{xx}(x,t)} = 0$ **at the boundary**

Redoing the routine described in the previous section with the second derivative of second order accuracy[2], which is given by the equations

$$u''(x_0) = \frac{1}{\Delta x^2}[2u(x_0) - 5u(x_1) + 4u(x_2) - u(x_3)] \tag{2.44a}$$
$$u''(x_m) = \frac{1}{\Delta x^2}[-u(x_{m-3}) + 4u(x_{m-2}) - 5u(x_{m-1}) + 2u(x_m)] \ , \tag{2.44b}$$

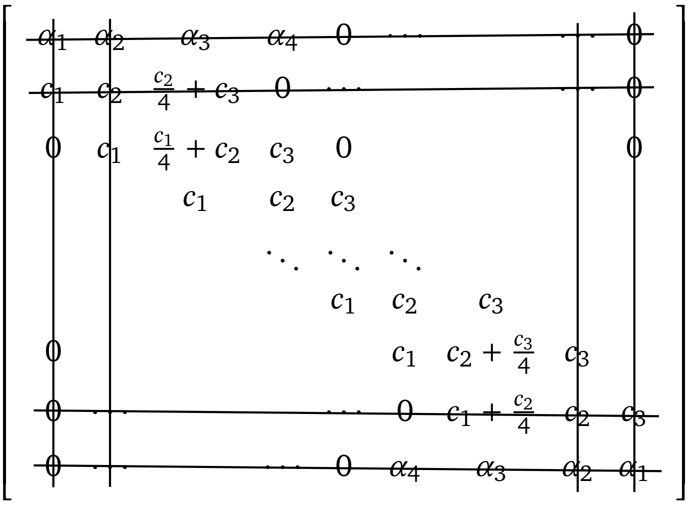

Figure 2.6: Modified operator matrix for $u(x,t) = 0$ and $u_x(x,t) = 0$ at the boundaries.

results in equations

$$u(x_1) = \frac{4}{5}u(x_2) - \frac{1}{5}u(x_3) \tag{2.45a}$$

$$u(x_{m-1}) = -\frac{1}{5}u(x_{m-3}) + \frac{4}{5}u(x_{m-2})\ . \tag{2.45b}$$

(2.45) constitutes the boundary criteria, and inserting those into the difference rules (2.42) leads to the relations

$$u'(x_1) = u(x_2)\left(\frac{4c_2}{5} + c_3\right) - \frac{c_2}{5}u(x_3) \tag{2.46a}$$

$$u'(x_2) = u(x_2)\left(\frac{4c_1}{5} + c_2\right) + u(x_3)\left(c_3 - \frac{c_1}{5}\right) \tag{2.46b}$$

$$u'(x_{m-2}) = u(x_{m-3})\left(c_1 - \frac{c_3}{5}\right) + u(x_{m-2})\left(c_2 + \frac{4c_3}{5}\right) \tag{2.46c}$$

$$u'(x_{m-1}) = -\frac{c_3}{5}u(x_{m-3}) + u(x_{m-2})\left(c_1 + \frac{4c_2}{5}\right)\ , \tag{2.46d}$$

which modifies the operator matrix into the matrix depicted in figure 2.7.

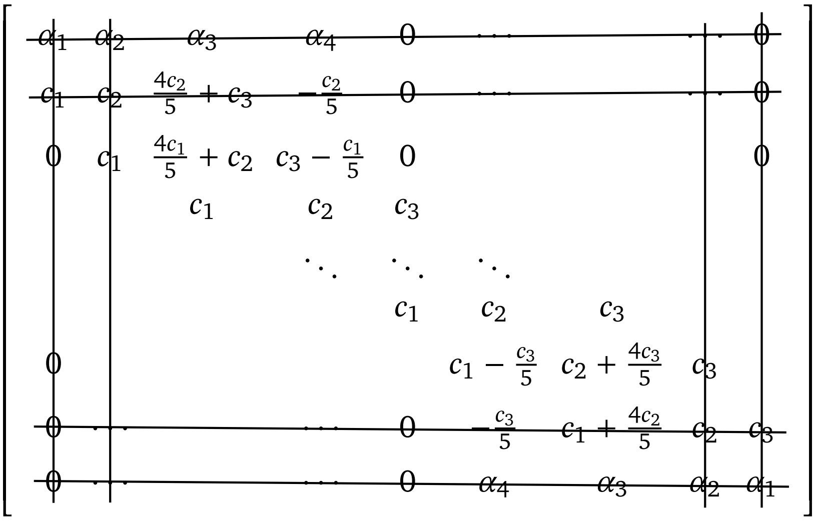

$$\begin{bmatrix}
\alpha_1 & \alpha_2 & \alpha_3 & \alpha_4 & 0 & \cdots & & \cdots & 0 \\
c_1 & c_2 & \frac{4c_2}{5}+c_3 & -\frac{c_2}{5} & 0 & \cdots & & \cdots & 0 \\
0 & c_1 & \frac{4c_1}{5}+c_2 & c_3-\frac{c_1}{5} & 0 & & & & 0 \\
 & & c_1 & c_2 & c_3 & & & & \\
 & & & \ddots & \ddots & \ddots & & & \\
 & & & & c_1 & c_2 & c_3 & & \\
0 & & & & & c_1-\frac{c_3}{5} & c_2+\frac{4c_3}{5} & c_3 & \\
0 & \cdots & & \cdots & 0 & -\frac{c_3}{5} & c_1+\frac{4c_2}{5} & c_2 & c_3 \\
0 & \cdots & & \cdots & 0 & \alpha_4 & \alpha_3 & \alpha_2 & \alpha_1
\end{bmatrix}$$

Figure 2.7: Modified operator matrix for $u(x,t) = 0$ and $u_{xx}(x,t) = 0$ at the boundaries.

2.3.2 Combining operators

For the differential operators

$$L_2 = \frac{d^2}{dx^2} \tag{2.47a}$$

$$L_4 = \frac{d^4}{dx^4}\ , \tag{2.47b}$$

it is from elementary operator algebra known that

$$L_2[L_2 f(x)] = [L_2 L_2] f(x) \tag{2.48a}$$

$$= L_4 f(x) \tag{2.48b}$$

for some C^4 function $f(x)$.

Since we have established numerical approximations for the operators (2.47) with the matrices D_2 (2.18) and D_4 (2.32), we can test if (2.48) holds for the discrete case. The discrete equivalent of $[L_2 L_2]$ is given by

$$[D_2]^2 = \begin{bmatrix} -1. & 4. & -6. & 4. & -1. & 0. & \cdots & & 0. \\ 0. & 0. & 0. & 0. & 0. & 0. & 0. & 0. & 0. \\ 1. & -4. & 6. & -4. & 1. & 0. & 0. & 0. & 0. \\ \vdots & \ddots & \ddots & \ddots & \ddots & \ddots & \ddots & & \vdots \\ 0. & 0. & 1. & -4. & 6. & -4. & 1. & 0. & 0. \\ \vdots & & \ddots & \ddots & \ddots & \ddots & \ddots & \ddots & 0. \\ 0. & 0. & 0. & 0. & 1. & -4. & 6. & -4. & 1. \\ 0. & 0. & 0. & 0. & 0. & 0. & 0. & 0. & 0. \\ 0. & & \cdots & 0. & -1. & 4. & -6. & 4. & -1. \end{bmatrix}, \tag{2.49}$$

which imply the relation

$$(D_2)^2 \neq D_4 \tag{2.50}$$

by comparing (2.49) with D_4 in (2.32). In (2.49) we note that the identity (2.48) holds for the interior points, but breaks down at boundary. Since the MOL converts a PDE into a system of coupled ODEs, the boundary rules are important, as we discussed in the previous subsections regarding the boundary conditions, and we are to be aware of the result (2.50).

2.4 Perfectly Matched Layer for the reduced Schrödinger equation

As an introductory example, we will demonstrate and make use of the PML on the rSE with a contour based PML.

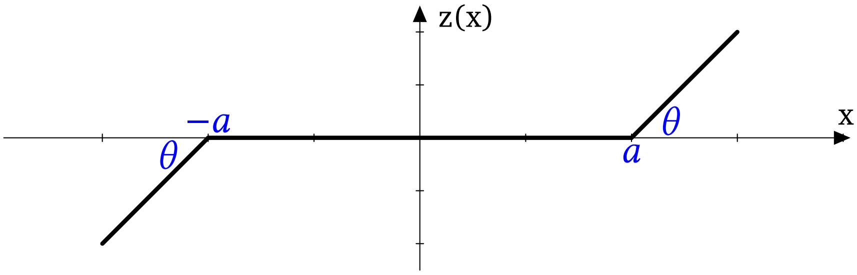

Figure 2.8: The complex contour $z(x)$ in (2.51)

2.4.1 The overall idea of a contour based PML

For a solution $\phi(x,t)$ of the rSE we introduce its analytic continuation $\Phi(z,t)$ where $\Phi|_{\mathbb{R}} = \phi$, and the complex contour

$$z(x) = \begin{cases} -a + e^{i\theta}(x+a) & \text{for } x \leq -a \\ x & \text{for } x \in (-a,a) \\ a + e^{i\theta}(x-a) & \text{for } x \geq a\,. \end{cases} \tag{2.51}$$

The angle θ is defined as in figure 2.8, and we say that the PML starts at the points $\{z(x) = \pm a\}$. To uphold a precise language we will from now on, and throughout the thesis, refer to the points $\{z(x) = \pm a\}$ as the PML points, the set $\{z(x) \in (-a,a)\}$ as outside the PML region, and the two remaining sets as inside the PML region[2]. The contour branches $z(x)^-$ and $z(x)^+$ are referred to as the negative and positive PML regions respectively.

We define

$$\Psi(x,t) = \Phi(z,t)\big|_{z=z(x)} \tag{2.52}$$

as the analytical continuation of $\phi(x,t)$ along the contour $z(x)$. Hence, $\Psi(x,t)$ takes the same values as $\phi(x,t)$ outside the PML region, but is modified on the inside. Our claim is that the input domain modification $x \to z(x)$ impose a PML for the rSE, and to show why, we study a single solution mode of the rSE

$$\phi_0(x,t) = Ae^{-i\omega t}e^{ikx} \tag{2.53}$$

---

[2] It is possible to argue about the semantics in this choice of inside and outside for the PML region, but for simplicity we have let "the inside" be where the PML applies.

where $\omega = k^2$, as in section 2.1.1. If we assume that the mode initiates at the origin and ensure $k > 0$, the wave propagates towards the positive PML region. Denoting $e^{i\theta} = \tilde{c} = \alpha + i\beta$ where $\{\alpha, \beta\} \in \mathbb{R}^+$ for consistency with figure 2.8, $z(x)^+$ could be rewritten as

$$\begin{aligned} z(x)^+ &= a + e^{i\theta}(x - a) && (2.54a) \\ &= a(1 - \tilde{c}) + (\alpha + i\beta)x \,. && (2.54b) \end{aligned}$$

Incorporating this form of $z(x)^+$ into (2.53), a wave packet moving from the origin into the positive PML region turn out as

$$\begin{aligned} \phi_0(z(x)^+, t) &= Ae^{-ik^2t}e^{ika(1-\tilde{c})}e^{ikx(\alpha+i\beta)} && (2.55a) \\ &= \tilde{A}e^{-ik^2t}e^{ikx\alpha}e^{-kx\beta} && (2.55b) \\ &= \tilde{A}e^{-i(k^2t-kx\alpha)}e^{-kx\beta} && (2.55c) \\ &= \tilde{A}e^{-iG(x,t)}e^{-kx\beta} \,, && (2.55d) \end{aligned}$$

where $\tilde{A} = Ae^{ika(1-\tilde{c})}$ and $G(x, t) = (k^2t - kx\alpha)$. The first two factors in (2.55d) describes the mode amplitude and oscillatory behaviour, while the last factor ensures exponential decay since $\beta, k, x > 0$. For a wave mode travelling in the other direction $z(x)^-$, we may redo the calculations with $\{k, \alpha, \beta\} < 0$ for consistency with direction and figure 2.8. This results in a solution

$$\phi_0(z(x)^-, t) = \tilde{A}e^{-iH(x,t)}e^{kx\beta} \qquad (2.56)$$

where $\tilde{A} = Ae^{ika(\tilde{c}-1)}$ and $H(x, t) = (k^2t + kx\alpha)$. The outcome of this scenario is the same as for the positive PML region, since the numbers $\beta, k, x < 0$. If we impose the Fourier mode solution

$$\phi(x, t) = \sum_k Ae^{-ik^2t}e^{ikx} \qquad (2.57)$$

to the rSE, the presented arguments ensures exponential decay inside the PML region for all k.

Now we are to transform the rSE into a problem containing the PML imposed solution $\Psi(x, t)$. In general, the procedure has the following structure: begin with the original problem, put up the analogous equation for the general analytical continuation $\Phi(z,t)$, and evaluate it along the contour $z = z(x)$. This idea is illustrated schematically in (2.58c).

$$\phi(x,t)_t = i\phi(x,t)_{xx} \tag{2.58a}$$

$$\downarrow \text{ analytic continuation}$$

$$\Phi(z,t)_t = i\Phi(z,t)_{zz} \tag{2.58b}$$

$$\downarrow \text{ along } z(x)$$

$$\Phi(z,t)_t \Big|_{z=z(x)} = i\Phi(z,t)_{zz} \Big|_{z=z(x)} \tag{2.58c}$$

Our task is then to express the spatiotemporal derivatives of (2.58c) in terms of $\Psi(x,t)$. From the chain rule we obtain the relations

$$\begin{aligned}
\partial_x \Psi(x,t) &= \partial_x \Phi(z(x),t) && (2.59a)\\
&= \frac{\partial \Phi(z(x),t)}{\partial z}\frac{\partial z(x)}{\partial x} && (2.59b)\\
&= z'(x)\ \partial_z \Phi(z(x),t) && (2.59c)\\
&= \Phi_z z' \ , && (2.59d)
\end{aligned}$$

$$\begin{aligned}
\partial_{xx}\Psi(x,t) &= \partial_x[\partial_x \Psi(x,t)] && (2.60a)\\
&= \partial_x\left[z'(x)\ \partial_z \Phi(z(x),t)\right] && (2.60b)\\
&= z''(x)\partial_z\Phi(z(x),t) + z'(x)\partial_x\partial_z\Phi(z(x),t) && (2.60c)
\end{aligned}$$

$$\downarrow \text{ where } \Phi(z(x),t)|_{\mathbb{R}} \in C^2 :\ \ \partial_x\partial_z = \partial_z\partial_x \tag{2.60d}$$

$$\begin{aligned}
&= z''(x)\partial_z\Phi(z(x),t) + z'(x)\partial_z[\partial_x\Phi(z(x),t)] && (2.60e)\\
&= z''(x)\partial_z\Phi(z(x),t) + z'(x)\partial_z[z'(x)\ \partial_z\Phi(z(x),t)] && (2.60f)\\
&= z''(x)\partial_z\Phi(z(x),t) + [z'(x)]^2\partial_{zz}\Phi(z(x),t) && (2.60g)\\
&= z''\Phi_z + [z']^2\Phi_{zz} \ , && (2.60h)
\end{aligned}$$

for the spatial derivatives. Combining the results from (2.59) - (2.60) will after some manipulation result in the relations (2.61) - (2.62), which describes the PML-modified first and second order derivative.

$$\Phi_z = \frac{\Psi_x}{z'} \tag{2.61}$$

$$\Phi_{zz} = \left[\Psi_{xx} - \frac{z''}{z'}\Psi_x\right]\frac{1}{[z']^2} \tag{2.62}$$

Since $\Psi(x,t)$ and $\Phi(z(x),t)$ depends equally on time, the temporal derivative does not change, such that

$$\partial_t \Psi(x,t) = \partial_t \Phi(z(x),t)\,. \tag{2.63}$$

The converted equation (2.58c) with $z(x)$ as stated in (2.51), and the derived relations (2.61) - (2.62) leads to the PML version of the rSE

$$\Psi_t = i\,\mathcal{L}\Psi\,, \tag{2.64}$$

where the operator $\mathcal{L}$ reads

$$\mathcal{L} = \begin{cases} \frac{1}{e^{2i\theta}}\Psi_{xx} & \text{for } x < -a \\ \Phi_{zz}\big|_{z=z(x)} & \text{for } x = -a \\ \Psi_{xx} & \text{for } x \in (-a,a) \\ \Phi_{zz}\big|_{z=z(x)} & \text{for } x = a \\ \frac{1}{e^{2i\theta}}\Psi_{xx} & \text{for } x > a\,. \end{cases} \tag{2.65}$$

Since $z(x)$ not is twice continuous differentiable at the PML points $\{z(x) = \pm a\}$, as we assumed in (2.60d) for the mixed partial derivatives, the operator $\mathcal{L}$ must be defined specifically in terms of $\Phi(z(x),t)$ at those points. To manage this we apply the difference rule procedure discussed in section 2.2.1, where we will express the spatial part of $\Phi(z(x),t)$ with the approximation

$$\Phi(z_j,t)\big|_{z_j=\pm a} \approx \sum_{l=0}^{s} c_i(t)(z_j - z_i)^l \tag{2.66}$$

of some order s to match the desired order of accuracy. In (2.66) z_j denotes $z(x_j)$, while z_i express the points we are assigning difference rules to, where $\Phi(z_j,t)$ corresponds to a function value at the gridpoint z_j.

Given a suitable discretisation, and a correct boundary condition setup, $\mathcal{L}$ is now possible to implement on a computer.

To illustrate the PML setup in terms of relevant domains, we refer to the diagram in figure 2.9.

$$\begin{tikzcd}
\mathbb{R}\times\mathbb{R} \arrow[r, "z(x)"] \arrow[rr, bend left, "\phi(x{,}t)"] \arrow[rr, bend right, "\Psi(x{,}t)"'] & \mathbb{C}\times\mathbb{R} \arrow[r, "\Phi(z(x){,}t)"] & \mathbb{C}\times\mathbb{R}
\end{tikzcd}$$

Figure 2.9: Diagram for the rSE continuation

2.4.2 Discretization of the rSE with the PML

To be able to land a numerical solution routine like the MOL for the reformulated rSE (2.64), there are some key details we must delve into concerning the operator $\mathcal{L}$. As discussed in section 2.2.1, our overall goal is to construct a matrix that represents the discretized operator for the spatial derivatives, but since the difference rules varies between each defined region in (2.65), we must include this feature into the numerical scheme.

For the PML scheme to be at all useful we must ensure that the PML points are on the grid, and the discretization

$$\Delta x = \frac{a}{M} \tag{2.67a}$$

$$L = \Delta x \cdot N \tag{2.67b}$$

$$x_l = l \cdot \Delta x \qquad l \in (-N, N)\,, \tag{2.67c}$$

ensures this detail. In (2.67) M denotes the number of gridpoints from the origin to the PML point a, while N express the number of gridpoints from the

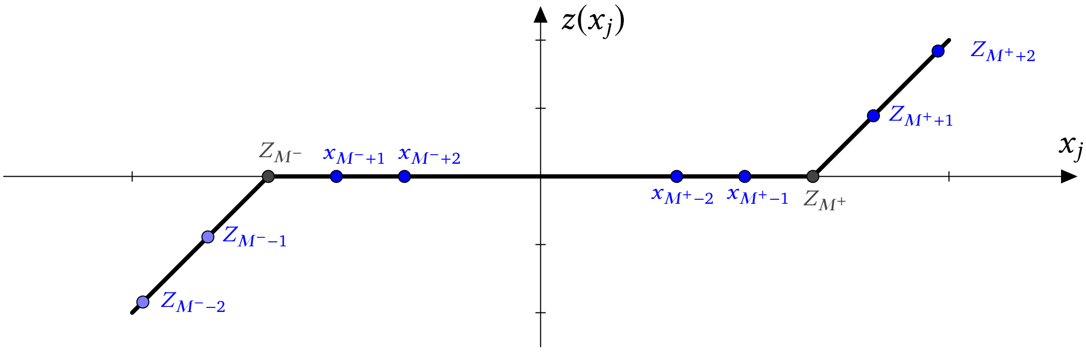

Figure 2.10: Discretization of the complex contour $z(x)$

origin to the endpoint L. Note that the domain length L with this discretization follows as a consequence of N:

$$L = a\,\frac{N}{M}\;. \tag{2.68}$$

The discrete version of $z(x)$ reads

$$z(x_l) = \begin{cases} -x_M + e^{i\theta}(x_l + a) & \text{for } x_l \le -a \\ x_l & \text{for } x_l \in (-a, a) \\ x_M + e^{i\theta}(x_l - a) & \text{for } x_l \ge a\,, \end{cases} \tag{2.69}$$

where $a = x_M$. Figure 2.10 illustrates the outline of this discretization where $z(x_j) = z_j$, and $\{z_{M^-}, z_{M^+}\}$ denotes the PML points such that

$$z_{M^-} = -a \quad \text{and} \quad z_{M^+} = a\;. \tag{2.70}$$

2.4.3 Generating the operator $\mathcal{L}$ for the rSE with PML enforced

With the discretization(2.67), the spatial part of the operator $\mathcal{L}$ in (2.65) takes the form of the following block matrix

$$\mathcal{D}_2(\theta) = \begin{pmatrix} D^{z(x)^-} & & & & \\ & PML^- & & \mathbf{O} & \\ & & D^{\mathbb{R}} & & \\ & \mathbf{O} & & PML^+ & \\ & & & & D^{z(x)^+} \end{pmatrix}. \tag{2.71}$$

The $PML^{\mp}$ blocks in (2.71) corresponds to the PML points at $x = \pm a$ in (2.65), and will be discussed on the next pages. Using a fourth order precision for Ψ_{xx}, the D-blocks in (2.71) turn out as

$$D^{z(x)^-} = \frac{e^{-2i\theta}}{\Delta x^2} \begin{pmatrix} \frac{15}{4} & -\frac{77}{6} & \frac{107}{6} & -13 & \frac{61}{12} & -\frac{5}{6} & \\ \frac{5}{6} & -\frac{5}{4} & -\frac{1}{3} & \frac{7}{6} & -\frac{1}{2} & \frac{1}{12} & \\ -\frac{1}{12} & \frac{4}{3} & -\frac{5}{2} & \frac{4}{3} & -\frac{1}{12} & & \\ & \ddots & \ddots & \ddots & \ddots & \ddots & \\ & & -\frac{1}{12} & \frac{4}{3} & -\frac{5}{2} & \frac{4}{3} & -\frac{1}{12} \end{pmatrix}, \tag{2.72}$$

$$D^{\mathbb{R}} = \frac{1}{\Delta x^2} \begin{pmatrix} -\frac{1}{12} & \frac{4}{3} & -\frac{5}{2} & \frac{4}{3} & -\frac{1}{12} & & \\ & \ddots & \ddots & \ddots & \ddots & \ddots & \\ & & -\frac{1}{12} & \frac{4}{3} & -\frac{5}{2} & \frac{4}{3} & -\frac{1}{12} \end{pmatrix}, \tag{2.73}$$

$$D^{z(x)^+} = \frac{e^{-2i\theta}}{\Delta x^2} \begin{pmatrix} -\frac{1}{12} & \frac{4}{3} & -\frac{5}{2} & \frac{4}{3} & -\frac{1}{12} & & \\ & \ddots & \ddots & \ddots & \ddots & \ddots & \\ & & -\frac{1}{12} & \frac{4}{3} & -\frac{5}{2} & \frac{4}{3} & -\frac{1}{12} \\ & \frac{1}{12} & -\frac{1}{2} & \frac{7}{6} & -\frac{1}{3} & -\frac{5}{4} & \frac{5}{6} \\ & -\frac{5}{6} & \frac{61}{12} & -13 & \frac{107}{6} & -\frac{77}{6} & \frac{15}{4} \end{pmatrix}, \tag{2.74}$$

where the entries of these D-blocks are generated in the same way as in section 2.2.1 for the constants $d = 2$ and $s = 4$.

2.4.4 Generating difference rules around the PML points

As stated in the derivation of the operator $\mathcal{L}$ (2.65), we must build our numerical scheme at the PML points from the analytical continuation $\Phi(z, t)$. In order to understand why, we will explain why we not want to use $\Psi(x, t)$ to do so.

Since $\Psi(x,t) = \Phi(z,t)|_{z=z(x)}$, the following relations apply

- at negative PML point:

$$\Psi_x = -e^{i\theta}\Phi_z|_{z=-a} \ , \tag{2.75}$$

- for $x \in (-a,a)$:

$$\Psi_x = \Phi_z \ , \tag{2.76}$$

- at positive PML point:

$$\Psi_x = e^{i\theta}\Phi_z|_{z=a} \ . \tag{2.77}$$

To keep the number of calculations at a minimum we only derive the forthcoming relation for the positive PML point, while we will state the analogous relation at the negative PML point.

We define the following

$$\Psi_x^+ = \lim_{x\to a^+} \Psi_x \tag{2.78a}$$

$$= e^{i\theta}\Phi_z|_{z=a} \ , \tag{2.78b}$$

$$\Psi_x^- = \lim_{x\to a^-} \Psi_x \tag{2.78c}$$

$$= \Phi_z|_{z=a} \ , \tag{2.78d}$$

which combined leads to the relation

$$\Psi_x^+ = e^{i\theta}\Psi_x^- \tag{2.79}$$

at the positive PML point. Redoing the same calculations would result in the relation

$$-e^{i\theta}\Psi_x^- = \Psi_x^+ \tag{2.80}$$

at the negative PML point.

(2.79) and (2.80) illustrates that the spatial derivative of $\Psi(x,t)$ is discontinuous at the PML points, and the relations are to be coincided as internal boundary conditions for the RSE.

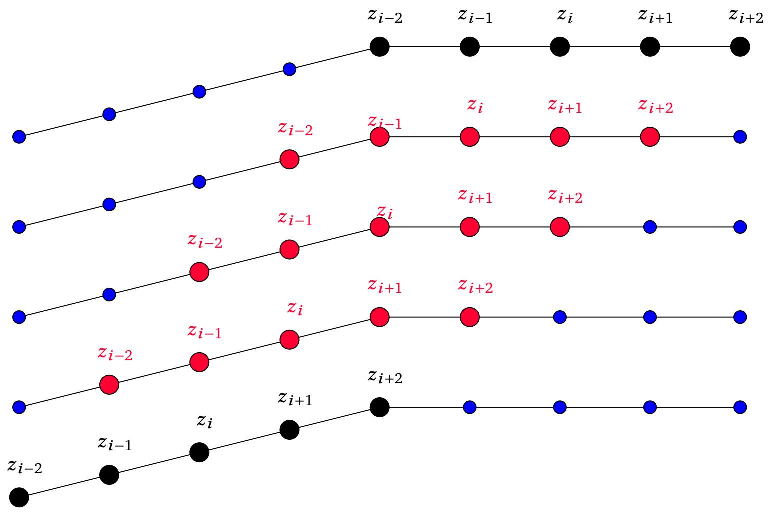

Figure 2.11: The CDM around the negative PML point with a five point approximation.

The relations (2.79) and (2.80) are obviously tedious to handle, so in stead of implementing these unmanageable relations into our numerical scheme, we turn to the analytic continuation. Since $\Phi(z, t)$ is a analytic continuation of $\phi(x, t)$, it is per definition possible to approximate by a power series, which we therefore may use to generate the differential rules from.

To generate difference rules for the two regions where the PML emerges we approximate discrete function value $\Phi(z_j, t)$ around the PML points z_i by

$$\begin{aligned}\Phi(z_j, t) \approx c_0(t) + c_1(t)(z_j - z_i) + c_2(t)(z_j - z_i)^2 \\ + c_3(t)(z_j - z_i)^3 + c_4(t)(z_j - z_i)^4 \,,\end{aligned} \tag{2.81}$$

to uphold the same order of accuracy as the matrices (2.72) - (2.74).

Since the CDM extends over $s + 1$ gridpoints, we must modify $s - 1$ difference rules around each PML point to approximate $\Phi(z_j, t)$ at those points. To understand why, we turn to figure 2.11 for clarification. The figure depicts the CDM with $s = 4$ at the outbreak of the negative PML domain, for the gridpoints $z_i \in \{z_{M^- -2}, z_{M^- +2}\}$. From the figure we observe:

- The factors $(z_j - z_i)$ for the rules marked with black gridpoints are fully contained inside or outside PML domain, and thereby belongs to the D-blocks in (2.71).

- The rules marked with red gridpoints have factors $(z_j - z_i)$ that extend inside and outside of the PML domain, and must be calculated separately.

With the approximation (2.81) we can put up equations analogous to the system (2.24)

$$\begin{aligned}
\Phi(z_{i-2}, t) &= c_0(t) + c_1(t)(z_{i-2} - z_i) + c_2(t)(z_{i-2} - z_i)^2 && (2.82a)\\
&\quad + c_3(t)(z_{i-2} - z_i)^3 + c_4(t)(z_{i-2} - z_i)^4 \\
\Phi(z_{i-1}, t) &= c_0(t) + c_1(t)(z_{i-1} - z_i) + c_2(t)(z_{i-1} - z_i)^2 && (2.82b)\\
&\quad + c_3(t)(z_{i-1} - z_i)^3 + c_4(t)(z_{i-1} - z_i)^4 \\
\Phi(z_i, t) &= c_0(t) && (2.82c)\\
\Phi(z_{i+1}, t) &= c_0(t) + c_1(t)(z_{i+1} - z_i) + c_2(t)(z_{i+1} - z_i)^2 && (2.82d)\\
&\quad + c_3(t)(z_{i+1} - z_i)^3 + c_4(t)(z_{i+1} - z_i)^4 \\
\Phi(z_{i+2}, t) &= c_0(t) + c_1(t)(z_{i+2} - z_i) + c_2(t)(z_{i+2} - z_i)^2 && (2.82e)\\
&\quad + c_3(t)(z_{i+2} - z_i)^3 + c_4(t)(z_{i+2} - z_i)^4 \ ,
\end{aligned}$$

for the second derivative

$$\partial_{zz}\Phi(z_i, t) \approx 2c_2(t, \Phi(z_{i-2}), \cdots, \Phi(z_{i+2})) \ . \tag{2.83}$$

Our task is now to calculate $c_2(t, \Phi(z_{i-2}), \cdots, \Phi(z_{i+2}))$ for the required gridpoints z_i. Since we apply the MOL, the time dependency of c_2 in (2.83) is the same for all timesteps, and we will therefore concentrate on the spatial part of c_2 in the imminent calculations.

To be able to solve the system (2.82) we need to establish what the factors $(z_j - z_i)$ are around the PML points, and in essence there are three possibilities:

1. Both z_i and z_j are outside the PML region.

2. Both z_i and z_j are inside the PML region.

3. Either z_i is inside the PML region and z_j on the outside, or the contrary.

In all cases we have

$$m < i \text{ such that } x_m < x_i \,, \tag{2.84a}$$

$$n > i \text{ such that } x_n > x_i \,, \tag{2.84b}$$

$$\tag{2.84c}$$

and we define

$$|m - i| = k_1 \,, \tag{2.85a}$$

$$|n - i| = k_2 \,, \tag{2.85b}$$

where $m, n, i \in \mathbb{Z}$ and $k \in \mathbb{N}$.

1. Both z_j and z_i are outside the PML region.

$$\begin{aligned} z_m - z_i &= x_m - x_i \\ &= -k_1 \Delta x \end{aligned} \tag{2.86a}$$

$$\begin{aligned} z_n - z_i &= x_n - x_i \\ &= k_2 \Delta x \end{aligned} \tag{2.86b}$$

2. Both z_j and z_i are are inside the PML region. For simplicity we combine the discretized equations for $z(x)^+$ and $z(x)^-$ such that

$$z_i^{\mp} = z(x_i)^{\mp} = \mp a + e^{i\theta}(x_i \pm a) \tag{2.87}$$

The factor difference relations then reads

$$z_m^{\mp} - z_i = [\mp a + e^{i\theta}(x_m \pm a)] - [\mp a + e^{i\theta}(x_i \pm a)] \tag{2.88a}$$

$$= e^{i\theta}(x_m - x_i) \tag{2.88b}$$

$$= -k_1 \Delta x e^{i\theta} \,, \tag{2.88c}$$

$$\begin{aligned}
z_n^{\mp} - z_i &= [\mp a + e^{i\theta}(x_n \pm a)] - [\mp a + e^{i\theta}(x_i \pm a)] && (2.89\text{a})\\
&= e^{i\theta}(x_n - x_i) && (2.89\text{b})\\
&= k_2 \Delta x e^{i\theta} \ . && (2.89\text{c})
\end{aligned}$$

Hence, the factors $(z_j - z_i)$ are just multiples of Δx times the complex factor $e^{i\theta}$.

3. If one point lies inside the PML region and the other on the outside, there are two cases.

   (a) z_i sits on the complex branch of $z(x)$, while z_j is on the real.

   (b) z_j sits on the complex branch of $z(x)$, while z_i is on the real.

   In the presented calculations $x_M^{\mp}$ denotes the PML points $\mp a$.

   (a) $z_i \in z(x)^{\mp}$ while $z_j \in (-a, a)$:

$$\begin{aligned}
z_j - z_i &= x_j - z_i && (2.90\text{a})\\
&= x_j - [\mp a + e^{i\theta}(x_i \pm a)] && (2.90\text{b})\\
&= x_j - [z_M^* + e^{i\theta}(x_i - z_M^*)] && (2.90\text{c})\\
&= (x_j - x_M^*) - e^{i\theta}(x_i - x_M^*) \ , && (2.90\text{d})
\end{aligned}$$

   where $j = n$ and $x_M^* = x_M^-$ at the negative PML region, while $j = m$ and $x_M^* = x_M^+$ at the positive PML region.

   (b) $z_i \in (-a, a)$ while $z_j \in z(x)^{\mp}$

$$\begin{aligned}
z_j - z_i &= z_j - x_i && (2.91\text{a})\\
&= [\mp a + e^{i\theta}(x_j \pm a)] - x_i && (2.91\text{b})\\
&= [z_M^* + e^{i\theta}(x_j - z_M^*)] - x_i && (2.91\text{c})\\
&= (x_M^* - x_i) + e^{i\theta}(x_j - x_M^*) \ , && (2.91\text{d})
\end{aligned}$$

where $j = m$ and $x^*_M = x^-_M$ for the negative PML region, while $j = n$ and $x^*_M = x^+_M$ for the positive PML region.

Taking use of the presented factors $(z_j - z_i)$, the solution of system (2.82) leads to the approximations

$$\partial_{zz}\Phi(z_i, t) \approx \frac{1}{\Delta x^2}\left(\eta_{i-2}\Phi_{i-2} + \eta_{i-1}\Phi_{i-1} + \eta_i\Phi_i + \eta_{i+1}\Phi_{i+1} + \eta_{i+2}\Phi_{i+2}\right) \tag{2.92}$$

where z_i and η_i are stated in table 2.3.

	Coefficients				
Gridpoint rule	η_{i-2}	η_{i-1}	η_i	η_{i+1}	η_{i+2}
Z_{M^--1}	$-\frac{e^{-i\theta}}{3(3e^{i\theta}+1)}$	$\frac{(3e^{i\theta}+1)e^{-2i\theta}}{(2e^{i\theta}+1)}$	$-\frac{(3e^{i\theta}+2)e^{-2i\theta}}{(e^{i\theta}+1)}$	$\frac{e^{-2i\theta}}{3}\left(e^{i\theta}+3\right)$	$-\frac{2e^{2i\theta}}{(6e^{3i\theta}+11e^{2i\theta}+6e^{i\theta}+1)}$
Z_{M^-}	$\frac{(-3e^{i\theta}+2)e^{-2i\theta}}{2(2e^{2i\theta}+3e^{i\theta}+1)}$	$\frac{2(6e^{i\theta}-2)e^{-2i\theta}}{(e^{2i\theta}+3e^{i\theta}+2)}$	$\frac{e^{-2i\theta}}{2}\left(2e^{2i\theta}-9e^{i\theta}+2\right)$	$\frac{2(-2e^{i\theta}+6)e^{i\theta}}{(2e^{2i\theta}+3e^{i\theta}+1)}$	$\frac{(2e^{i\theta}-3)e^{i\theta}}{2(e^{2i\theta}+3e^{i\theta}+2)}$
Z_{M^-+1}	$-\frac{2e^{-i\theta}}{(e^{3i\theta}+6e^{2i\theta}+11e^{i\theta}+6)}$	$\frac{e^{-i\theta}}{3}\left(3e^{i\theta}+1\right)$	$-\frac{2e^{i\theta}+3}{(e^{i\theta}+1)}$	$\frac{e^{i\theta}+3}{(e^{i\theta}+2)}$	$-\frac{1}{3(e^{i\theta}+3)}$
Z_{M^+-1}	$-\frac{1}{3(e^{i\theta}+3)}$	$\frac{e^{i\theta}+3}{(e^{i\theta}+2)}$	$-\frac{2e^{i\theta}+3}{(e^{i\theta}+1)}$	$\frac{e^{-i\theta}}{3}\left(3e^{i\theta}+1\right)$	$-\frac{2e^{-i\theta}}{(e^{3i\theta}+6e^{2i\theta}+11e^{i\theta}+6)}$
Z_{M^+}	$\frac{(2e^{i\theta}-3)e^{i\theta}}{2(e^{2i\theta}+3e^{i\theta}+2)}$	$\frac{2(-2e^{i\theta}+6)e^{i\theta}}{(2e^{2i\theta}+3e^{i\theta}+1)}$	$\frac{e^{-2i\theta}}{2}\left(2e^{2i\theta}-9e^{i\theta}+2\right)$	$\frac{2(6e^{i\theta}-2)e^{-2i\theta}}{(e^{2i\theta}+3e^{i\theta}+2)}$	$\frac{(-3e^{i\theta}+2)e^{-2i\theta}}{2(2e^{2i\theta}+3e^{i\theta}+1)}$
Z_{M^++1}	$-\frac{2e^{2i\theta}}{(6e^{3i\theta}+11e^{2i\theta}+6e^{i\theta}+1)}$	$\frac{e^{-2i\theta}}{3}\left(e^{i\theta}+3\right)$	$-\frac{(3e^{i\theta}+2)e^{-2i\theta}}{(e^{i\theta}+1)}$	$\frac{(3e^{i\theta}+1)e^{-2i\theta}}{(2e^{i\theta}+1)}$	$-\frac{e^{-i\theta}}{3(3e^{i\theta}+1)}$

Table 2.3: Difference constants associated with the six difference rules around the PML points for the second derivative with a fourth order accuracy.

With the presented procedure we are able to represent the $PML^{\pm}$ blocks in the matrix (2.71), and the operator $\mathcal{L}$ (2.65) is represented on the entire discretized contour. We note that these difference rules by no means are calculated by hand, but are produced from a script that does all the symbolic work.

2.4.5 The numerical solution

Now we apply the MOL with the specified matrix operator (2.71), the initial condition (2.7b) defined on $z(x)$, and the constants in table 2.4 to produce the solution depicted in figure 2.12. The figures illustrate that the real part of the solution $\phi(x,t)$ travels towards the positive PML point, and goes to zero. Hence, the theory concerning the PML holds, and the analytical work we have done applies.

k_0	a	M	N	Δx	θ	t_{min}	t_{max}	Δt	σ
5	10	75	150	2/15	$\pi/2$	0	10	0.05	0.5

Table 2.4: Fourier and Difference comparison constants for the RSE

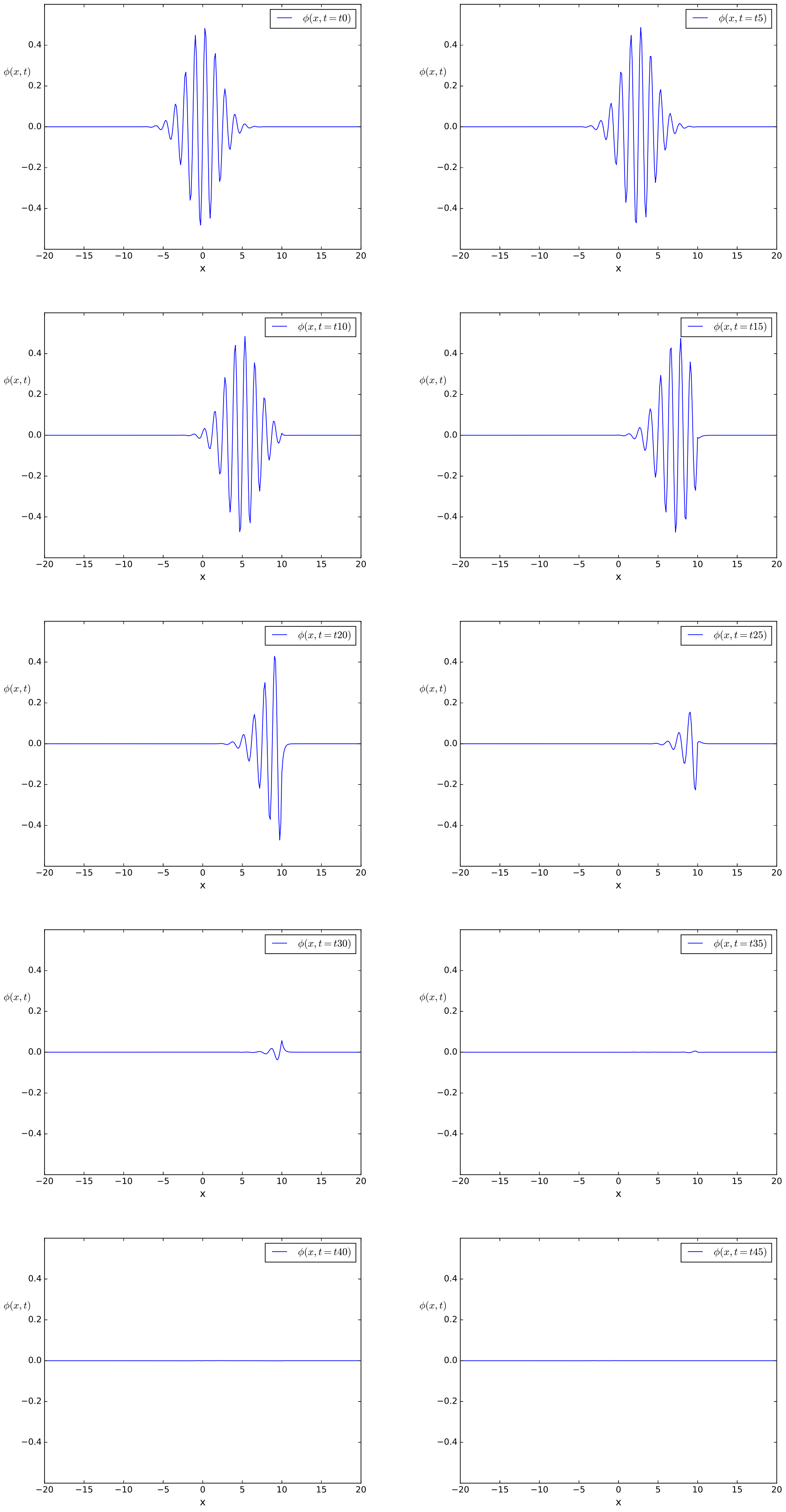

Figure 2.12: Solution of the RSE with the PML enfocred.

3

A pattern forming system

Now that we have achieved some mathematical-numerical methods and techniques, we are equipped to wander the landscape of pattern forming equations and dynamics. As one reads from the introduction, the terrain of this landscape is an overwhelming one, and to be able to apply the obtained machinery, we are throughout the thesis to work in a mathematical laboratory containing one spatial dimension in addition to time. In the following studies we will investigate a single model, the Swift-Hohenberg equation.

3.1 The Swift Hohenberg equation

We start by reacalling the Swift - Hohenberg equation(SHE):

$$u_t = ru - (1 + \nabla^2)^2 u + N(u) \ , \tag{3.1}$$

a model equation thoroughly discussed in [1], which the material in the upcoming paragraphs and subsection 3.2 originates from.

Historically, the equation was developed in 1977 to investigate to what extent the nonequilibrium transition from a uniform to a nonuniform convecting state were similar to a phase transition. As time went by and technology made numerical computations more accessible, one discovered that the equation could produce solutions with rich spatiotemporal dynamics, which in turn led to the SHE as a model of pattern forming systems.

The SHE is a so called generated model equation, since it is a result of a heuristic derivation using explicit criteria like symmetry arguments to embed "physical properties" into the equation. In that manner, the SHE does not model a specific physical system, rather several different systems. The equation is thus designed to imitate various non equilibrium systems where its solutions are evolving patterns, like the ones observed in Rayleigh-Benard convection. A consequence of this imposed "physical nature", is that the SHE is fruitful to investigate when one are to assay the mathematics of pattern forming systems.

The one dimensional version of the SHE we want to consider throughout the thesis reads

$$\begin{aligned} u_t &= ru - (1 + \partial_{xx})^2 u - u^3 \\ u(x, 0) &= f(x) \\ x &\in (-L, L) \,, \end{aligned} \tag{3.2}$$

where L can be finite or infinite, $u = u(x, t)$, r is the control parameter of the system, $f(x)$ the initial condition, and $-u^3$ the non-linearity. If L is infinite the boundary conditions reads

$$u(\pm L, t) = 0 \tag{3.3a}$$

$$u_x(\pm L, t) = 0 \,, \tag{3.3b}$$

whereas periodic conditions

$$u(x, t) = u(x + 2L, t) \tag{3.4a}$$

$$u_x(x, t) = u_x(x + 2L, t) \tag{3.4b}$$

apply for finite L. Other conditions may apply[1], but (3.3b) - (3.4) are the default conditions.

3.2 Linear stability analysis of the SHE

By observation we establish a solution to (3.2) from the trivial solution $u_b = 0$, that we will refer to as a base solution. A small perturbation $u \rightarrow u + u_b$ around the base solution can be shown to result in the linearized SHE (3.5).

$$u_t = ru - (1 + \partial_{xx})^2 u \tag{3.5}$$

To develop useful terminology and understanding of how the SHE evolves with time relative to a small perturbation, we will explore the linear perturbed part of the SHE by playing with formulas and equations. The main calculations and overall conclusions presented in this subsection are as mentioned similarly discussed in [1], but our analysis contain some modifications to the original script.

Equation (3.5) is a linear PDE with constant coefficients, whose solution might be a standard mode on the form

$$u(x,t) = Ae^{\sigma t} e^{\xi x} \ , \tag{3.6}$$

where σ and ξ are arbitrary constants. Inserting (3.6) into (3.5) results in the algebraic equation

$$\sigma = r - (\xi^2 + 1)^2 \ , \tag{3.7}$$

that can be satisfied for some σ, r and ξ. To establish the nature of ξ and σ we analyse how $u(x,t)$ (3.6) behaves relative to the parameters, under the assumption of a small perturbation $u(x,t)$.

The behaviour of ξ is determined by investigating how the spatial part of $u(x,t)$ changes if the domain is finite or infinite.

[1] i.e $u_{xx}(\pm L, t) = 0$ or $u_{xx}(x,t) = u_{xx}(x+2L, t)$, for the infinite and finite case respectively

- Infinite boundaries: if $x \to \pm\infty$ in (3.6) a real, non zero ξ would make the spatial part of $u(x,t)$ grow out of bounds on either side, contradicting the assumption of a small perturbation around u_b. The same applies if $\xi = a + ib$, only that such a ξ will force $u(x,t)$ to oscillate towards $\pm\infty$. If ξ is purely imaginary, $\xi = ik$ where $k \in \mathbb{R}$, the spatial part of $u(x,t)$ does not grow exponentially for any x, which is consistent relative to the perturbation.

- Periodic boundaries: if $u(x,t)$ is $2L$ periodic for finite L, we demand that the solution is the same at all positions x and $x + 2L$, at all times. Hence, the relations

  $$u(x,t) = u(x+2L,t) \tag{3.8a}$$
  $$Ae^{\sigma t}e^{\xi x} = Ae^{\sigma t}e^{\xi(x+2L)} \tag{3.8b}$$
  $$1 = e^{2\xi L}\,, \tag{3.8c}$$

  emerge, which results in the formula

  $$\xi = m\frac{i\pi}{L}, \qquad m \in \mathbb{Z} \tag{3.9}$$

  for ξ. Since ξ in (3.9) is a imaginary number, we denote $\xi = ik$ and write

  $$k_m = m\frac{\pi}{L}\,, \quad m \in \mathbb{Z}\,, \tag{3.10}$$

  where k_m is a discrete countable set. With this, the mode solution (3.6) holds for one k_m, and is consistent under the assumption of a small perturbation around u_b.

To summarize, we can for finite and infinite L write $\xi = ik$, such that (3.7) reads

$$\sigma_k = r - (1-k^2)^2\,, \tag{3.11}$$

for some k. The stated relations and equations imply that the perturbation $u(x,t)$ is on the form

$$u(x,t) = Ae^{\sigma_k t}e^{ikx}\,, \tag{3.12}$$

where we recognise k as the wavenumber, and σ_k as the growth rate of a oscillating Fourier mode. The superposition principle for linear PDEs results in the Fourier series and transform

$$u(x,t) = \sum_{k_m} c_k e^{\sigma_{k_m} t} e^{ik_m x} \,, \tag{3.13}$$

$$u(x,t) = \int_{\mathbb{R}} \mathrm{d}k \; e^{\sigma_k t} e^{ikx} \,, \tag{3.14}$$

for the periodic discrete and infinite continuous domain respectively.

To ensure that the solutions $u(x,t)$ (3.13) - (3.14) are small and decays in the limit $t \to \infty$, the criteria for σ_k emerge as

$$\max_k \text{Re } \sigma_k < 0, \tag{3.15}$$

which by observation holds for $r \in \mathbb{R}^-$.

3.2.1 Growth rate behaviour

To determine how the perturbation $u(x,t)$ evolves with time, we are to investigate how the growth rate σ_k (3.11) changes for varying k and r. As a first remark, we note that σ_k is a real number for all wave numbers k, and could be interpreted as a real valued parameter function $\sigma(k)$ for the variable k, and the varying parameter r. Furthermore we denote that if $k \to \pm\infty$, then $\sigma(k)$ describes a monotonically decreasing function, which ensures a decaying behaviour of the perturbation $u(x,t)$. Figure 3.1 illustrates the growth rate function for small k with different of r. If $r \in (0,1)$ the zeros of $\sigma(k)$ are given by

$$k_2^- = -\sqrt{1+\sqrt{r}} \quad \text{and} \quad k_1^- = -\sqrt{1-\sqrt{r}} \tag{3.16a}$$

$$k_1^+ = \sqrt{1-\sqrt{r}} \quad \text{and} \quad k_2^+ = \sqrt{1+\sqrt{r}} \,, \tag{3.16b}$$

and they are distributed along the k-grid as depicted in figure 3.2. If $r > 1$ the $k_1^\pm$ roots goes imaginary, and we are left with the real $k_2^\pm$ roots. This behaviour

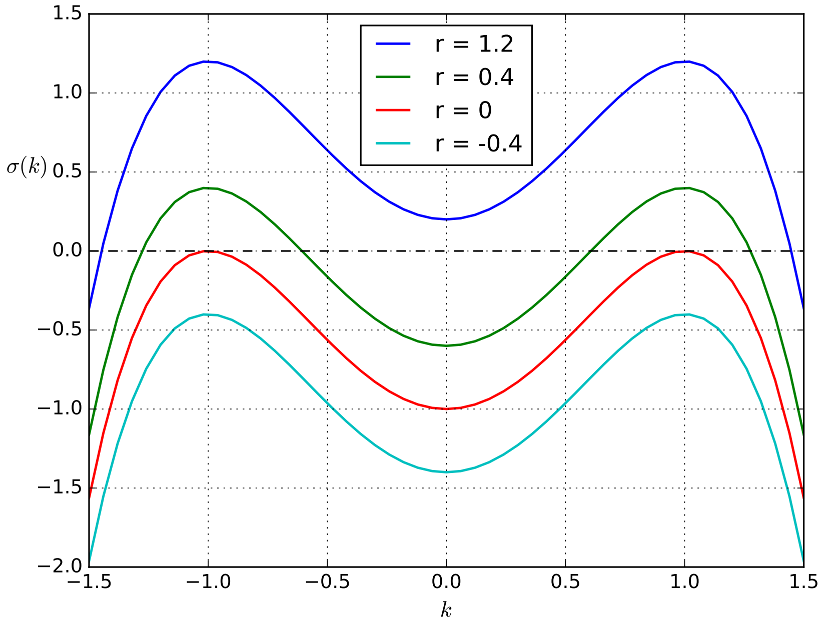

Figure 3.1: The growth rate $\sigma(k)$ for different values of r.

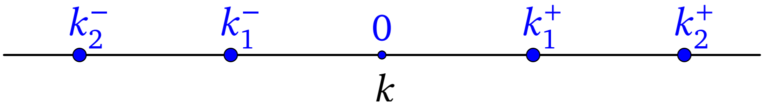

Figure 3.2: The zeros of the Swift Hohenberg Equation if $0 < r < 1$.

is illustrated in figure 3.1, where the image of $\sigma(k)$ elevates with increasing r, while the real $k_1^\pm$ roots disappears as $r \rightarrow 1$.

The derivative of $\sigma(k)$ reads

$$\sigma'(k) = -4k(k^2 - 1) \ , \tag{3.17}$$

and reveal the global maxima at $k = \pm 1$, as already predicted by the image of $\sigma(k)$. This imply that the maximum values of $\sigma(k)$ are given by

$$\max_k \sigma(k) = r \ , \tag{3.18}$$

since the term $(k^2 - 1)^2$ in (3.11) goes to zero at $k = \pm 1$.

From (3.18) we conclude that the solution $u(x, t)$ around the base state u_b is linearly stable when $r < 0$, linearly unstable for $r > 0$, and that the threshold of instability is given by the critical value $r_c = 0$. Furthermore, we define the corresponding critical wavenumber as $k_c = 1$, since the global maxima of $\sigma(k)$ occurs at $k = 1$ for all r. [2] From figure 3.1 and equation (3.17) we conclude that wavenumbers in the neighbourhood of k_c ensures growing spatial modes, and that those modes grow much slower than the decaying modes corresponding to large wavenumbers $|k| >> k_c$.

In summary, the outcome of this linear stability analysis suggests that a small perturbation around the base state u_b with $r > r_c$ results in some form of spatiotemporal evolution for the linear SHE (3.5) due to the positive growth rates for some wavenumbers. From PDE theory we know that Fourier solutions with positive growth rates results in exploding solutions as $t \to \infty$, which therefore suggest that the perturbed solution $u(x, t)$ are to grow out of bounds. However, the full SHE (3.2) is equipped with a negative nonlinearity, which at the end of the day ensures a bounded dynamical spatiotemporal behaviour.

3.3 A perfectly matched layer for the Swifth Hohenberg equation

Inspired by the results in section 2.4, we now want to enforce a PML on the SHE (3.2), and build a numerical scheme to solve the transformed equation with the MOL.

To achieve this, we will perform the same routine on the SHE as we did for the

---

2. We do not include both signs for the established wave number since the absolute value for both k-roots are 1. The sign only describes direction relative to the associated wave vector in 2 and 3 dimensions, that in one dimension corresponds to wave a travelling in either the positive or negative direction.

RSE; apply some complex analysis to find a PML version of the SHE, establish the nature of the differential operators, choose a suitable discretization, and build the numerical approximation for the spatial part of the equation.

3.3.1 Converting the SHE to a PML equation

Recalling subsection 2.3.2 and the results concerning combinations of numerical differential operators, we rewrite the SHE (3.2) as

$$u_t = (r-1)u - (2\partial_{xx} + \partial_{xxxx})u - u^3 \ , \tag{3.19}$$

to avoid computational errors.

The necessary calculations to transform (3.19) into a PML equation are more or less identical to the ones in subsection 2.4, and are therefore not included in detail here. We write the required few, and present the main features of the imminent calculations by words and a somewhat precise hand waving.

By defining the analytic continuation of $u(x,t)$ as $U\,|_{\mathbb{R}} = u$ where $U = U(z,t)$, the equation

$$U_t = (r-1)U - (2\partial_{zz} + \partial_{zzzz})U - U^3 \ , \tag{3.20}$$

is analogous to (3.19) for the analytic continuation $U(z,t)$. The function

$$\Psi(x,t) = U(z,t)\,\big|_{z=z(x)} \tag{3.21}$$

is a solution of (3.20) along some complex contour $z(x)$, and we want to express the spatiotemporal derivatives of (3.20) in terms of $\Psi(x,t)$. Using the same contour (2.51) as for the RSE, and an industrious practice of the chain rule similar to the manipulations in (2.59) - (2.60), one can derive equations for U_z, U_{zz}, U_{zzz} and U_{zzzz} expressed by Ψ_x, Ψ_{xx}, Ψ_{xxx}, and Ψ_{xxxx}. These relations contain derivatives of $z(x)$, as (2.61) and (2.62), whereby everything simplifies due the zero derivatives of $z^{(n)}(x)$ when $n \geq 2$. By the stated procedure, the second and fourth "spatial" complex derivative in (3.20) turn out as

$$U_{zz} = \frac{\Psi_{xx}}{[z'(x)]^2} \tag{3.22a}$$

$$= e^{-2i\theta}\Psi_{xx} \, , \tag{3.22b}$$

$$U_{zzzz} = \frac{\Psi_{xxxx}}{[z'(x)]^4} \tag{3.22c}$$

$$= e^{-4i\theta}\Psi_{xxxx} \, . \tag{3.22d}$$

If we combine the stated pieces of theory, the PML version of the SHE emerges as

$$\Psi_t = [(r-1) - \mathcal{L}]\Psi - \Psi^3 \, , \tag{3.23}$$

which we from now will refer to as the PMLSHE. The differential operator $\mathcal{L}$ in (3.23) reads

$$\mathcal{L} = \begin{cases} \frac{2}{e^{2i\theta}}\Psi_{xx} + \frac{1}{e^{4i\theta}}\Psi_{xxxx} & \text{for } x < -a \\ 2U_{zz}\big|_{z=z(x)} + U_{zzzz}\big|_{z=z(x)} & \text{for } x = -a \\ 2\Psi_{xx} + \Psi_{xxxx} & \text{for } x \in (-a, a) \\ 2U_{zz}\big|_{z=z(x)} + U_{zzzz}\big|_{z=z(x)} & \text{for } x = a \\ \frac{2}{e^{2i\theta}}\Psi_{xx} + \frac{1}{e^{4i\theta}}\Psi_{xxxx} & \text{for } x > a \, , \end{cases} \tag{3.24}$$

and the initial and boundary conditions are given by the relation

$$\begin{aligned} \Psi(x,0) &= f(x) \\ \Psi(\pm L, t) &= 0 \\ \Psi_x(\pm L, t) &= 0 \\ x &\in (-L, L) \, , \end{aligned} \tag{3.25}$$

where L can be both finite and infinitely large.

Due to the fact that $z(x)$ is neither twice nor four times continuous differentiable at the PML points - as one has to assume to perform the previous mentioned chain rule bonanza - the derivatives ∂_{xx} and ∂_{xxxx} need to be specified in terms of the analytic continuation $U(z(x), t)$ at those points. Such a procedure is discussed in section 1.4, and the routine is the same this time around.

The intention of this setup is that the PMLSHE are to produce solutions with spatiotemporal dynamics outside the PML region for $r > 0$, while the solutions decays symmetrically from the PML points and into PML regions, long before it reaches the endpoint of L. In that manner, finite L can be interpreted as periodic boundary conditions. This idea is illustrated in figure 3.3, but we remark that this imagery is much more an idea, than rigorous mathematics.

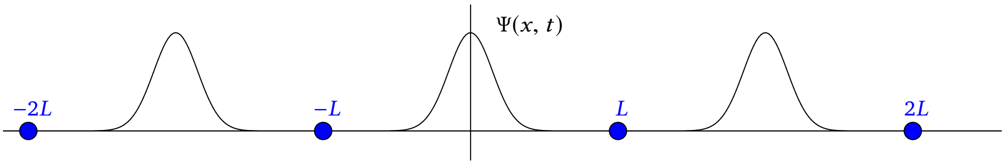

Figure 3.3: The idea of periodic boundary conditions for the PML setup.

Since the PMLSHE (3.23), and the corresponding differential operator (3.24) is a quite complex collection of expressions, we want to simplify our notation. By introducing the step function

$$\theta(x) = \begin{cases} \theta_N & \text{for } x < -a \\ 0 & \text{for } x \in (-a, a) \\ \theta_P & \text{for } x > a\,, \end{cases} \tag{3.26}$$

as depicted in figure 3.4, where θ_N and θ_P are the $z(x)$-contour angles defined

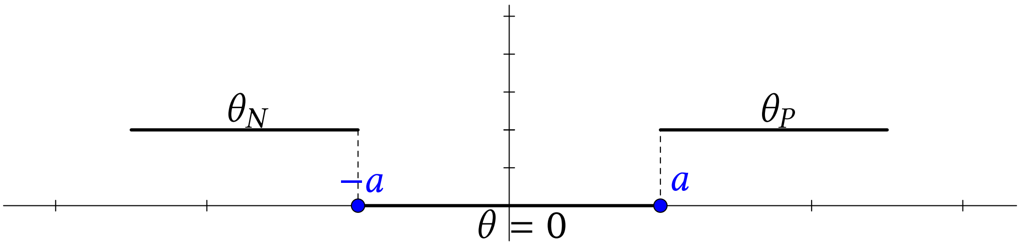

Figure 3.4: The step function $\theta(x)$

on the interval

$$\{\theta_N, \theta_P\} \in \left[0, \frac{\pi}{2}\right] , \tag{3.27}$$

we present the more compact version of the PMLSHE

$$\Psi_t = [r - (1 + 2e^{-2i\theta(x)}\partial_{xx} + e^{-4i\theta(x)}\partial_{xxxx})]\Psi - \Psi^3 \,. \tag{3.28}$$

Note that (3.28) in general not is analogous to (3.23) due to the discontinuities at the PML points, but behaves like (3.23) at all other spatial points. However, if θ is constant over the whole line, where θ is a constant in the interval $(0, \frac{\pi}{2})$, then (3.28) and (3.23) describe the same system.

3.4 Discretization, numerical representations of operators, and numerics for the SHE with a PML

As a first remark concerning the numerics of the PMLSHE (3.23), we want to discuss the number of necessary gridpoints to approximate the differential operators contained in the operator $\mathcal{L}$ (3.24). Contrary to the rSE, that contained one differential operator, the transformed SHE (3.23) inheres a sum of two differential operators. To sustain the same order of accuracy for both terms, the difference rules corresponding to each term should be approximated with the number of gridpoints as stated in table 3.1. One must not demand the same order of accuracy for both operators, but since the differential operator with the lowest precision dictates the precision of the solution $\Psi(x, t)$, we choose this setup for consistency.

	∂_{xx}		∂_{xxxx}	
Order of accuracy	2	4	2	4
# of gridpoints, CDM	3	5	5	7
# of gridpoints, boundary rules	4	6	6	8

Table 3.1: Number of required gridpoints to approximate the second and fourth spatial derivative for two different orders of accuracy.

Applying the same discretization as for the RSE

$$\Delta x = \frac{a}{M} \tag{3.29a}$$

$$L = \Delta x \cdot N \tag{3.29b}$$

$$x_l = l \cdot \Delta x \qquad l \in (-N, N) \,, \tag{3.29c}$$

we again ensure that the PML points are on the grid. If we represent the spatial domain with the vector

$$\boldsymbol{\Psi} = \left[\Psi(x_{-N}, t) \quad \Psi(x_{-N+1}, t) \quad \cdots \quad \cdots \quad \Psi(x_N, t)\right]^T \,, \tag{3.30}$$

and denote it as Ψ_l for $l \in [-N, N]$, the PMLSHE (3.23) can be turned into a ODE system like (2.9) by the relation

$$\Psi_l' = \sum_{s=-N}^{N} M_{ls} \Psi_s - (\Psi_l)^3 \,. \tag{3.31}$$

The non-linearity[3] in (3.31) is implemented into the MOL routine by changing the return statement of the *RHS* function in listing 2.1, to the one described in listing 3.1.

Listing 3.1: Pseudo code of the right hand side subroutine for the MOL with a non linearity

```
def RHS(time, psi)
        return dotproduct(M, psi) - psi**3
```

M_{ls} in (3.31) represents the system operator differential matrix (SODM), which is defined as

$$M(r, \theta) = (r - 1) I_d - L(\theta) \,, \tag{3.32}$$

where r is the control parameter and θ denotes the contour angle given by $z(x)$. I_d specifies the identity matrix, and $L(\theta)$ represents the differential operator $\mathcal{L}$ (3.24) for the angle θ. The operator $L(\theta)$ reads

$$L(\theta) = 2\mathcal{D}_2(\theta) + \mathcal{D}_4(\theta) \,, \tag{3.33}$$

---

[3] $(\Psi_l)^3$ is to be read as raising each component of Ψ_l to the third power.

where $\mathcal{D}_2(\theta)$ and $\mathcal{D}_4(\theta)$ are on the block matrices form (2.71), and contains difference rules for all spatial points. In appendix A both $\mathcal{D}_2$ and $\mathcal{D}_4$ are independently tested and verified for different functions and angles.

Since the discretized system obviously is defined on at finite interval, we implement the required grid and operator manipulations[4] to satisfy the assumed boundary conditions in (3.25). With this, we have a complete discretized version of the PMLSHE, and we are now ready to solve both the regular and the PML transformed SHE.

3.5 Numerical solutions

3.5.1 The standard SHE

Since our entire numeric scheme is based on the contour $z(x)$ (2.51), we let $\theta = 0$ such that $z(x)$ describes the x-axis, while the transformed system (3.23) - (3.25) collapses into the regular SHE (3.2), with (3.19) as the governing equation.

We are with this setup able to test if the numerical scheme produces the expected outcome for the standard SHE (3.2), which according to theory is one dimensional stripes[1]. This is actually a "kill two birds in one stone" situation, since we are to perform a first test on the numerical scheme, and establish the nature of $u(x, t)$ for the regular SHE. If the numerics do not portray the expected outcome, we know something is wrong in our setup, and we are sent back to the drawing board.

Applying white noise and a gaussian function as initial conditions, together with the constants in table 3.2, our scheme produces the results depicted in figure 3.5 and 3.6 for the regular SHE. Note that the figures reads left to right,

---

[4] Note that these manipulations imply the index shift $N \to N - 1$ for the summation (3.31).

and downwards.

a	M	N	Δx	θ	t_{min}	t_{max}	Δ t	r	L
10	150	500	1/15	0	0	15000	2	0.5	100/3

Table 3.2: Constants in the MOL scheme of the PMLSHE for different values of θ.

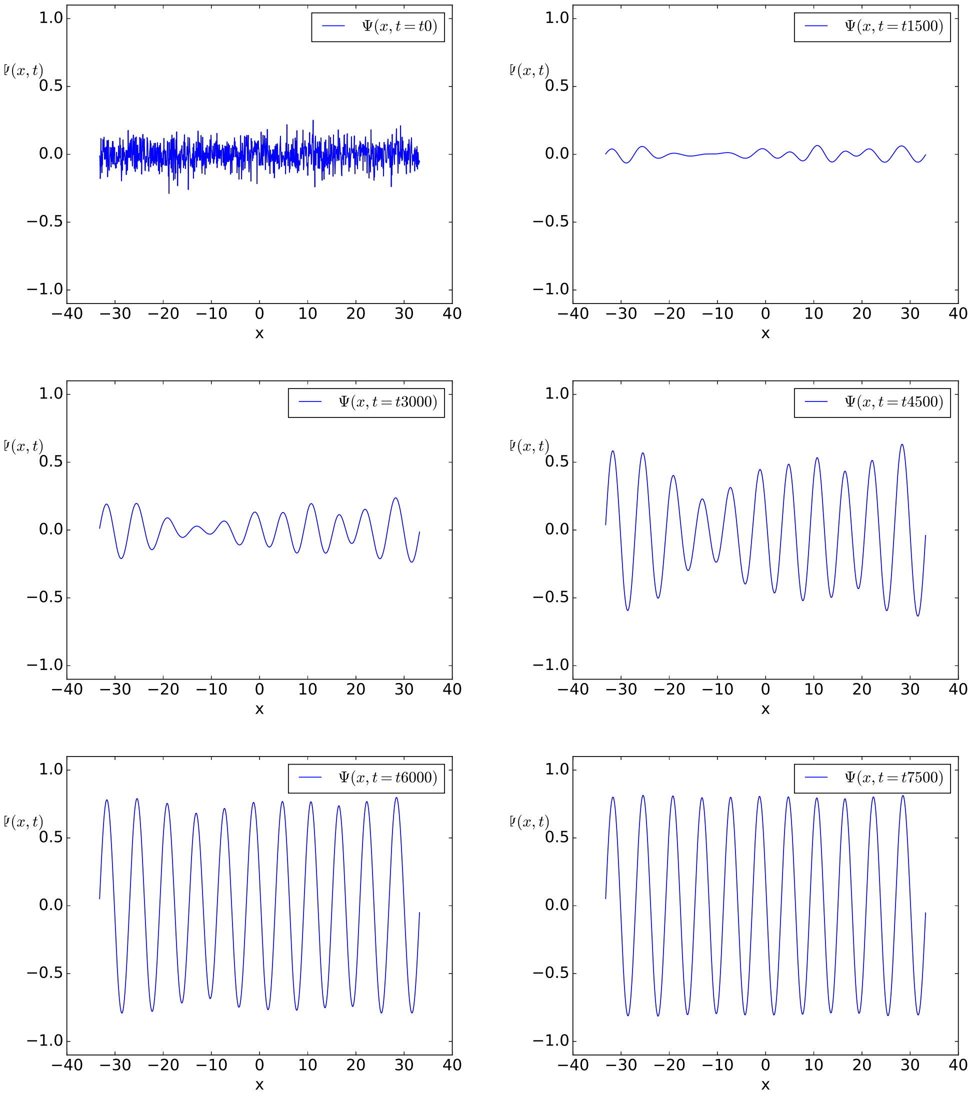

Figure 3.5: Solution of the standard SHE with white noise as the initial condition.

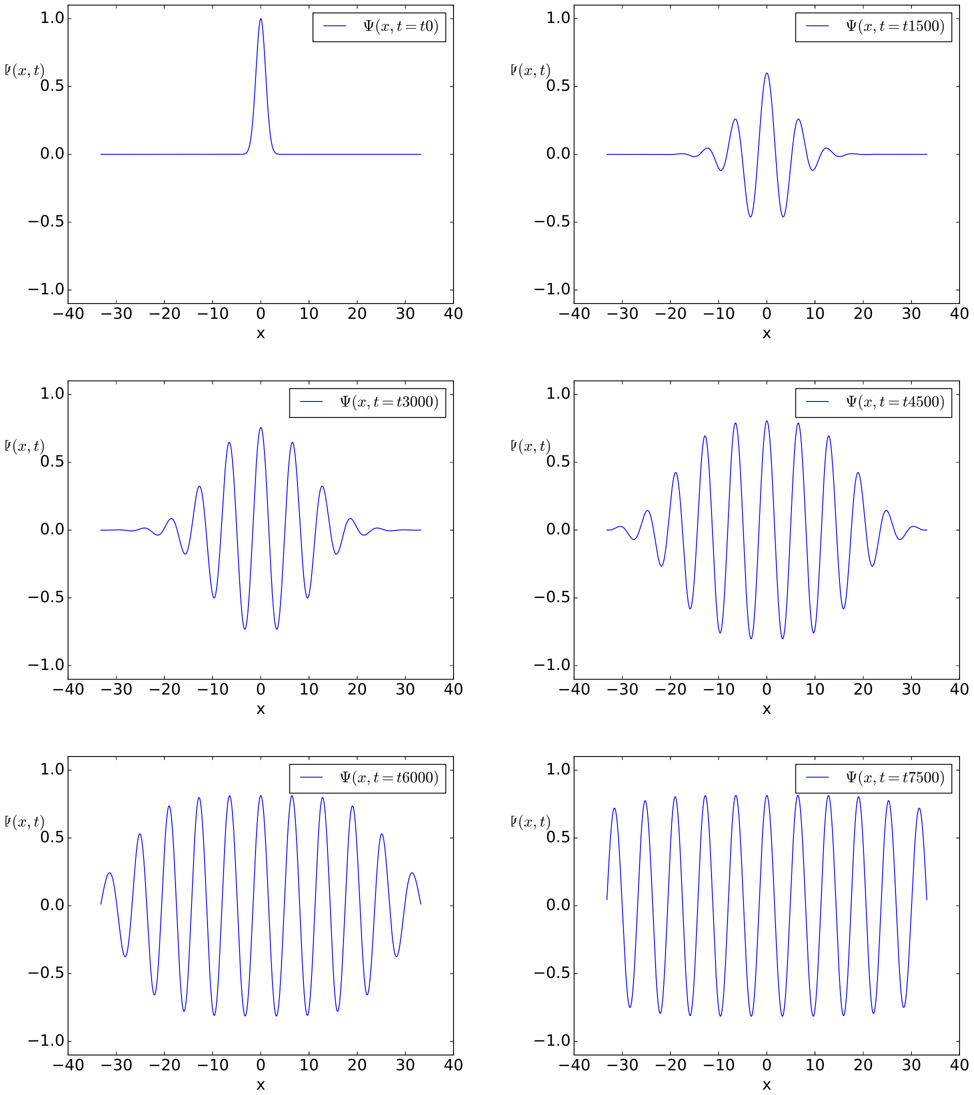

Figure 3.6: Solution of the standard SHE with the the initial condition $e^{-\frac{(x-x_0)^2}{2}}$ around $x_0 = 0$.

At first glance, the solution $u(x,t)$ seems to be a ordinary sinusoidal function for large t, but this exactly what we should expect. To understand why, imagine that the extremal values of a solution $u(x, t = t_{\text{lage}})$ takes one color at the peaks, and another at the bottoms. Then imagine that the solution was stretched inwards or outwards from the paper plane, and visualize the solution by looking at it from above. The result would then illustrate two dimensional stripes. Even tough this explanation is ad hoc, we conclude that the numerical scheme has passed its first naive test, since it produces the expected outcome in form of one dimensional stripes. We are also to observe one of the more subtle pieces of unsaid theory from this simulation: the same pattern appears from different initial conditions. The onset pattern and evolution of $u(x,t)$ is not the same in both figures, but both solutions turn into a regular "striped state" around the same time.

3.5.2 The SHE with a PML

Now that we have established the solution of the standard SHE, we step up our game and turn to the PMLSHE (3.23). Our intention is that the numerical scheme are to produce "sinusodal" stripes as observed for the standard SHE outside the PML region, while the solution decays exponentially from the PML points, and goes to zero inside the PML region. Applying a white noise initial condition, the angles $(\theta_1, \theta_2, \theta_3) = (\frac{\pi}{8}, \frac{\pi}{4}, \frac{\pi}{2})$, and the constants in table 3.2, results in the solutions illustrated in figure 3.7 to 3.9 respectively.

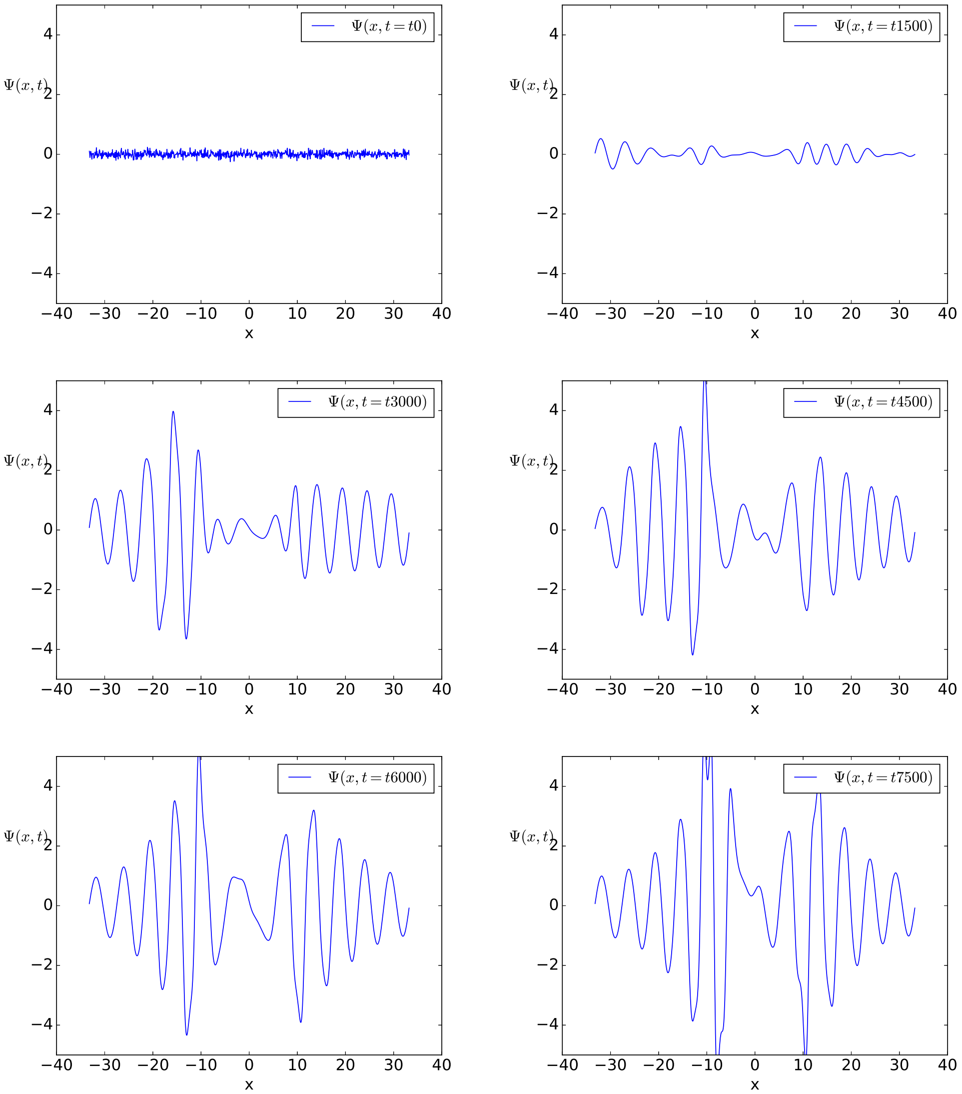

Figure 3.7: Solutions of the PMLSHE with $\theta_1 = \frac{\pi}{8}$.

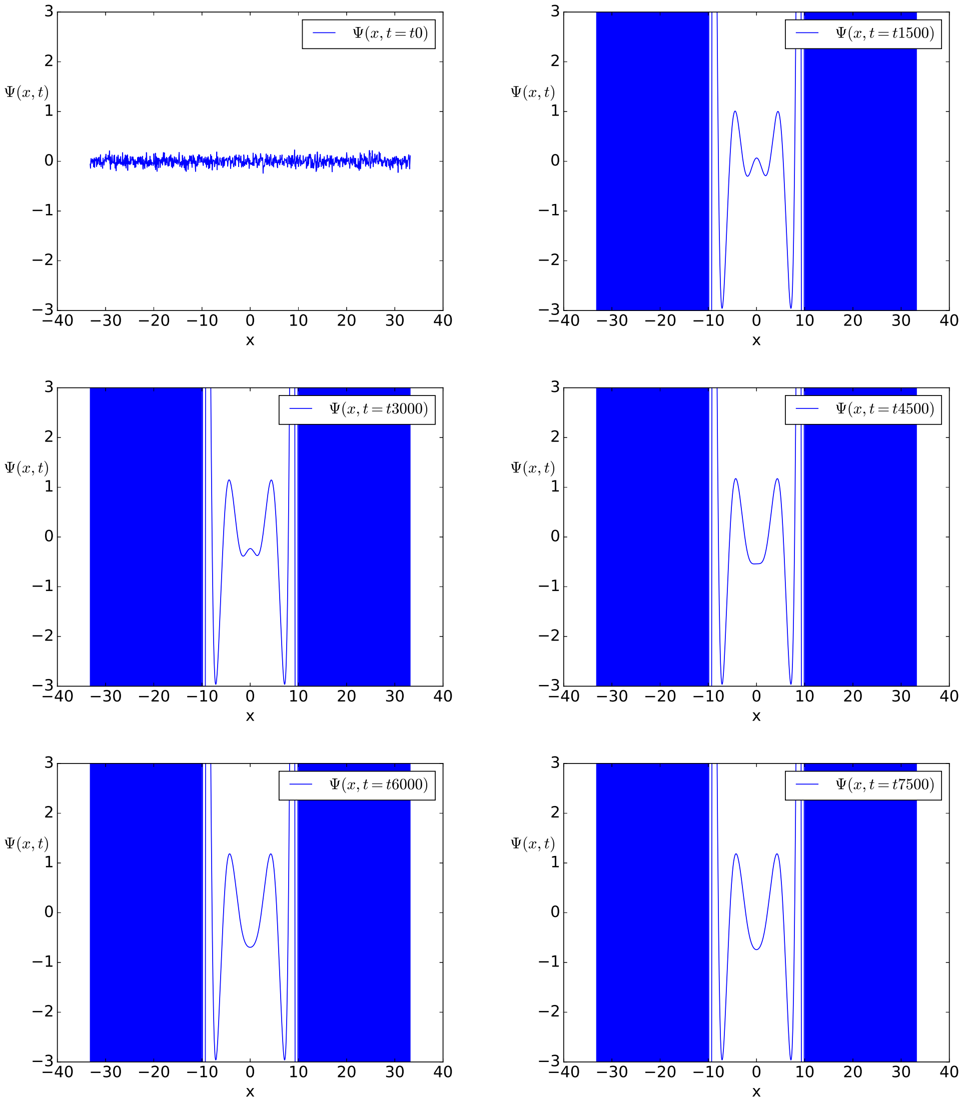

Figure 3.8: Solutions of the PMLSHE with $\theta_2 = \frac{\pi}{4}$.

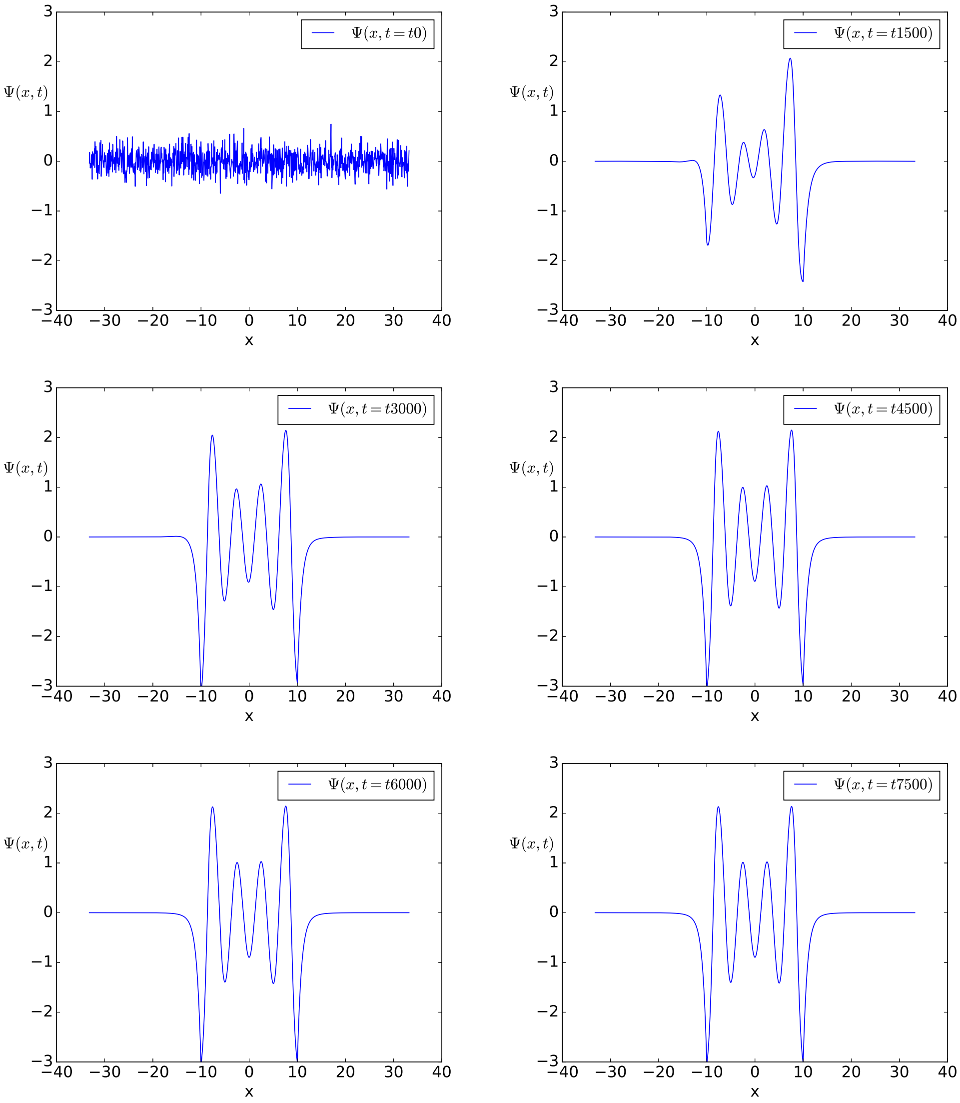

Figure 3.9: Solutions of the PMLSHE with $\theta_3 = \frac{\pi}{2}$.

The figures clearly illustrate that the numerical scheme do not result in the desired outcome for the PMLSHE (3.23) when $\theta > 0$, contrary to what we observed for the RSE. As previously mentioned, other boundary conditions may apply to the SHE, but a switch from $\Psi_x(\pm L, t) = 0$ to $\Psi_{xx}(\pm L, t) = 0$ results in such similar solutions, that we do not include them in the text.

4

Investigation and analysis

4.1 A qualitative comparison between the numerical results of the standard SHE and the PMLSHE

To qualitative discuss the behaviour of the solutions of $\Psi(x,t)$, we are to compare the PML solutions in figure 3.7 - 3.9 with the solution of the standard SHE $u(x,t)$ in figure 3.5. The behaviour of $\Psi(x,t)$ for different θ is discussed in the upcoming paragraph, while table 4.1 briefly states the overall nature of $\Psi(x,t)$ for large t.

θ	Ψ inside PML region: $\lvert x\rvert > 10$	Ψ outside PML region: $x \in (-10,10)$
$\theta_1 = \pi/8$	Distorted and barely damped.	No regular stripes.
$\theta_2 = \pi/4$	Extreme growth on grid scale	Two stripes.
$\theta_3 = \pi/2$	Totally damped	Uneven striped pattern

Table 4.1: The behaviour of $\Psi(x,t)$ for large t.

θ_1 does not result in a solution where $\Psi(x,t)$ goes to zero within the PML region. Actually, $\Psi(x, t)$ behaves diametrically opposite: stripes are not present outside the PML region, while they are partially represented on the inside. Note that the magnitude $|\Psi(x, t)|$ overall is larger than $|u(x, t)|$.

The result of θ_2 is way off inside the PML region, where $\Psi(x, t)$ seems to be grid levelled oscillations, with $|\Psi(x, t)| >> |u(x, t)|$. Outside the PML region some pattern evolution takes place, but $\Psi(x, t)$ contains fewer peaks than $u(x, t)$ within this domain.

θ_3 leads to a solution that is somewhat close to what we actually want, since $\Psi(x, t)$ is damped inside the PML region, while there is some evolution from white noise to stripes relative to $u(x, t)$ on the outside. However, the stripes located at the PML points seem to be influenced by a Gibbs-similar phenomenon, while the magnitude of $|\Psi(x, t)|$ matches $|u(x, t)|$ the remaining stripes outside the PML region.

Common for all simulations are the early evolution of unwanted spatiotemporal behaviour in contrast to our intention of a well functioning PML, and that the amplitude $|\Psi(x, t)|$ overall is larger than $|u(x, t)|$ for large t. A physical interpretation of this result is that the PML seems to put "extra energy" into the system.

The obtained solutions suggests that something is wrong somewhere in our overall setup, since every nonzero θ to some extent fails to produce the desired solution. Our task becomes to investigate the setup and try to establish exactly where the problems occur. We suggest that the answer hides behind one of the following three doors: either the contour based PML not applies to the SHE, or the MOL based PML scheme is numerically unstable as a consequence of the discretization. The third possibility might be implementation errors. Even though the differential operators contained in the SODM are shown to generate the correct derivatives for different θ, and all PML solutions $\Psi(x, t)$ are generated from the same code that produces the expected outcome for the standard SHE solution $u(x, t)$, we can not assume that the implementation is correct. Nor does it help that the PML scheme for the SHE follows the same design as the PML scheme for the rSE, where the PML did apply. At the end of the day, we can not rule out that the unwanted behaviour of $\Psi(x,t)$ for $\theta > 0$ originates from implementation errors.

4.2 Analysis of the linear numerical PMLSHE system

A natural way to start our investigation is by analysing the implemented numerical scheme, since it is the decisive cause for our presented solutions. We suspect that the implemented PMLSHE-system becomes additionally unstable relative to the the default instability of the SHE for $r > 0$, and we want to investigate the numerical scheme in the context of "additional instability". Therefore, the task becomes to determine whether or not the numerical scheme enforces more instability into the PML system, relative to the original system.

To do so, we need to preform a numerical linear stability analysis for the implemented PML scheme. We recall the MOL formulation of Ψ (3.30) such that the linear numerical system reads

$$\boldsymbol{\Psi}' = M(r,\theta)\boldsymbol{\Psi} \;, \tag{4.1}$$

where $M(r,\theta)$ denotes the SODM in (3.31) and (3.32). This system is well known from standard ODE theory, and a trial solution $\boldsymbol{\Psi} = e^{\lambda t}\boldsymbol{u}_0$ results in the eigenvalue problem

$$\lambda \boldsymbol{u}_0 = M(r,\theta)\boldsymbol{u}_0 \;, \tag{4.2}$$

with the corresponding solution

$$\boldsymbol{\Psi}(t) = \sum_l \alpha_l \boldsymbol{u}_l e^{\lambda_l t} \;, \tag{4.3}$$

under the assumption that $M(r,\theta)$ is diagonalizable. λ_l denotes the eigenvalues of the SODM, and are analogous to σ_k in the discrete Fourier solution (3.13) of the SHE. $\boldsymbol{u}_l$ express the corresponding eigenvectors of λ_l, and α_l

a	M_1	M_2	N_1	N_2	r	Δx_1	Δx_2	L
10	150	300	500	1000	0.5	$\frac{1}{15}$	$\frac{1}{30}$	100/3

Table 4.2: Constants used to generate the function $\lambda_*(\theta)$.

denotes the associated amplitude. The solution (4.3) is said to be unstable if one or more eigenvalues λ_l have a positive real part greater than zero, and we will denote the largest real eigenvalue by λ_*. Based on the observations in figure 3.7 to 3.9, where the nature of $\Psi(x,t)$ strongly varied with θ, we are to investigate how λ_* varies with θ.

Figure 4.1 and 4.2 illustrates the image of $\lambda_*(\theta)$ for two different Δx, where the constants in table 4.2 have been applied, and $\Delta x_1 > \Delta x_2$. Note that the λ_*-axis are logarithmically scaled.

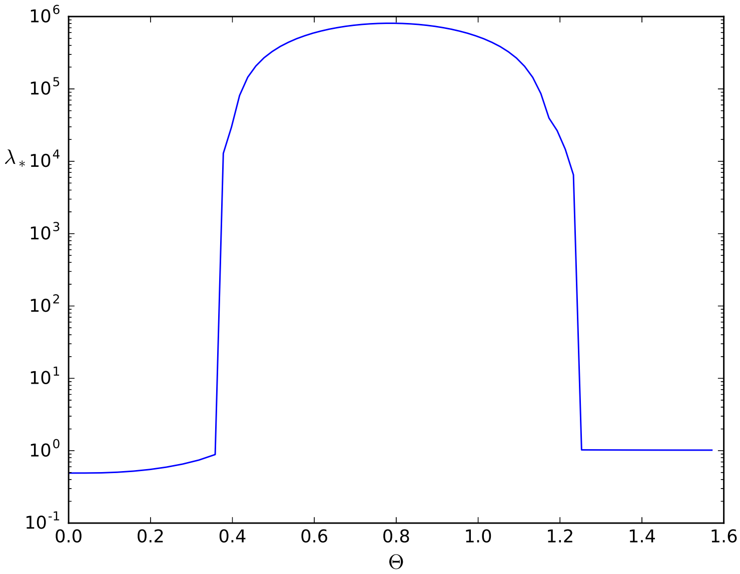

Figure 4.1: The max eigenvalue function $\lambda_*(\theta)$ with $\Delta x_1 = \frac{1}{15}$

As insinuated in the numerical solutions of $\Psi(x,t)$ in the previous section, the figures suggest that λ_* strongly varies with θ. As a first observation, we note

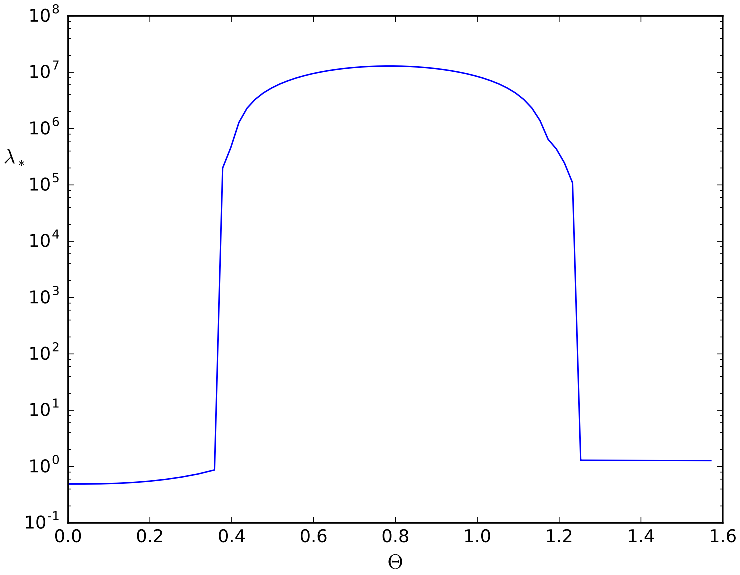

Figure 4.2: The max eigenvalue function $\lambda_*(\theta)$ with $\Delta x_2 = \frac{1}{30}$

that $\lambda_*(0) \approx r$ as it should, compared to the linear SHE. Furthermore, the behaviour of $\lambda_*(\theta)$ is the same in both figures: λ_* takes values of order 10^5 and larger when $\theta \in (0.39, 1.2)$, and is of order 10^0 in the remaining two θ-domains. We remark that the magnitude of λ_* for $\theta \in (0.39, 1.2)$ varies with the resolution, such that $|\lambda_*(\theta)|_{\Delta x_1} << |\lambda_*(\theta)|_{\Delta x_2}$.

This strange behaviour states that the numerical scheme has some unwanted behaviour built into the system, since "extra instability" seem to occur for all $\theta > 0$. However, we are not ready to take the images of $\lambda_*(\theta)$ as absolute truths just yet. Figure 4.1 and 4.2 of $\lambda_*(\theta)$ are created by the same implemented SODM used to generate the time varying solution $\Psi(x, t)$ in figure 3.7 to 3.9, and if the implementation is erroneous, we can not trust either result.

4.3 A comparisation between the SHE and the PMLSHE using an eigenvalue perturbation method

Based on the results in the previous sections, we are in need to analyse the implemented PMLSHE from another point of view. Since the numerical system allegedly changes nature for all θ, one alternative approach is to investigate how the PMLSHE behaves after a small change in θ. For simplicity of notation and manageable calculations, we choose to work with (3.28) as the governing equation for the PMLSHE in the imminent calculations.

To investigate the PMLSHE for small θ, we apply the first order Taylor expansions

$$e^{-2i\theta(x)} \approx 1 - 2i\theta(x) \tag{4.4a}$$

$$e^{-4i\theta(x)} \approx 1 - 4i\theta(x)\ , \tag{4.4b}$$

which inserted into (3.28) leads to the equation

$$\Psi_t = [\mathcal{U} + 4i\theta(x)\mathcal{V}]\Psi\ , \tag{4.5}$$

where the differential operators $\mathcal{U}$ and $\mathcal{V}$ reads

$$\mathcal{U} = r - (1 + \partial_{xx})^2 \tag{4.6a}$$

$$\mathcal{V} = \partial_{xx}(1 + \partial_{xx})\ . \tag{4.6b}$$

If we assume a separable solution $\Psi = \psi(x)e^{\sigma t}$, (4.5) turns into

$$\sigma\psi = [\mathcal{U} + 4i\theta(x)\mathcal{V}]\psi\ , \tag{4.7}$$

as an equation for the spatial part of Ψ, analogous to the implemented MOL discretization for small θ. The structure of (4.7) states that the spatial part of the PMLSHE can be read as a perturbation problem where $\theta(x)$ acts as the perturbation parameter, since $\theta(x)$ is constant in each θ-domain relative to the PMLSHE formulation (3.23). In that manner, the equation

$$\sigma\psi = \mathcal{U}\psi \tag{4.8}$$

specify the unperturbed problem with the corresponding solution $\psi = e^{ikx}$, while (4.7) defines the perturbed problem.

Since our objective is to investigate how the PMLSHE (3.23) behaves on a finite domain, we define the unperturbed problem (4.8) as the standard SHE on a finite domain, such that the boundary conditions are periodic. With the derived relations, our objective becomes to establish a PML correction for a small θ to the finite SHE.

We then turn towards the mathematical toolbox and take out the apparatus of perturbation theory, which is the only game in town for analysing small variations around a known state of a mathematical formulation of a physical system.

Since the forthcoming analysis concerns finite L, the wavenumbers are discrete and given as

$$k_j = \frac{\pi}{L} j \,, \tag{4.9}$$

where j is an integer. The corresponding for k_j eigenfunction is given by

$$\psi_j = e^{ik_j x} \,, \tag{4.10}$$

and the associated growth rate reads

$$\sigma_j = r - (1 - k_j^2)^2 \,. \tag{4.11}$$

The calculations within the field of perturbation theory are by nature tedious, and we do not include all details in the forthcoming paragraphs. We write the required relations, and present the main arguments by words to substantiate our results.

Since we are to establish corrections to the growth rate σ_j, and its corresponding wavenubmer k_j for any integer j, we need to establish a consistent notation. By denoting ψ_j(4.10) as ψ_0^j, and σ_j (4.11) as σ_0^j for a integer $j \in \mathbb{Z}$, we suggest the perturbation relations

$$\sigma^j = \sigma_0^j + \epsilon\sigma_1^j + \epsilon^2\sigma_2^j \,, \tag{4.12}$$

$$\psi^j = \psi_0^j + \epsilon\psi_1^j + \epsilon^2\psi_2^j \, , \tag{4.13}$$

witch inserted into (4.7) results in the perturbation hierarchy

- ϵ^0:

$$\sigma_0^j\psi_0^j = \mathcal{U}\psi_0^j \, , \tag{4.14}$$

- ϵ^1:

$$(\mathcal{U} - \sigma_0^j)\psi_1^j = \sigma_1^j\psi_0^j - 4i\theta(x)\mathcal{V}\psi_0^j \, , \tag{4.15}$$

- ϵ^2:

$$(\mathcal{U} - \sigma_0^j)\psi_2^j = \sigma_1^j\psi_1^j + \sigma_2^j\psi_0^j - 4i\theta(x)\mathcal{V}\psi_1^j \, . \tag{4.16}$$

We are now to determine σ_1^j and σ_2^j as the first and second order correction to σ_0^j (4.11), and to manage this, we will discuss each order of ϵ separately. Our most trusted tools in the imminent calculations is the inner product

$$\langle f(x), g(x)\rangle = \int_{-L}^{L} \mathrm{d}x \; f(x)\overline{g(x)} \, , \tag{4.17}$$

and standard results from linear algebra on a functional space. Particularly the theory concerning orthogonality of eigenfunctions, with the corresponding Kronecker Delta as a result of the inner product between different and equal eigenfunctions, and eigenfunction expansion of a vector in the functional space.

ϵ^0 :

Equation (4.14) describes is the initial problem and is thereby solved by (4.11).

ϵ^1 :

The inner product between (4.15) and ψ_0^j described in (4.18)

$$\langle\ (\mathcal{U}-\sigma_0^j)\psi_1^j,\ \psi_0^j\ \rangle = \langle \sigma_1^j\psi_0^j - 4i\theta(x)\mathcal{V}\psi_0^j,\ \psi_0^j\ \rangle \tag{4.18}$$

where ψ_1^j is expressed by the expansion

$$\psi_1^j = \sum_{n\neq j} b_n\psi_0^n\ , \tag{4.19}$$

results in the relation

$$\sigma_1^j = 4i\frac{\langle\theta(x)\mathcal{V}\psi_0^j,\ \psi_0^j\rangle}{\langle\psi_0^j,\ \psi_0^j\rangle} \tag{4.20}$$

for the first order correction σ_1^j. To substantiate this result we remark that the left hand side of (4.18) is zero since to the inner product $\langle\ \psi_0^j,\ \psi_0^n\rangle$, which emerges after inserting the expansion (4.19), is zero $\forall\ n\neq j$. The right hand side is thereby zero, and standard inner product rules results in the presented formula for σ_1^j. Equation (4.20) states that σ_1^j is strictly imaginary, and it is therefore of no use to us, since we are interested in the real valued corrections to the growth rate σ_0^j. According to (4.16) we must establish an exact expression for ψ_1^j, in order to determine the next correction σ_2^j. Hence, we are to determine the constants b_n in (4.19). To find those constants we expand the right hand side of (4.15) by

$$\sum_{n\neq j} c_n\psi_0^n = \sigma_1^j\psi_0^j - 4i\theta(x)\mathcal{V}\psi_0^j\ , \tag{4.21}$$

where the inner product between (4.21) and ψ_0^m

$$\langle\ \sum_{n\neq j} c_n\psi_0^n,\ \psi_0^m\ \rangle = \langle\ \sigma_1^j\psi_0^j - 4i\theta(x)\mathcal{V}\psi_0^j,\ \psi_0^m\ \rangle\ , \tag{4.22}$$

results in the relation

$$c_m = -\frac{2i}{L}\langle\ \theta(x)\mathcal{V}\psi_0^j,\ \psi_0^m\ \rangle\ . \tag{4.23}$$

This follows since the left hand side of (4.22) is 0 for all $n\neq m$, and 1 for $n=m$, which explains the constant c_m in (4.23). The right hand side of (4.22) contains two inner products, of which one is zero by the same argument as in the previous paragraph, and the other is given by c_m in (4.23).

Inserting (4.19) and (4.21) into (4.15), together with the relation

$$\mathcal{U} \sum_{n \neq j} b_n \psi_0^n = \sum_{n \neq j} b_n \sigma_0^n \psi_0^n, \tag{4.24}$$

as argued by (4.14), leads to the equation

$$\sum_{n \neq j} b_n (\sigma_0^n - \sigma_0^j) \psi_0^n = \sum_{n \neq j} c_n \psi_0^n \ . \tag{4.25}$$

Equation (4.25) is true by comparison if the relation

$$b_n = \frac{c_n}{\sigma_0^n - \sigma_0^j} \tag{4.26}$$

holds, and since c_n in (4.26) is given by c_m in (4.23), we obtain the equation

$$b_n = -\frac{2i}{L(\sigma_0^n - \sigma_0^j)} \langle\ \theta(x) \mathcal{V} \psi_0^j,\ \psi_0^n\ \rangle\ . \tag{4.27}$$

for the constants b_n. This expression contains only known mathematical objects, which allows us to step up the game and carry out the last correction σ_2^j.

ϵ^2 :

Redoing the inner product calculations from (4.18) on the second order perturbation equation (4.16) with a eigenfunction ψ_0^j, where ψ_2^j is expressed by an expansion like ψ_1^j in (4.19), the second order correction σ_2^j reads

$$\sigma_2^j = \frac{2i}{L} \langle\ \theta(x) \mathcal{V} \psi_1^j,\ \psi_0^j\ \rangle\ \ . \tag{4.28}$$

Substituting ψ_1^j in (4.28) with the expansion (4.19), and the corresponding b_n in (4.27), results in the relation

$$\sigma_2^j = \frac{4}{L^2} \sum_{n \neq j} \frac{1}{\sigma_0^n - \sigma_0^j} \langle\ \theta(x) \mathcal{V} \psi_0^j,\ \psi_0^n\ \rangle\ \langle\ \theta(x) \mathcal{V} \psi_0^n,\ \psi_0^j\ \rangle\ \ , \tag{4.29}$$

which contains only known mathematical objects. To proceed with (4.29), we need to establish what the factor $\mathcal{V}\psi_0^m$ in the inner products describes. Applying an eigenfunction ψ_0^m, leads to the relation

$$\begin{aligned}\mathcal{V}\psi_0^m &= \partial_{xx}(1+\partial_{xx})e^{ik_m x} && \text{(4.30a)}\\ &= k_m^2(k_m^2-1)\psi_0^m && \text{(4.30b)}\\ &= \alpha_m\psi_0^m\ , && \text{(4.30c)}\end{aligned}$$

where α_m reads

$$\alpha_m = k_m^2(k_m^2-1)\ . \tag{4.31}$$

With this, the growth rate (4.29) takes the simple form

$$\sigma_2^j = \frac{4}{L^2}\sum_{n\neq j}\frac{\alpha_n\alpha_j}{\sigma_0^n-\sigma_0^j}\langle\ \theta(x)\psi_0^j,\ \psi_0^n\ \rangle\ \langle\ \theta(x)\psi_0^n,\ \psi_0^j\ \rangle\ , \tag{4.32}$$

where the inner products in (4.32) are given as

$$\begin{aligned}\langle\ \theta(x)\psi_0^j,\ \psi_0^n\ \rangle\ &= \theta_N\left[\frac{i}{k_j-k_n}e^{ix(k_j-k_n)}\right]_{-L}^{-a} + \theta_P\left[\frac{i}{k_j-k_n}e^{ix(k_j-k_n)}\right]_{a}^{L} && \text{(4.33a)}\\ \langle\ \theta(x)\psi_0^n,\ \psi_0^j\ \rangle\ &= \theta_N\left[\frac{i}{k_n-k_j}e^{ix(k_n-k_j)}\right]_{-L}^{-a} + \theta_P\left[\frac{i}{k_n-k_j}e^{ix(k_n-k_j)}\right]_{a}^{L}\ , && \text{(4.33b)}\end{aligned}$$

if we recall the definition of $\theta(x)$ (3.26).

Since the relations α_m (4.31), σ_m(4.11), and the stated inner products (4.33) all are given by k_j and the fixed constants $\{L, a, \theta_N, \theta_P, r\}$, equation (4.32) represents a function $\sigma_2^j(k_j)$ over the discrete set of wavenumbers k_j, and is possible to calculate numerically from a suitable list of integers j. By taking use of the same parameter regime for $\{M, N, a, r, L\}$[1] as applied to the numeric solutions $\Psi(x,t)$ in figure 3.5 to 3.9, the growth rate correction $\sigma_0 + \sigma_2$ is analogous to the eigenvalues λ_l in (4.3) for the numeric PML scheme for small θ.

---

[1] Note that L is given by the relation $L = \frac{N}{M}a$ from the discretization (2.67).

a	M	N	j_{low}	j_{high}	θ_P	θ_N	r	L
10	150	500	−55	55	$\pi/30$	$\pi/30$	0.5	$100/3$

Table 4.3: Parameters to the PML correction σ_2^j.

We are with this numeric perturbation able to produce a PML correction $\sigma_0 + \sigma_2$ very similar to our numerics, and plot it against the growth rate σ_0 for the standard SHE on a finite domain. Applying the constants in table 4.3 results in the image depicted in figure 4.3 for the functions

$$f_1(k_j) = \sigma_0^j(k_j) \tag{4.34a}$$
$$f_2(k_j) = \sigma_0^j(k_j) + \sigma_2^j(k_j) \; . \tag{4.34b}$$

As the figure illustrates, the growth rate of the PML correction matches

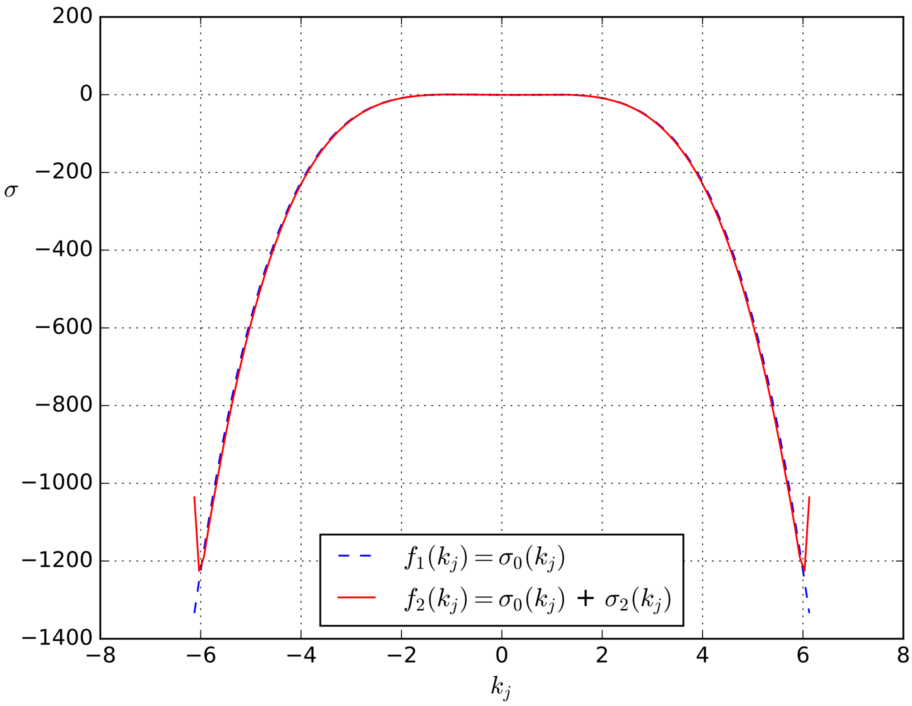

Figure 4.3: The standard SHE growth rate σ_0 on a finite domain plotted against its second order PML correction σ_2.

the standard SHE, but changes nature completely at a specific wavenumber and grows in the opposite direction. However, since the correction σ_2 is a asymptotic PML correction to σ_0 for small θ, we are not in position to make any decisive conclusions concerning the PMLSHE just yet. The growth caused by σ_2 might flatten out and never become positive which not would affect the PMLSHE. Alternatively, it may grow out of bounds and influence its solutions extensively.

Based on the presented results for the PML correction to the SHE, we are led to suspect that the numerical results of $\Psi(x, t)$ and $\lambda_*(\theta)$ in the previous sections not are a consequence of implementation errors, but rather a built in feature of the PMLSHE. To investigate this further, we turn to the original formulation of the PMLSHE with the intention to carry out analytical calculations.

4.4 Stability analysis of a PMLSHE similar equation

Based on the results in the two previous sections, we will consider the option that a PML transformation of the SHE imposes an unforeseen nature of the PMLSHE. To determine whether the PML actually produces the desired outcome for the SHE, we are to perform a stability analysis of the PMLSHE (3.23). We will as in the previous section work with (3.28) as the governing equation for the PMLSHE to keep the number of calculations at a manageable minimum.

The base solution $\Psi_b = 0$ also applies to (3.28), which in turn leads to the linear PMLSHE

$$\Psi_t = [r - (1 + e^{-2i\theta(x)}\partial_{xx})^2]\Psi \ . \tag{4.35}$$

However, normal modes on the form $e^{ikx}e^{\sigma t}$ does not solve for Ψ in (4.35), since it leads to the relation

$$\sigma = r - (1 - e^{-2i\theta(x)}k^2)^2 \ , \tag{4.36}$$

which physically makes little sense: the growth rate can not be a function of the spatial variable x. We must therefore modify our equation into something solvable, but at the same time, partially analogous to the original PMLSHE.

Since the stepfunction $\theta(x)$ is the undisputed cause for the futile relation (4.36), we redefine $\theta(x)$ to be constant over the whole spatial domain by $\theta(x) = \theta \ \forall x$ where $\theta \in (0, \pi/2)$, as a somewhat naive, but seemingly relevant simplification. Furthermore we assume that the domain length L of the PMLSHE is infinitely large, such that the function $\Psi(x, t)$ can be expressed by a integral solution analogous to the Fourier transform (3.14). As previously mentioned, both formulations (3.28) and (3.23) of the PMLSHE are equivalent statements under these conditions.

With the stated assumptions, a small perturbation $\Psi \longrightarrow \Psi + \Psi_b$ around $\Psi_b = 0$ for the linear PMLSHE (4.35) results in the linear constant PML equation

$$\Psi_t = [r - (1 + e^{-2i\theta}\partial_{xx})^2]\Psi \ , \tag{4.37}$$

which we from now on will refer to as the CPMLSHE.

Even though (4.37) not is equivalent to (4.35) as a variant of the linear PMLSHE, or our numerical scheme, we have to assume that the nature and behaviour of (4.37) resembles those systems in some way. Equation (3.28) describes with the stated modification an evolution equation on a infinite domain that can be said to be "covered by a constant PML"[2], whereby the stability analysis of this system might give us advantageous insight.

Inserting a Fourier mode (3.12) into (4.37) results in the growth rate equation

$$\sigma = r - (1 - 2k^2 e^{-2i\theta} + k^4 e^{-4i\theta}) \ , \tag{4.38}$$

with the control parameters θ and r. Note that the right hand side of (4.38) is complex, which imply that σ is complex and on the form $\sigma = \sigma_R + i\sigma_I$.

---

[2] A physical interpretation of a constant PML: think of the SHE as an equation describing the flow of a fluid with a specific viscosity, and that the PML is a noticeable change in viscosity.

As discussed in the linear stability analysis of the standard SHE, we are to investigate the real part of the growth rate as a function over the different wavenumbers. Applying a variant of Eulers identity

$$e^{iax} = \cos(ax) + i\sin(ax)\ , \qquad \text{for } a \in \mathbb{R}\ , \tag{4.39}$$

to (4.38) results in the equation

$$\sigma_R(k) = r - 1 + 2k^2\cos(2\theta) - k^4\cos(4\theta)\ , \tag{4.40}$$

for the real part of the growth rate. Our task is to determine under which parameter conditions the growth changes sign for all possible wave numbers.

As a first observation we remark that if $k \to \infty$, the $-k^4\cos(4\theta)$ term dominates the growth rate, such that the relation

$$\sigma_R(k) \approx -k^4\cos(4\theta) \tag{4.41}$$

holds for large k. Figure 4.4 which imply that $\cos(4\theta) < 0$ for $\theta \in (\frac{\pi}{8}, \frac{3\pi}{8})$, we conclude that the growth rate $\sigma_R(k)$ is both positive and describes an unbounded monotonically increasing function for those θ. This result is fundamentally problematic, because it implies an ill posed problem, where (4.37)

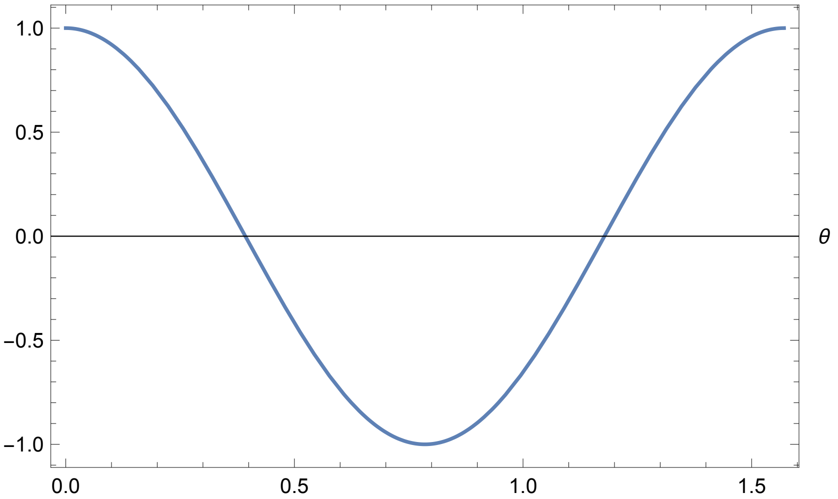

Figure 4.4: $\cos(4\theta)$ for $\theta \in [0, \frac{\pi}{2}]$

no longer describes a physical system. A proof to support this allegation is presented in appendix B.

The zeros of $\cos(4\theta)$ are given by $\theta_{Z_1} = \frac{\pi}{8}$ and $\theta_{Z_2} = \frac{3\pi}{8}$, which in turn controls the sign of the $2k^2\cos(2\theta)$ term in (4.40). Since $\cos(2\theta) > 0$ and $\cos(2\theta) < 0$ for θ_{Z_1} and θ_{Z_2} respectively, it follows that $\sigma_R(k)$ is monotonically increasing for θ_{Z_1}, and monotonically decreasing for θ_{Z_2}. To summarize, the valid PML angles for the CPMLSHE (4.37) are given by the set $S_I \cup S_{II}$ where

$$S_I = (0, \tfrac{\pi}{8}) \tag{4.42a}$$

$$S_{II} = [\tfrac{3\pi}{8}, \tfrac{\pi}{2}]\ , \tag{4.42b}$$

since $\sigma_R(k)$ defines a monotonically decreasing function for the valid θ.

Now we are to determine how $\sigma_R(k)$ changes for valid PML angles. We begin by examining the derivative of $\sigma_R(k)$

$$\sigma_R'(k) = 4k(\cos(2\theta) - k^2\cos(4\theta))\ , \tag{4.43}$$

with the corresponding zeros

$$k = 0 \tag{4.44a}$$

$$k^2 = \frac{\cos(2\theta)}{\cos(4\theta)}\ . \tag{4.44b}$$

The left hand side of the (4.44b) is always positive, and as figure 4.5 illustrates, the graph of $V(\theta) = \frac{\cos(2\theta)}{\cos(4\theta)}$ states that

$$V(\theta) > 0 \text{ if } \theta \in S_I \tag{4.45a}$$

$$V(\theta) < 0 \text{ for } \theta \in S_{II}. \tag{4.45b}$$

Hence, $\sigma_R(k)$ has three possible extremal points given by the wavenumbers

$$k_0 = 0\ , \qquad k_+ = \sqrt{\frac{\cos(2\theta)}{\cos(4\theta)}}\ , \qquad k_- = -\sqrt{\frac{\cos(2\theta)}{\cos(4\theta)}}\ , \tag{4.46}$$

where all three of them realizes if $\theta \in S_I$, while only k_0 occurs when $\theta \in S_{II}$.

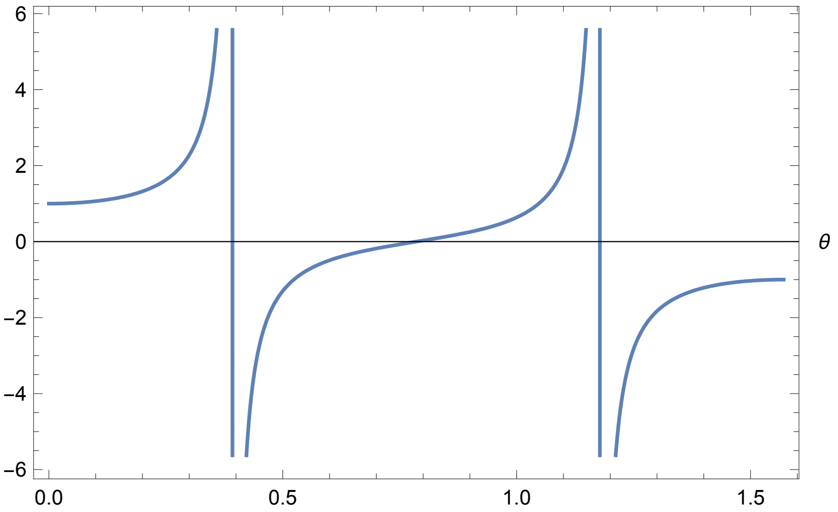

Figure 4.5: $V(\theta) = \frac{\cos(2\theta)}{\cos(4\theta)}$ for $\theta \in [0, \frac{\pi}{2}]$

Since we have established the zeros $\sigma_R(k)$, and its monotonically decreasing nature for feasible θ, the image and critical wavenumbers of $\sigma_R(k)$ are implicitly given:

- If $\theta \in S_I$, the shape of the growth rate curve is as illustrated in subfigure 4.6a, whereby the global maxima occurs at the critical wavenumbers $k_c = k_\pm$.
- If $\theta \in S_{II}$, the shape of the growth rate curve is as illustrated in subfigure 4.6b, and the global maxima occurs at the critical wavenumber $k_c = k_0$.

From the the wavenumber-wavelenght relation

$$\xi = \frac{2\pi}{k}\,, \tag{4.47}$$

where ξ denotes the wavelenght, we remark that the already assumed infinite domain of x is a necessary criteria if $\theta \in S_{II}$ are to be valid PML angles. This follows as a consequence of the critical wavenumber $k_0 = 0$ that arises for $\sigma_R(k)$ when $\theta \in S_{II}$, as depicted in figure 4.6b.

Now we have reached the final step of this analysis, namely to decide how the maximal value of $\sigma_R(k)$ depends on the control parameter r. Since we

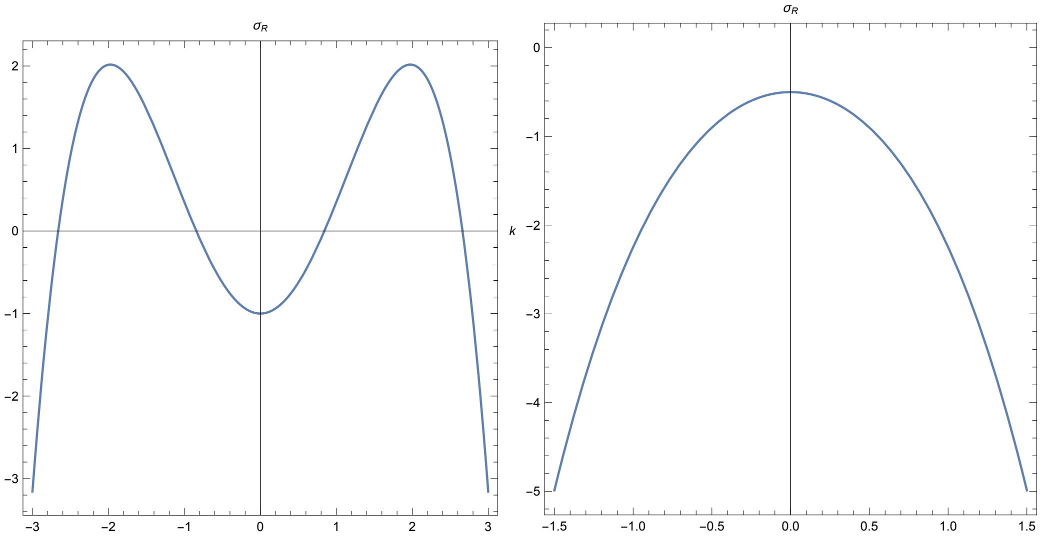

(a) Image of $\sigma_R(k)$ if $\theta \in S_I$.

(b) Image of $\sigma_R(k)$ if $\theta \in S_{II}$.

Figure 4.6: The growth rate curve $\sigma_R(k)$ for valid PML angles.

have established the nature of $\sigma_R(k)$, the r-dependency is straight forward to determine from the critical wave numbers. Inserting (4.46) into $\sigma_R(k)$ (4.40) results in the following formulas

- If $\theta \in S_I$:

  $$\max_k \sigma_R(k) = r - 1 + \frac{\cos^2(2\theta)}{\cos(4\theta)} \; . \tag{4.48}$$

  By letting $\max_k \sigma_R(k) = 0$ in (4.48) we obtain the function

  $$r_1(\theta) = \frac{\cos^2(2\theta)}{\cos(4\theta)} - 1 \tag{4.49}$$

  which is depicted in figure 4.7. As the figure illustrates, the critical value r_c of the CPMLSHE is smaller than zero for all $\theta \in S_I$.

- If $\theta \in S_{II}$

  $$\max_k \sigma_R(k) = r - 1 \; , \tag{4.50}$$

  which results in the function

  $$r_2(\theta) = 1 \; . \tag{4.51}$$

Hence, the critical parameter of the CPMLSHE for $\theta \in S_2$ is given by $r_c = 1$ for all angles, which is illustrated in figure 4.7.

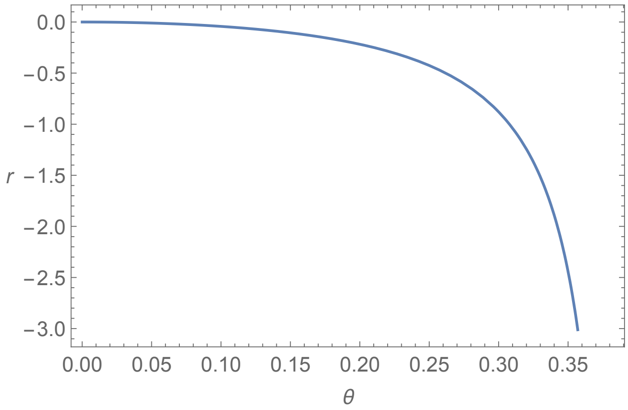

(a) $r_1(\theta)$ for $\theta \in (0, \frac{\pi}{8})$ of the CPMLSHE.

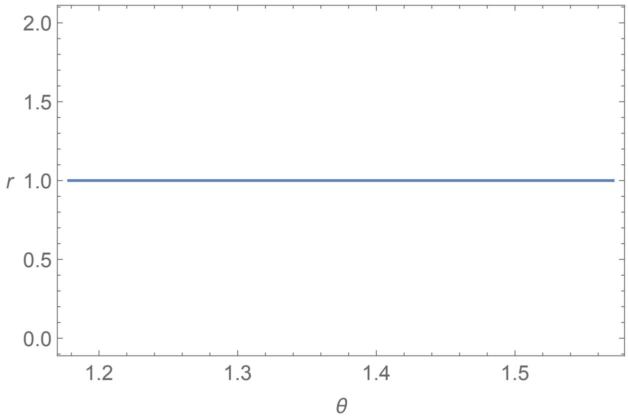

(b) $r_2(\theta)$ for $\theta \in (\frac{3\pi}{8}, \frac{\pi}{2})$ of the CPMLSHE.

Figure 4.7: $r_c(\theta)$ for valid PML angles $S_I \cup S_{II}$.

In summary, the PML applies to the CPMLSHE on a infinite domain for the two valid ranges of $S_I \cup S_{II}$ stated in (4.42). Both the growth rate, and the critical parameter r_c depends on θ such that r_c is a varying function of θ for $\theta \in S_I$ where $r_c < 0 \; \forall \; \theta$, while $r_c = 1$ for all $\theta \in S_{II}$.

The goal for this section were to consider the option of a ill posed nature for PMLSHE, which resulted in the presented CPMLSHE analysis. The obtained results indicates that well posedness of the PMLSHE depends on θ, but since the presented CPMLSHE analysis assumed a infinite domain, we are to analyse the CPMLSHE on a finite domain to approximate the finite PMLSHE even better.

4.5 The CPMLSHE on a finite domain

In this section we will analyse the CPMLSHE on a finite domain, and the objective is to derive an analytic solution where the boundary conditions $u(x,t) = 0$ and $u_{xx}(x,t) = 0$ are enforced. Furthermore, we will compare the analytic solution with a numerical solution based on the scheme we applied to the PMLSHE, only with a constant PML enforced. However, we will not investigate the solutions in terms of spatiotemporal dynamics, but through comparison of analogous corresponding spatial modes, when the system is on the onset of pattern formation.

We will also investigate how the critical parameter r_c varies with θ both analytically and numerically, and we will assume that the feasible PML angles from the previous section applies in the finite case, since we are of no reason to believe otherwise.

As we will see, the analytical solution must be determined by a case study, and to sustain readability we present a general overview of the numerical and analytical solution process, while we present both analytical and numerical solutions for each case separately.

4.5.1 Analytical analysis

The CPMLSHE with the assumed boundary conditions reads

$$\Psi_t = [r - (1 + e^{-2i\theta}\partial_{xx})^2]\Psi \tag{4.52a}$$

$$\Psi(\pm L, t) = 0 \tag{4.52b}$$

$$\Psi_x(\pm L, t) = 0\ , \tag{4.52c}$$

whereby a test solution $\Psi = \phi(x)e^{\sigma t}$ leads to the eigenvalue problem

$$(r - \sigma)\phi = (1 + e^{-2i\theta}\partial_{xx})^2\phi \tag{4.53a}$$

$$\phi(\pm L) = 0 \tag{4.53b}$$

$$\phi_x(\pm L) = 0\ , \tag{4.53c}$$

for the spatial part of the CPMLSHE. Based on the results from the previous section, we assume that the growth rate is complex and on the form $\sigma = \sigma_R + i\sigma_I$.

However, we let $\sigma_R = 0$ in the forthcoming calculations since the objective is to determine the critical parameter function $r_c(\theta)$, and analyse the system on the onset of pattern formation.

Since the constant on the left hand side of (4.53) varies with θ, we need to solve (4.53) by preforming a case study, where the expression $(r - \sigma) = r - i\sigma_I$ dictates the different cases. Since both r and σ_I are real numbers, there are only two cases.

1. Case I: $r - i\sigma_I$ is a possible complex number for real r and σ_I, where at most one can be zero
2. Case II: $r = \sigma = 0$

To solve the eigenproblem (4.53) we apply the eigenfunction

$$\phi_{k_n}(x) = e^{ik_n x}\ , \tag{4.54}$$

which for each case of r and σ_I results in a criteria equation with n solutions for the wavenumbers $k = k_n$. With those k_n we are able to establish a basis solution to the eigenproblem by the linear combination

$$\phi(x) = \sum_n a_n e^{ik_n x} \,, \tag{4.55}$$

which we will use to satisfy the boundary conditions and determine analytical critical parameter function $r_c^A(\theta)$.

4.5.2 Numerical analysis

To generate the numerical critical parameter function $r_c^N(\theta)$ and the spatial mode analogous to (4.55) from the numerical scheme, we recall the ODE system formulation (4.1) - (4.3), with the corresponding notation for the eigenvalues λ_l, eigenvectors $\boldsymbol{u}_l$ and maximal eigenvalue λ_* of a operator matrix.

For the finite CPMLSHE (4.52) we define the constant PML operator matrix

$$C(r,\theta) = (r-1)I_d - [2e^{-2i\theta}\mathcal{D}_2(0) + e^{-4i\theta}\mathcal{D}_4(0)] \,, \tag{4.56}$$

as a modified version of the PML SODM $M(r,\theta)$ (3.32). $\mathcal{D}_2(0)$ and $\mathcal{D}_4(0)$ represents the standard spatial second and fourth order derivative on a finite domain, and I_d denotes the identity matrix.

For a fixed θ_F we define the function

$$f(r) = \max_{\lambda_l} C(r,\theta_F) \tag{4.57a}$$

$$= \lambda_*[C(r,\theta_F)] \,, \tag{4.57b}$$

and establish the root finding problem

$$f(r) = 0 \tag{4.58a}$$

$$r \in (a,b) \tag{4.58b}$$

$$f(a) < 0 < f(b) \,. \tag{4.58c}$$

The solution of (4.58) determines r_c for the fixed θ_F, and is easily solved by a built in numerical root finder routine. For a suitable θ-grid of the valid PML angles we are therefore able to numerically determine the function $r_c^N(\theta)$.

For corresponding values of θ and r, the spatial mode analogous to the solution $\phi(x)$ (4.55) is given by the eigenvector $\boldsymbol{u}_l$ of $C(r,\theta)$ that corresponds to the eigenvalue $\lambda_l = \lambda_R + i\lambda_I$ where $\lambda_R \approx 0$. We denote this eigenvector $\boldsymbol{u}_*$.

4.5.3 Case I: Analytical analysis

Inserting (4.54) into (4.53) results in the criteria equation

$$(1 - k^2 e^{-2i\theta})^2 = r - i\sigma_I \, , \tag{4.59}$$

where the solutions of (4.59) are given by the expressions

$$\begin{aligned}
k_1 &= e^{i\theta}(1 + \sqrt{r - i\sigma_I})^{1/2} && (4.60a)\\
k_2 &= e^{i\theta}(1 - \sqrt{r - i\sigma_I})^{1/2} && (4.60b)\\
k_3 &= -e^{i\theta}(1 + \sqrt{r - i\sigma_I})^{1/2} && (4.60c)\\
k_4 &= -e^{i\theta}(1 - \sqrt{r - i\sigma_I})^{1/2} \, . && (4.60d)
\end{aligned}$$

The corresponding linear combination which determines the solution space of $\phi(x)$ reads

$$\phi(x) = A\phi_{k_1}(x) + B\phi_{k_2}(x) + C\phi_{k_3}(x) + D\phi_{k_4}(x) \, , \tag{4.61}$$

and we will use (4.61) to satisfy the boundary conditions by establishing a nontrivial solution to the matrix system

$$\begin{bmatrix} \phi_{k_1}(-L) & \phi_{k_2}(-L) & \phi_{k_3}(-L) & \phi_{k_4}(-L) \\ \phi_{k_1}(L) & \phi_{k_2}(L) & \phi_{k_3}(L) & \phi_{k_4}(L) \\ \phi'_{k_1}(-L) & \phi'_{k_2}(-L) & \phi'_{k_3}(-L) & \phi'_{k_4}(-L) \\ \phi'_{k_1}(L) & \phi'_{k_2}(L) & \phi'_{k_3}(L) & \phi'_{k_4}(L) \end{bmatrix} \begin{bmatrix} A \\ B \\ C \\ D \end{bmatrix} = \begin{bmatrix} 0 \\ 0 \\ 0 \\ 0 \end{bmatrix} \, . \tag{4.62}$$

Our task is therefore to establish under which conditions the determinant of the matrix in (4.62) is zero for fixed L. We denote the matrix M_I, which takes the form of (4.63) after inserting the corresponding basis vectors and constants.

$$M_I = \begin{bmatrix} e^{-ik_1L} & e^{-ik_2L} & e^{-ik_3L} & e^{-ik_4L} \\ e^{ik_1L} & e^{ik_2L} & e^{ik_3L} & e^{ik_4L} \\ ie^{-ik_1L}k_1 & ie^{-ik_2L}k_2 & ie^{-ik_3L}k_3 & ie^{-ik_4L}k_4 \\ ie^{ik_1L}k_1 & ie^{ik_2L}k_2 & ie^{ik_3L}k_3 & ie^{ik_4L}k_4 \end{bmatrix} \tag{4.63}$$

Conceptually the determinant $|M_I|$ reads

$$|M_I| = f(k_1, k_2, k_3, k_4) \cdot g(k_1, k_2, k_3, k_4) \ , \tag{4.64}$$

where the factors f and g are to large to include in the text. Since k_n is defined as a relation $k_n(\theta, r, \sigma_I)$, the governing determinant equation reads

$$f(\theta, r, \sigma_I) \cdot g(\theta, r, \sigma_I) = 0 \ , \tag{4.65}$$

where the factor $f(\theta, r, \sigma_I)$ is on the form $e^{h(\theta,r,\sigma_I)}$, and non zero by definition.

Hence, the boundary conditions are satisfied for combinations of $\{r, \theta, \sigma_I\}$ which fulfils the equation

$$g(\theta, r, \sigma_I) = 0 \ , \tag{4.66}$$

and since g is a complex function $g = g_R + ig_I$, (4.66) transforms into the system of equations

$$g_R(\theta, r, \sigma_I) = 0 \tag{4.67a}$$

$$g_I(\theta, r, \sigma_I) = 0 \ . \tag{4.67b}$$

The symbolic expressions of g_R and g_I are to our knowledge unmanageable, and we will therefore solve (4.67) numerically for fixed θ. In that manner, (4.67) describes a system of two equations with two unknowns, which we can solve to determine $r(\theta)$ by a numerical iteration process like the Newton Method from a initial guess $\gamma_0 = (r^*, \sigma_I^*)$. However, both g_R and g_I are highly nonlinear expressions of trigonometric functions, which imply multiple solutions of (4.67). The problem is therefore to determine a useful initial guess g_0, such that the iterated solution corresponds to the lowest r-value at the onset of pattern formation. Taking use of a symbolic mathematical software with numerical support[3], we are able to plot the contour lines of (4.67), and from the plot determine a initial guess g_0.

As an example we present the contour plot depicted in figure 4.8 for $\theta = \frac{15\pi}{32}$, and the previously applied domain length $L = 100/3$. A solution of (4.67) is given where the different coloured lines intersect, and as the figure illustrates, the smallest zero occurs around $\gamma_0 = (1, 0)$. Using γ_0 as the initial guess results in the exact solution $r = 1.00755$ and $\sigma_I = -0.000925538$, which states that $r_c^A(\frac{15\pi}{32}) = 1.00755$. For a suitable θ-grid we are to repeat this process for the valid PML angles, which will result in the numerically calculated analytic

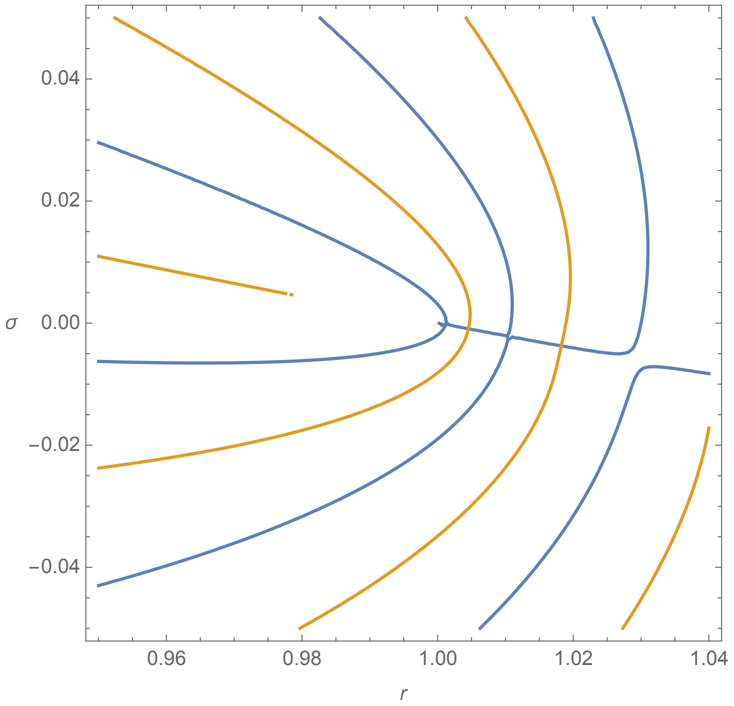

Figure 4.8: Contour plot of (4.67) for $\theta = \frac{15\pi}{32}$.

---

[3] Mathematica

θ	r_c	L	M	M
$15\pi/32$	1.00755	$100/3$	150	500

Table 4.4: Constants used to generate the eigenvector $\boldsymbol{u}_*$ and $\phi(x)$ in figure 4.10.

$r_c^A(\theta)$.

In summary, the eigenvalue problem (4.53) for this case is solved by (4.61), for entangled values of θ, σ_I and r which determines $k_n(\theta, r, \sigma_I)$. To determine the constants $\{A, B, C, D\}$ we investigate the nullspace of M_I (4.63), where the entries of the eigenvector that corresponds to a almost zero eigenvalue defines the constants.

4.5.4 Case I: Comparing the numerical and analytical solutions

Now that we have established analytical expressions for the solution $\phi(x)$ and $r_c^A(\theta)$ we will take use of the numerical procedures to calculate the corresponding modes and $r_c^N(\theta)$ from the operator matrix $C(r, \theta)$ to test our numerical setup.

The critical parameter function $r_c(\theta)$

Both the numerically calculated $r_c^N(\theta)$, and the analytical $r_c^A(\theta)$ are depicted in figure 4.9, and as the figures states, the numerical and analytical solutions match for both θ-domains. By comparing the finite $r_c(\theta)$ in figure 4.9 with the infinite $r_c(\theta)$ depicted in figure 4.7, we observe that the nature of $r_c(\theta)$ appears to be the same for $\theta \in S_1$, and identical when $\theta \in S_{II}$.

The spatial modes

Applying the constants in table 4.4 results in the image of $\boldsymbol{u}_*$ and $\phi(x)$ depicted in figure 4.10. Since that r and θ are tuned such that the CPMLSHE are on the

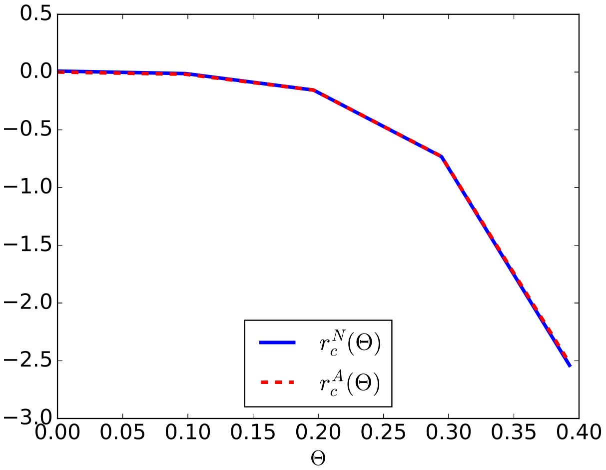

(a) Image of $r_c^N(\theta)$ and $r_c^A(\theta)$ for $\theta \in S_I$.

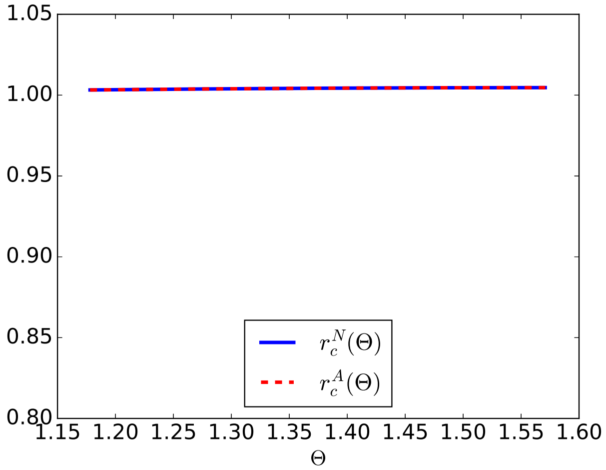

(b) Image of $r_c^N(\theta)$ and $r_c^A(\theta)$ for $\theta \in S_{II}$.

Figure 4.9: Image of the numerically calculated $r_c^N(\theta)$, and analytic $r_c^A(\theta)$ for the valid PML angles $S_I \cup S_{II}$.

onset of pattern formation, the figure illustrates the first unstable spatial mode of the finite CPMLSHE. As the figure states, both the numerical eigenvector and the analytical solution describes the same standing wave, even though the amplitudes are different due to unmatched scalings.

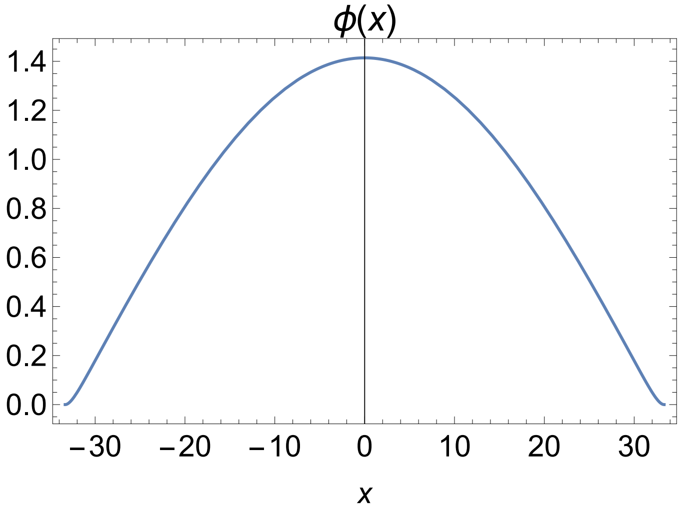

(a) The analytic solution $\phi(x)$ (2.5) for the finite CPMLSHE.

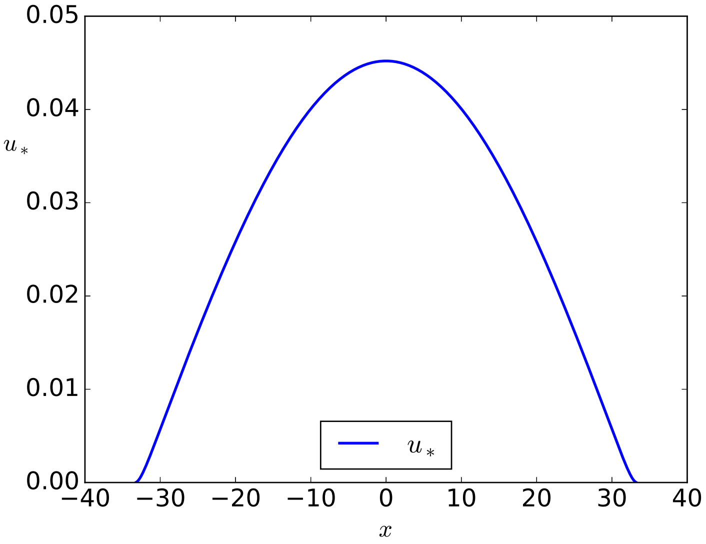

(b) The eigenvector $\boldsymbol{u}_*$ of $C(r, \theta)$ that corresponds to the eigenvalue λ_l with zero real part.

Figure 4.10: A standing spatial mode of the CPMLSHE on a finite domain for $\theta = \frac{15\pi}{32}$.

4.5.5 Case II: Analytics and numerics

In this case, the eigenfunction (4.54) results in the criteria equation

$$(1 - k^2 e^{-2i\theta})^2 = 0 \,, \tag{4.68}$$

with the corresponding solutions

$$k_1 = e^{i\theta} \tag{4.69a}$$
$$k_2 = -e^{i\theta} \,. \tag{4.69b}$$

The wavenumbers in (4.69) corresponds to a two termed linear combination

$$\phi(x) = A\phi_{k1}(x) + B\phi_{k2}(x), \tag{4.70}$$

which imply that the solution (4.70) is degenerated, since (4.53) is a fourth order problem. We must therefore modify our solution (4.70) to span the solution space of $\phi(x)$. As we always do in such situations, we make a qualified wild guess, and we suggest the modified solution

$$\phi(x) = Ax\phi_{k_1}(x) + Bx\phi_{k_2}(x) + C\phi_{k_1}(x) + D\phi_{k_2}(x) \,, \tag{4.71}$$

for each k_n in (4.69).

To justify the modification $x\phi_{k_n}(x)$, we must argue that the relation

$$(1 + e^{-2i\theta}\partial_{xx})^2 x\phi_{kn}(x) = 0 \tag{4.72}$$

holds for both k_n. Applying some algebra to the left hand side of (4.72) results in the relation

$$(1 + e^{-2i\theta}\partial_{xx})^2 x\phi_{k_n}(x) = e^{-4i\theta}\left(e^{2i\theta} - k_n^2\right)\left(k_n(4i - k_n x) + e^{2i\theta}x\right)\phi_{kn}(x) \,, \tag{4.73}$$

where the factor $\left(e^{2i\theta} - k_n^2\right)$ confirms (4.72) since it satisfies the relation

$$\left(e^{2i\theta} - k_n^2\right) = 0 \,, \tag{4.74}$$

for each k_n.

In order to proceed from here we ought to redo the calculations (4.62)-(4.63), but we will rather present the imminent calculations by words and precise hand waving.

Since k_1 and k_2 only depends on θ, the determinant is given by the relation

$$|M_I| = w(\theta) \ , \tag{4.75}$$

for fixed L, where $w(\theta) = w_R(\theta) + iw_R(\theta)$. In this case, we are left with two options:

1. Either $w(\theta) \neq 0 \ \forall \ \theta$, which imply that the only solution to the matrix system analogous to (4.62) for k_1 and k_2 is the non trivial, such that $\phi(x)$ (4.71) not defines a solution to the problem when $r = \sigma_R = 0$.

2. Alternatively, $w(\theta)$ forms a system of two equations and one unknown. This system might have solutions and corresponding spatial modes, but we will argue that these solutions and modes are of little interest to us: When $r = \sigma = 0$, the solution $\phi(x)e^{\sigma t}$ describes a time independent stationary mode, which not would generate any spatiotemporal behaviour. Since our analysis concerns modes on the onset of pattern formation, these modes are of little interest to us.

4.5.6 CPMLSHE summary

In this section we have established an analytic solution to the finite CPMLSHE, and we have produced the corresponding numerical solution from our implemented scheme. Furthermore, we have developed an algorithm that calculates the numerical $r_c^N(\theta)$, which is illustrated to produce the same results as the analytical function $r_c^A(\theta)$. We also note that the nature of the critical parameter function $r_c(\theta)$ is the same for both the finite and infinite CPMLSHE. This tells us that the numerical scheme and the developed procedures are correct, which we can use to determine $r_c(\theta)$ and spatial modes for the PMLSHE.

4.6 The linear PMLSHE revisited

Based on the discussions and results presented in section 4.2 - 4.5, we will continue our investigation of linear PMLSHE (3.23) under the assumption that the implemented numerical scheme (3.31) - (3.32) generates true solutions to the PMLSHE.

Our intention is to establish the nature of both $r_c(\theta)$ and the fastest growing spatial modes u_* the for fixed, corresponding r and θ values. By comparing the results from the eigenvalue analysis of the PMLSHE in section 4.2 with the different θ-domains for the CPMLSHE in section 4.4 and 4.5, we define the domains

$$I_1 = \left(0, \frac{4\pi}{32}\right) , \tag{4.76a}$$

$$I_2 = \left(\frac{4\pi}{32}, \frac{12\pi}{32}\right) , \tag{4.76b}$$

$$I_3 = \left(\frac{12\pi}{32}, \frac{16\pi}{32}\right) . \tag{4.76c}$$

To sustain readability, we discuss the critical parameter dependency and present images of the spatial modes in stand alone sections, while we discuss the established results in a summarizing section.

In order to generate the spatial modes on the onset of pattern formation for different θ, we must know corresponding r values, and must therefore start our investigation by establishing the nature of $r_c(\theta)$.

4.6.1 $\mathrm{r_c}(\theta)$ for the numeric PMLSHE

For the the PMLSHE and the corresponding SODM $M(r, \theta)$ (3.32) we recall the eigenvector and eigenvalue notation from the previous sections, and for a fixed θ_F we define the function

$$f_{\text{pmlshe}}(r) = \max_{\lambda_l} M(r, \theta_F) \tag{4.77a}$$

$$= \lambda_*[M(r, \theta_F)] . \tag{4.77b}$$

a	M_1	M_2	N_1	N_2	Δx_1	Δx_2	L
10	150	300	500	1000	$\frac{1}{15}$	$\frac{1}{30}$	100/3

Table 4.5

Furthermore we establish the root searching problem

$$f_{\text{pmlshe}}(r) = 0 \tag{4.78a}$$

$$r \in (a, b) \tag{4.78b}$$

$$f_{\text{pmlshe}}(a) < 0 < f_{\text{pmlshe}}(b) \ , \tag{4.78c}$$

which we can solve numerically for a suitable θ-grid to establish the function $r_c(\theta)$.

Based on the results in section 4.2 where λ_* varied with resolution, we are to calculate $r_c(\theta)$ for two different Δx. Applying the constants in table 4.5 results in the image of $r_c(\theta)$ depicted in figure 4.11 for $\Delta x_1 > \Delta x_2$. Note that the $r_c(\theta)$-axis is logarithmically scaled and that Δx_2 represents a doubling in precision relative to Δx_1.

Figure 4.11 clearly states that $r_c(\theta)$ varies with precision, and its nature differs for each region in (4.76):

- If $\theta \in I_1$, $r_c(\theta)$ is the approximately same for both resolutions.
- If $\theta \in I_2$, $r_c(\theta)$ varies extensively as a consequence of the increased resolution.
- If $\theta \in I_3$, $r_c(\theta)$ becomes significantly smaller as a consequence of the increased resolution.

If we combine this result for $r_c(\theta)$ for $\theta \in I_2$ with the plots of the grid levelled oscillating $\Psi(x, t)$ for $\theta = \frac{\pi}{8}$ in section 3.5, and the large λ_*-values for $\theta \in I_2$ in section 4.2, we are to conclude that $\theta \in I_2$ defines a ill posed problem for the PMLSHE, as also were the case for the CPMLSHE.

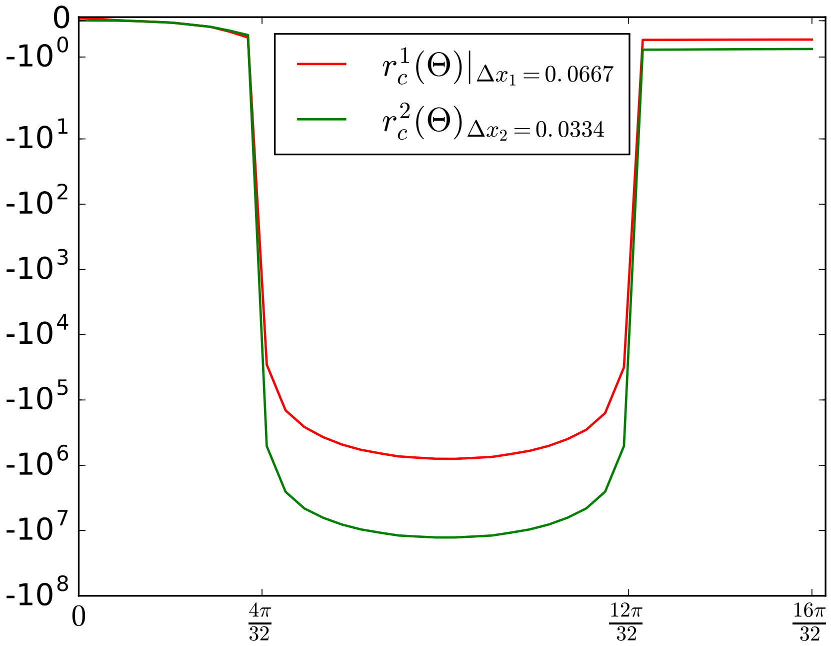

Figure 4.11: $r_c(\theta)$ for the PMLSHE for $\Delta x_1 = \frac{1}{15}$ and $\Delta x_2 = \frac{1}{30}$.

We will therefore exclude I_2 in the forthcoming analysis, while I_1 and I_3 are to be investigated further in order to determine the nature of $r_c(\theta)$ and the fastest growing modes of the PMLSHE. Before we proceed with our analysis, we recall the discretization and wavenumber-wavelenght relations stated in previous sections:

$$L = \frac{N}{M}a \,, \tag{4.79a}$$

$$\Delta x = \frac{a}{M} \,, \tag{4.79b}$$

$$\xi = \frac{2\pi}{k} \,. \tag{4.79c}$$

They require that the constants a, L, and the ratio $\frac{N}{M}$ must be the same for all numerical calculations of $r_c(\theta_F)$, in order to make the investigation useful. Since we have applied $a = 10$ and $L = \frac{100}{3}$ in all previous SHE and PMLSHE calculations, it is given that we apply those values in the forthcoming analysis.

In order to calculate the full $r_c(\theta)$ for higher resolutions, the algorithm that solves (4.78) becomes impractically computational intensive, since the dimension of the SODM grows as $(2N)^2$, and all eigenvalues of $M(r, \theta_F)$ must be calculated to determine the root of $f(r)$.

However, since $r_c(\theta)$ not varies with resolution for $\theta \in I_1$, and its nature is the same for both resolutions when $\theta \in I_3$, $r_c(\theta)$ should therefore vary equally for all θ_F in each region. We will therefore apply the angles

$$\theta_1 = \frac{3\pi}{32} \in I_1 \tag{4.80a}$$

$$\theta_3 = \frac{15\pi}{32} \in I_3 \tag{4.80b}$$

in the imminent calculations to determine the nature of $r_c(\theta)$ and the spatial modes u_*.

We define $r_c(M_{\theta=\theta_F})$ as a "function" of M gridpoints between the origin and the PML point for a fixed angle θ_F, and figure 4.12 illustrates the image of $r_c(M)$ for the angles θ_1 and θ_3 when $M \in (100, 700)$. Note that this notation only is useful in the context of figure 4.12; we are after all calculating how $r_c(\theta_1)$ and $r_c(\theta_3)$ varies with resolution.

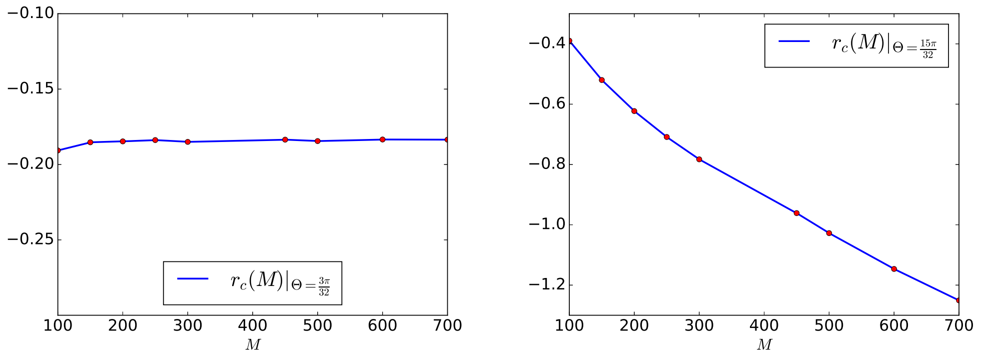

(a) How $r_c(\frac{3\pi}{32})$ varies with resolution. **(b)** How $r_c(\frac{15\pi}{32})$ varies with resolution.

Figure 4.12: How $r_c(\theta_F)$ for a fixed θ_F varies with increasing resolution.

The figures illustrates that $r_c(\theta_F)$ varies with with resolution in both θ-domains, but in opposite ways: $r_c(\theta_1)$ varies on the scale 10^{-3} at all resolutions except the smallest, and seems to converge to a negative and constant value, while $r_c(\theta_3)$ varies at the scale 10^1 and seems to slowly diverge. As we will discuss in a few paragraphs down the road, the implications of these results are possibly substantial for what concerns well posedness for the PMLSHE, but to investigate the results of figure 4.12 further we return to the function $f(r)$ (4.77).

We start by rewriting $f(r)$ as

$$\lambda_*(r) = \max_{\lambda_l} M(r, \theta_F)|_{\Delta x} \ , \tag{4.81}$$

which calculates the real maximum eigenvalue of the operator matrix $M(r, \theta_F)$ for a fixed θ_F at a given resolution Δx.

Figure 4.13 and 4.14 illustrates the image of $\lambda_*(r)$ for θ_1 and θ_3 respectively, where figure 4.13 is given by two subplots: one for the full r-domain, and one for smaller values in order to illustrate the nature of $\lambda_*(r)$. Both figures are generated with the resolutions $\Delta x = \{0.1, 0.067, 0.033, 0.022\}$, where $r \in (-3, 3)$. Note that the zeros of (4.81) marked as black dots in figure 4.13 and 4.14 corresponds to the red points in figure 4.12, and that the vertical stippled line at $r = 0.5$ represents the parameter value r we applied in our numerical calculations in section 3.5.

The figures 4.13 - 4.14 states the image of $\lambda_*(r)$ as straight lines for the given values of r. We remark that we have calculated $\lambda_*(r)$ for both θ_1 and θ_3 with the precision $\Delta x = 0.1$ for the larger interval $r \in (-50, 50)$, and the result was the same straight lines as depicted in the figures.

Now that we have established the nature of $r_c(\theta)$, and how it varies with resolution, we are to investigate the spatial modes on the onset of pattern formation to hopefully gain more information about the PMLSHE.

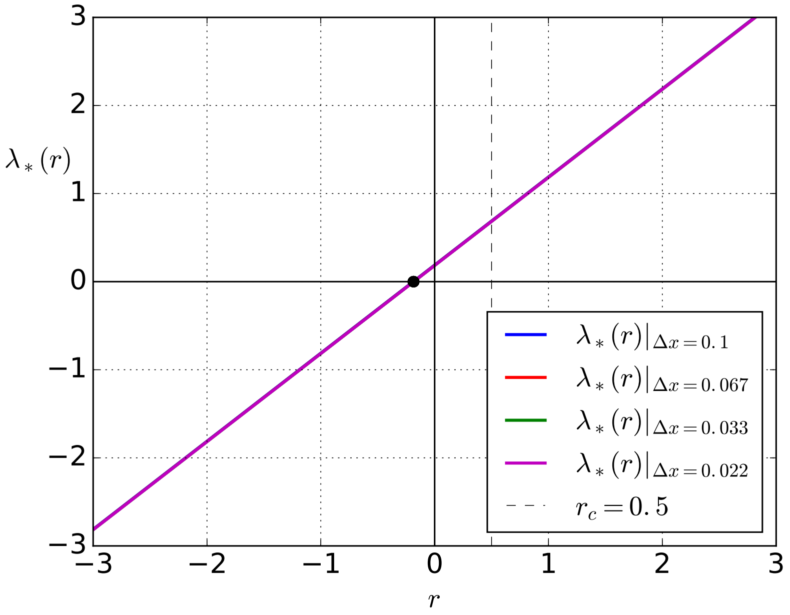

(a) How $\lambda_*(r)$ at $\theta = \frac{3\pi}{32}$ varies with resolutions.

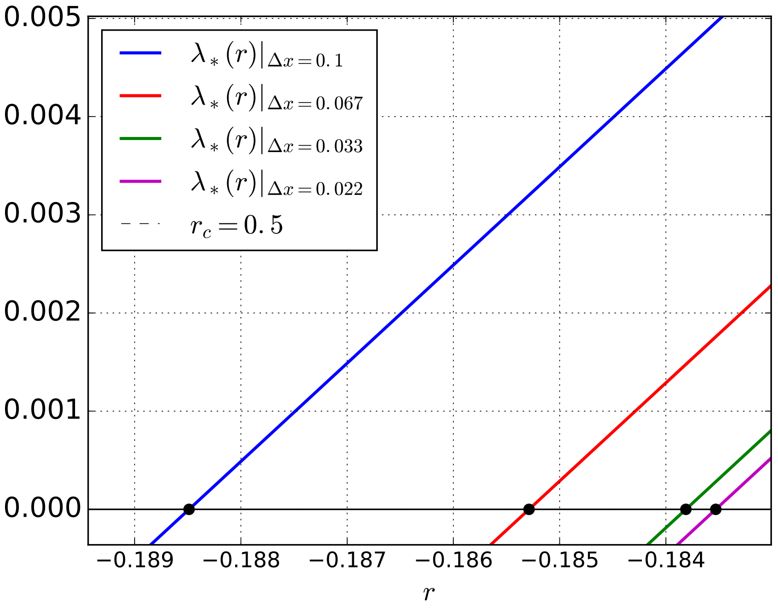

(b) How $\lambda_*(r)$ at $\theta = \frac{3\pi}{32}$ varies with resolutions for smaller values of r.

Figure 4.13: How $\lambda_*(r)$ at $\theta = \frac{3\pi}{32}$ varies with resolutions.

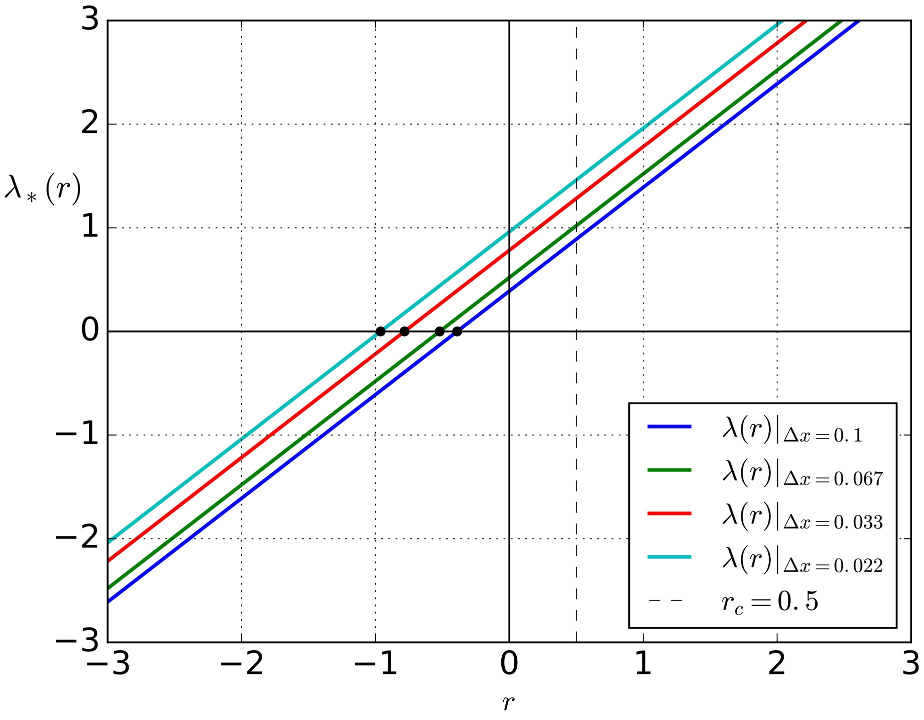

Figure 4.14: How $\lambda_*(r)$ at $\theta = \frac{15\pi}{32}$ varies with resolutions.

4.6.2 Eigenmodes for the numeric PMLSHE

We recall that the eigenvector $\boldsymbol{u}_*$ of $M(r,\theta)$ that describes the fastest growing mode on the onset of pattern formation is found from corresponding r and θ values determined by $r_c(\theta)$ since $\lambda_* \approx 0$ for those values.

Figure 4.15 to 4.17 illustrates $\boldsymbol{u}_*$ for three different θ, one from each defined domain in (4.76). All modes are normalized and generated for decreasing Δx. The modes in figure 4.15 and 4.17 corresponds to θ_1 and θ_3 respectively, while $\theta_2 = \frac{16\pi}{32}$ is used to generate the modes in figure 4.16. If we compare $\boldsymbol{u}_*$ from each domain with the solutions of $\Psi(x,t)$ in section 3.5, we observe that the modes explain much of the observed behaviour of $\Psi(x,t)$ for large t.

If we compare the corresponding modes in each domain, we note that $\boldsymbol{u}_*$ for

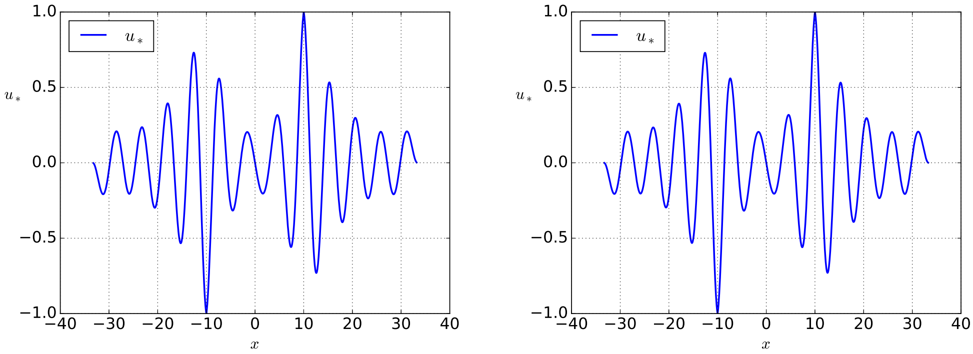

(a) u_* for $\Delta x = \frac{1}{15}$ when $\theta = \theta_1$.

(b) u_* for $\Delta x = \frac{1}{30}$ when $\theta = \theta_1$.

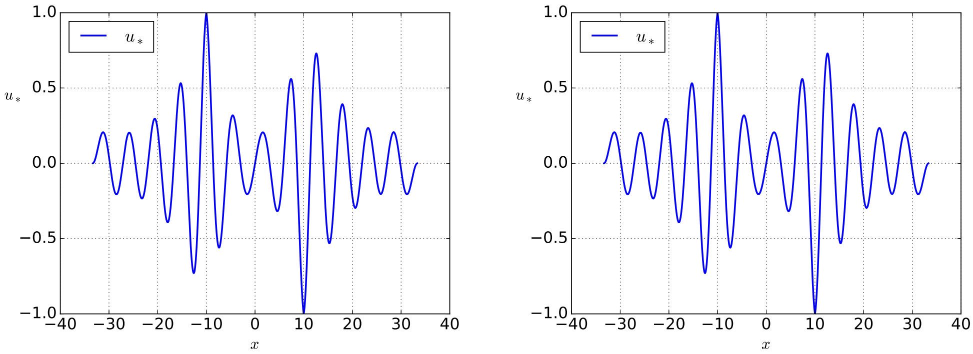

(c) u_* for $\Delta x = \frac{1}{50}$ when $\theta = \theta_1$.

(d) u_* for $\Delta x = \frac{1}{70}$ when $\theta = \theta_1$.

Figure 4.15: u_* on the onset of pattern formation for θ_1 for different resolutions.

$\theta \in I_1$ has some growing behaviour at the PML points, but does not seem to vary with resolution. The modes for $\theta \in I_2$ describes grid levelled oscillations for both depicted resolutions, which supports our previous claim of a ill posed PMLSHE for those θ. u_* for $\theta \in I_3$ clearly changes nature with resolution, and the modes attain δ function similar behaviour around the PML points. Note that this behaviour seems to tighten as the resolution decreases.

In the presented qualitative analysis of u_* we have strengthened our allegation of a ill posed PMLSHE for $\theta \in I_2$, but in order to determined posedness for the other regions we return to $r_c(\theta)$ and the results obtained in figure 4.12.

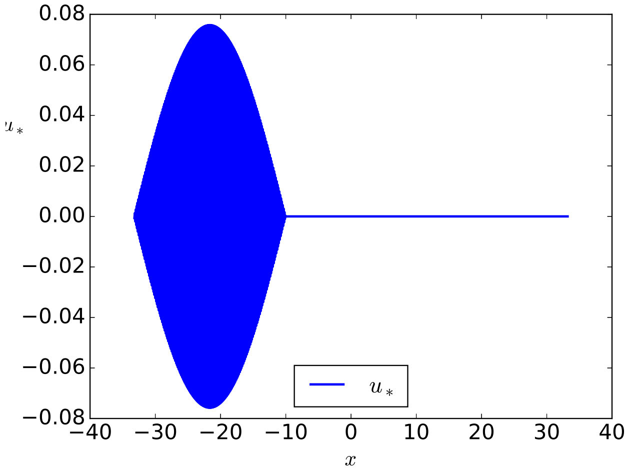

(a) $\boldsymbol{u}_*$ for $\Delta x = \frac{1}{30}$ when $\theta = \theta_2$.

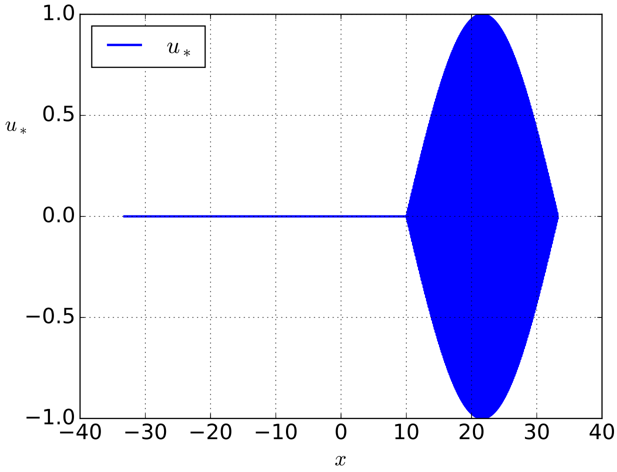

(b) $\boldsymbol{u}_*$ for $\Delta x = \frac{1}{70}$ when $\theta = \theta_2$.

Figure 4.16: $\boldsymbol{u}_*$ on the onset of pattern formation for θ_2 for different resolutions.

4.6.3 A conjecture

As stated in section 4.6.1, the behaviour of $r_c(\theta)$ depicted in figure 4.12 may reveal details concerning the posedness of the PMLSHE for θ in the regions I_1 and I_3. To argue why, recall the figures 4.13 - 4.14 which describe the image of the real maximum eigenvalue λ_* as a function of control parameters for different resolutions, and the MOL formulation of the linear PMLSHE

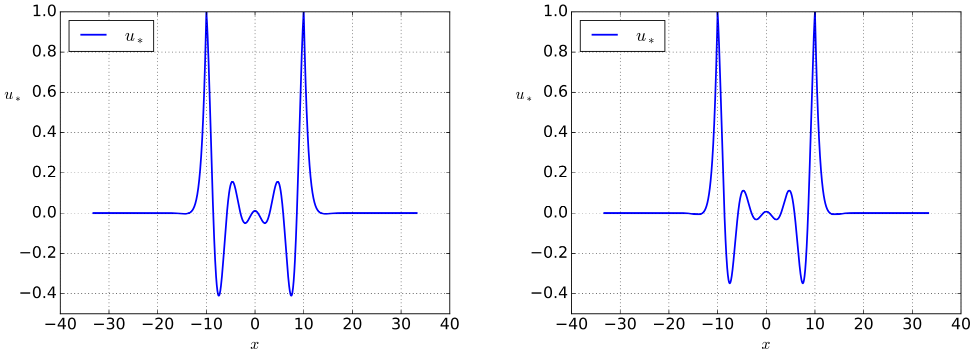

(a) $\boldsymbol{u}_*$ for $\Delta x = \frac{1}{15}$ when $\theta = \theta_3$.

(b) $\boldsymbol{u}_*$ for $\Delta x = \frac{1}{30}$ when $\theta = \theta_3$.

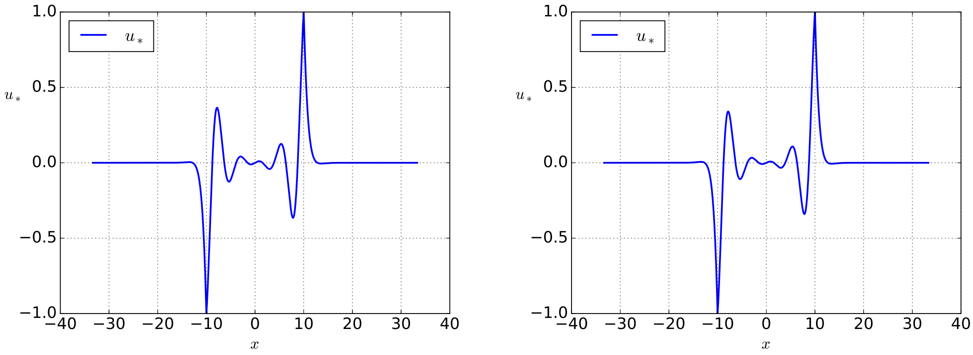

(c) $\boldsymbol{u}_*$ for $\Delta x = \frac{1}{50}$ when $\theta = \theta_3$.

(d) $\boldsymbol{u}_*$ for $\Delta x = \frac{1}{70}$ when $\theta = \theta_3$.

Figure 4.17: $\boldsymbol{u}_*$ on the onset of pattern formation for θ_1 for different resolutions.

(4.1) - (4.3). We also remark that r_c for the standard SHE is given by $r_c = 0$, and our intention were to run the PML system with $r > 0$ in order to generate spatiotemporal behavior, while the solutions were supposed to decay exponentially from the PML points and into the PML region.

Figure 4.13 indicates that $r_c(\theta)$ for $\theta \in I_1$ converges as the resolution increases. In that manner, there are two alternatives: $r_c(\theta)$ may converge to a small negative value r_n, or a positive value r_p.

- If $r \to r_n$ as $\Delta x \to 0$, the PML would be of no use to us, since we want to run the system for $r > 0$. Modes located inside the PML region would grow when we stress the system for positive r, which violates one of the intentions of introducing a PML.

- If $r \to r_p$ as $\Delta x \to 0$, the PML would apply for $0 < r < r_p$ since modes outside the PML region will grow and generate spatiotemporal behaviour, while modes located inside the PML region would decay and go to zero. However, this PML is also of no use to us, since it violates the intention of reduced computational time: If $\Delta x \to 0$, the gridpoint number M must be very large, and in that case, the operator matrix becomes very large, which imply that nothing is gained in terms of computational time.

Figure 4.14 indicates that $r_c(\theta)$ for $\theta \in I_3$ diverges such that $r_c(\theta) \to -\infty$ as $\Delta x \to 0$. If $r_c(\theta)$ actually diverges, it would state that $\lambda_* \to \infty$ as $\Delta x \to 0$. This imply that small initial data would generate infinity large derivatives at the instant when $t > 0$, which leads to an ill posed problem. If $r_c(\theta)$ not diverges, but rather converges to a negative value $r_c(\theta) \to r_n$, the argument in the top bullet point above applies, and the PML is again of no use.

Based on presented discussion, we are to state the following conjecture: A contour based PML is ill posed for the SHE if $\theta > \frac{\pi}{8}$, and well posed for $0 < \theta < \frac{\pi}{8}$.

5

Concluding remarks

5.1 Concluding remarks

The sole intention of this thesis were to apply a PML to a pattern generating model equation in order to save computational time, and eliminate boundary effects. We chose to work with the Swift-Hohenberg equation, but after thorough numerical and analytical examination, it turns out that we simply chose the wrong equation to apply a PML to.

In the first part of the thesis we introduced numerical and mathematical concepts, where the aim of the discussion were to establish a procedure on how to implement a numerical PML scheme to a general PDE, which in turn resulted in the PMLSHE.

The numerical simulations of the PMLSHE turned out to not produce the desired PML behaviour, and we began our investigations by postulating that the undesirable results could be a consequence of either implementation errors, ill posedness of the PMLSHE, or an unstable PML scheme due to the

MOL discretization.

In our investigations we performed the following: an eigenvalue analysis of the PMLSHE, a numerical eigenvalue perturbation method for the standard SHE with a small PML correction, an analytical analysis of the infinite CPMLSHE, a comparative numerical and analytical analysis of the finite CPMLSHE, and a numerical analysis of the PMLSHE.

Both the numerical eigenvalue perturbation method of the PML correction to the standard SHE, and the analytical calculations of the CPMLSHE indicated that the PMLSHE could be ill posed. Since the numerical and analytical comparative analysis of the CPMLSHE gave equal results, we were to trust our numerical scheme and the developed procedures. Based on these analysis we were to rule out implementation errors as the decisive reason for the undesired behaviour of PMLSHE. The final analysis of the PMLSHE illustrated that the problem is either ill posed, or of little relevance, depending on the angle given by the complex contour based PML.

5.2 Future work

As for the Swift-Hohenberg equation, we would suggest that the idea of a fully functioning PML should be abandoned, and we recommend readers not to follow the path we have laid out in this thesis. One might try to prove or disprove existence of PML solutions for $\theta \in (0, \frac{\pi}{8})$ analytically, but this problem is of little interest since nothing is gained in terms of reduced computational time, thereby violating the intention of a PML.

However, the PML is demonstrated apply to the rSE, and the sciences are filled with a wide range of PDEs where the PML-concept is useful to apply. As for pattern equations, the natural next step might be to investigate the one dimensional complex GLE (1.3) using the tools and concepts presented in this thesis.

A

Testing differential operators on a PML

Where the MOL is a clever way of transforming a PDE into a system of ODEs, a possible pitfall of the routine is that it utterly depends on the numeric differential operator implementation. One must therefore check the established operators, and a naive - but reliable way - to do so is by a visual comparison of the analytic derivative versus the numeric. The procedure is straight forward: pick a function $f(x)$ that is continuous up to the order of the differential operator $\mathcal{L}$, and plot the numeric derivative $\mathcal{L}_{\text{numeric}} f(x_i)$ against the analytic $\mathcal{L}_{\text{analytic}} f(x_i)$. If they match for a wide range of different functions with different behaviour, one can assume that the numeric approximation is fairly good. There are other tests and routines one can preform(different norms, conditional numbers, and so on), but those are not of our interest in this thesis.

a	M	n	Δx
5	50	20	0.1

Table A.1: Applied discretization constants to $\mathcal{D}_2(\theta)$ and $\mathcal{D}_4(\theta)$.

In the following figures, the operators $\mathcal{D}_2(\theta)$ and $\mathcal{D}_4(\theta)$, as used in the PML versions of the SHE (3.23) and rSE (2.64), are tested for the functions

$$f_1(x) = sin(x) \tag{A.1a}$$

$$f_2(x) = e^{i\frac{x^2}{10}} . \tag{A.1b}$$

They are tested relative to the contour $z(x)$ (2.51), and for different θ. We remark that if $\theta = 0$, $\mathcal{D}_2(\theta)$ and $\mathcal{D}_4(\theta)$ should produce the standard numerical second and forth derivative of $f(x)$. All plots are generated relative to the discretization (2.67), using the constants in table A.1. Note that Δx in these plots are bigger than the resolution we used to solve the PML versions of the SHE and rse, such that they are in many ways more inaccurate.

As we see in the figures A.1 - A.12, the oscillatory and spiky behaviour of the functions are well preserved. The derivatives are tested on other not included functions and resolutions, but the result is general the same. From this we can conclude that the numerical derivatives are good approximations to the analytical ones.

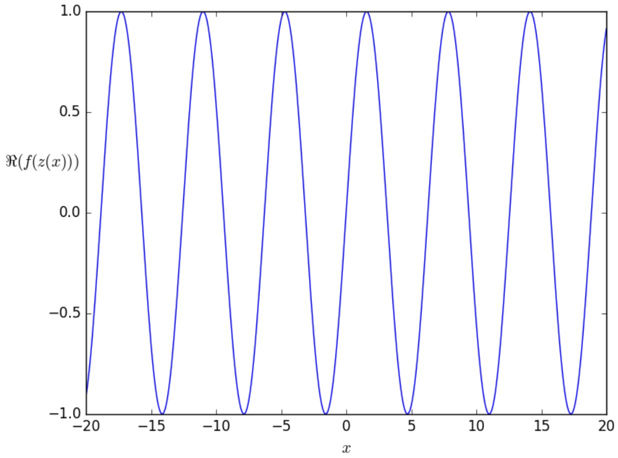

Figure A.1: $sin(z(x))$ and $\theta = 0$

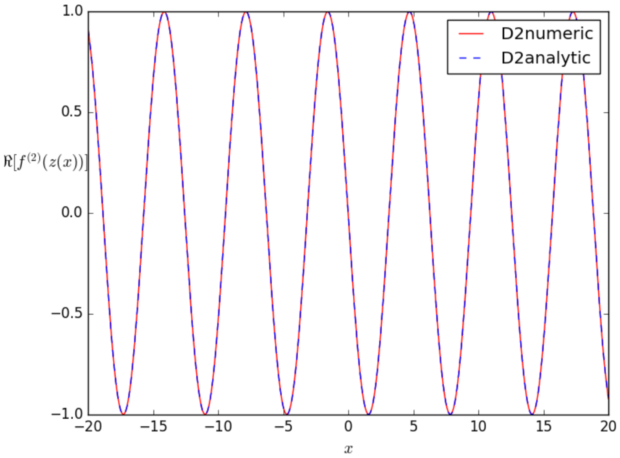

Figure A.2: $\mathcal{D}_2 sin(z(x))$ and $\theta = 0$

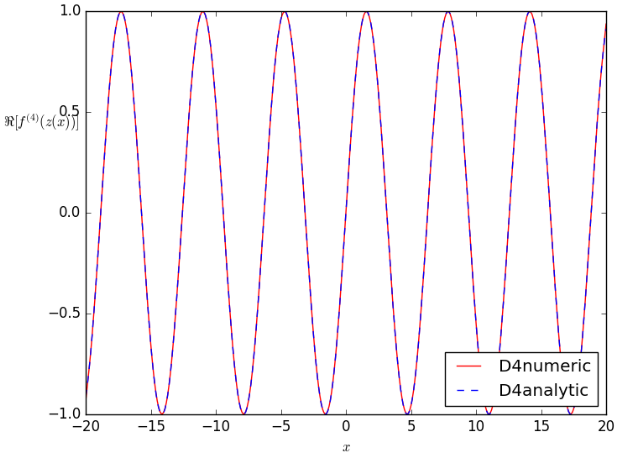

Figure A.3: $\mathcal{D}_4 sin(z(x))$ and $\theta = 0$

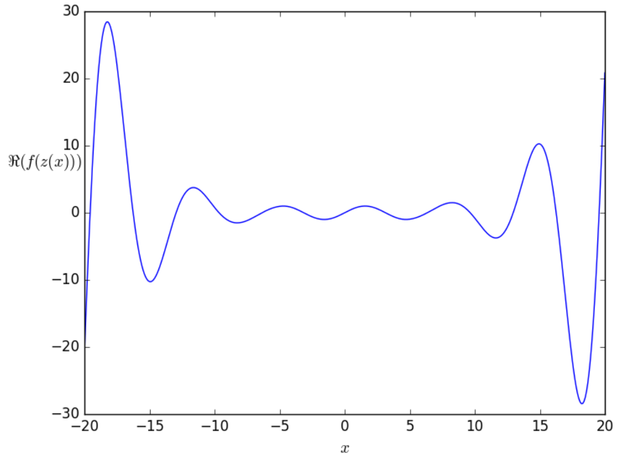

Figure A.4: $sin(z(x))$ and $\theta = \frac{\pi}{10}$

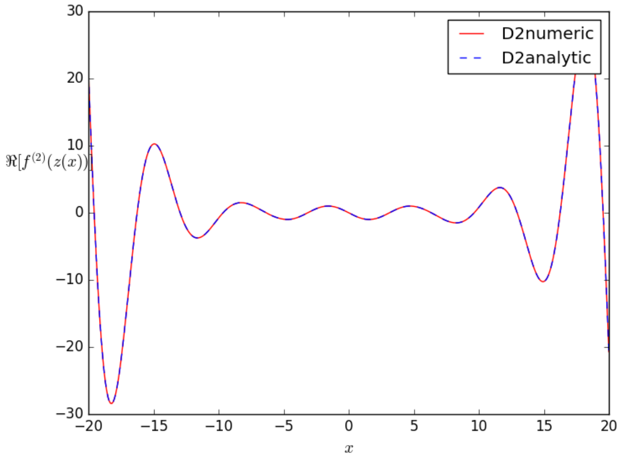

Figure A.5: $\mathcal{D}_2 sin(z(x))$ and $\theta = \frac{\pi}{10}$

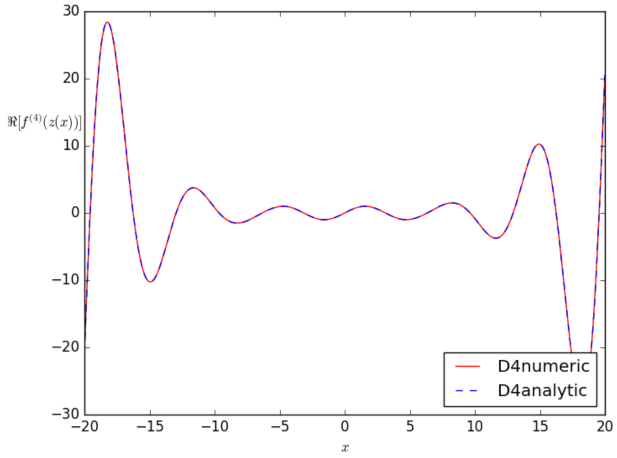

Figure A.6: $\mathcal{D}_4 sin(z(x))$ and $\theta = \frac{\pi}{10}$

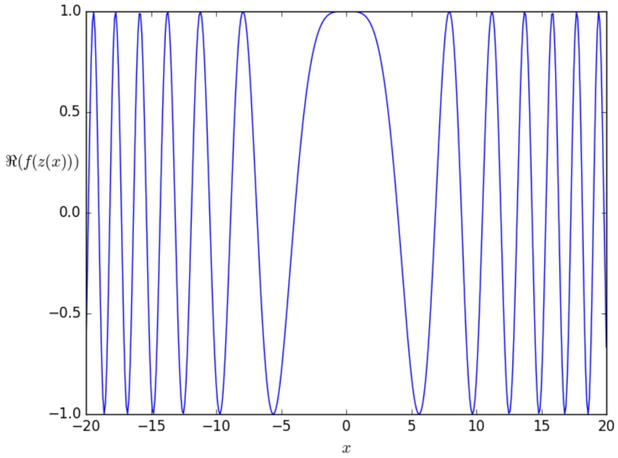

Figure A.7: $e^{i\frac{x^2}{10}}$ and $\theta = 0$

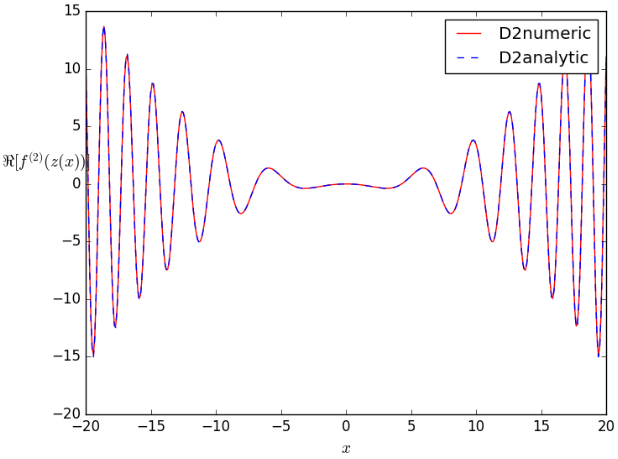

Figure A.8: $\mathcal{D}_2 e^{i\frac{x^2}{10}}$ and $\theta = 0$

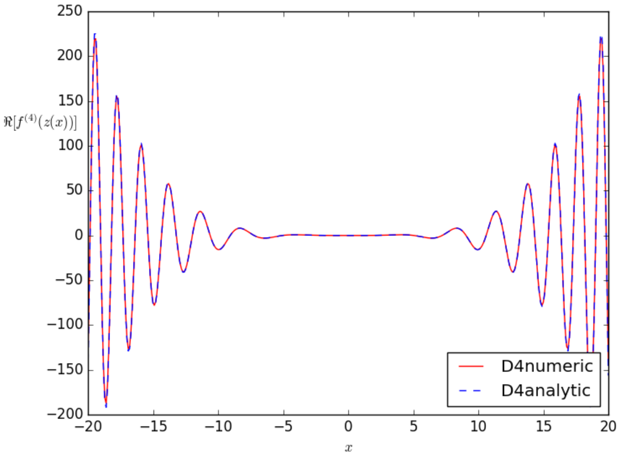

Figure A.9: $\mathcal{D}_4 e^{i\frac{x^2}{10}}$ and $\theta = 0$

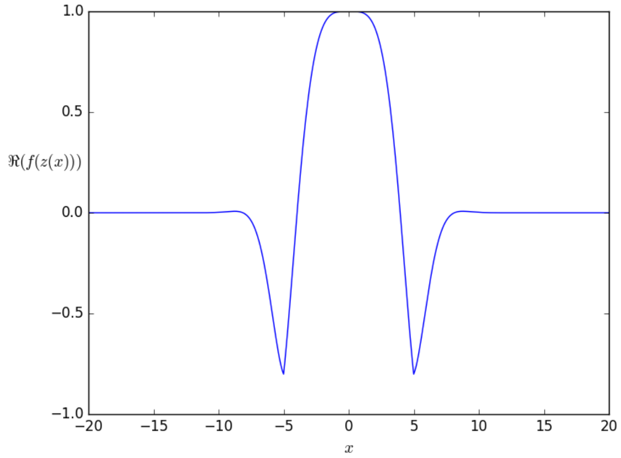

Figure A.10: $\left[e^{i\frac{x^2}{10}}\right]$ and $\theta = \frac{\pi}{4}$

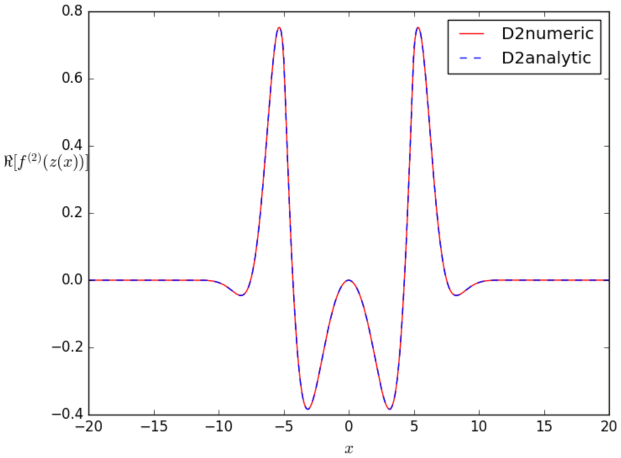

Figure A.11: $\mathcal{D}_2\left[e^{i\frac{x^2}{10}}\right]$ and $\theta = \frac{\pi}{4}$

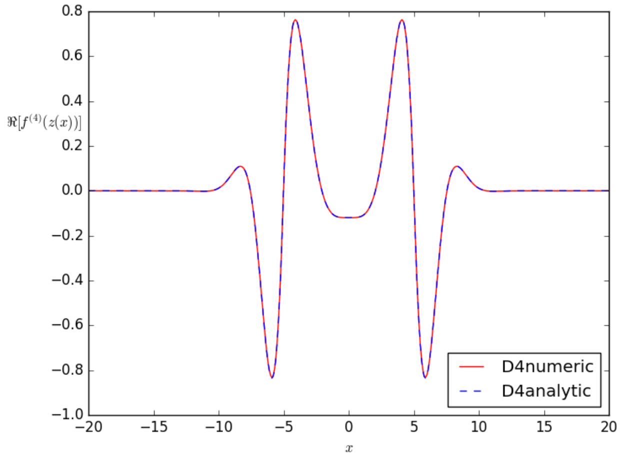

Figure A.12: $\mathcal{D}_4\left[e^{i\frac{x^2}{10}}\right]$ and $\theta = \frac{\pi}{4}$

B

Well posed partial differential equations

For a PDE with given initial and boundary data to model a physical system, or to give mathematical sense, the equation must fulfill some criteria. In general those read:

- The problem must have at least one solution.
- The problem must at most have one solution.
- The solution must depend in a continuous way on the data related to problem. Small data must thereby produce a small corresponding solution.

By data we mean parameters occurring in the PDE, description of boundary curves, and the functions that describe the boundary and initial data. We are to discuss the last criteria, and we will in this section we analyse an equation on the form

$$Au_{xx} + 2Bu_{xt} + Cu_{tt} + Du_x + Eu_t + Fu = 0 \ , \tag{B.1}$$

where the constants $A, \ldots, F$ are real. Aspects of the imminent conclusions for the equation (B.1) can be extended to a other equations [8], hereby the PML version of the SHE.

We assume normal mode solutions of (B.1) on the form

$$u(x,t) = a(k)e^{ikx+\sigma(k)t} \ . \tag{B.2}$$

By the principle of superposition, several normal modes can be added together for continuous k or discrete k_j to obtain the

$$u(x,t) = \sum_{j=-\infty}^{\infty} a(k_j)e^{ik_jx+\sigma(k_j)t} \tag{B.3}$$

$$u(x,t) = \int_{-\infty}^{\infty} dka(k)e^{ikx+\sigma(k)t} \tag{B.4}$$

Fourier series and Fourier transform respectively.

Inserting the normal mode (B.2) into the equation (B.1) results in the relation

$$C\sigma^2(2ikB + e)\sigma + (iDk + F - Ak^2) = 0 \ , \tag{B.5}$$

where σ denotes $\sigma(k)$. A normal mode solution can only exist if (B.5) is satisfied. (B.5) has two complex solutions, where we for each of those can denote its solution

$$\sigma(k) = \mathcal{R}[\sigma(k)] + i\mathcal{I}[\sigma(k)] \ , \tag{B.6}$$

and the corresponding normal mode as

$$u(x,t) = a(k)e^{\mathcal{R}[\sigma(k)]t}e^{i(kx+\mathcal{I}[\sigma(k)]t} \ . \tag{B.7}$$

By assuming that the mode amplitude $|a(k)|$ is bounded, the growth of $|u(x,t)|$ is thereby determined by $\mathcal{R}[\sigma(k)]$. To determine the outcome of this scheme is straight forward: either $\mathcal{R}[\sigma(k)]$ is bounded $\forall\ k \in \mathbb{R}$, or it is not. We define

$$\Omega = \sup_{k\in\mathbb{R}} \mathcal{R}[\sigma(k)] \tag{B.8}$$

as the maximal value of $\sigma(k)\ \forall k$.

If $\mathcal{R}[\sigma(k)]$ is unbounded such that $\Omega = \infty$, we let $a(k) = \frac{1}{\sigma^2(k)}$ and consider the initial value problem for the normal mode with data at $t = 0$, on the form

$$u(x,0) = \frac{e^{ikx}}{\sigma^2(k)} \tag{B.9a}$$

$$u_t(x,0) = \frac{e^{ikx}}{\sigma(k)}\ . \tag{B.9b}$$

Since $\mathcal{R}[\sigma(k)]$ is unbounded, there exist values of k such that $|u(x,0)|$ and $|u_(x,0)|$ are as small as we like. Hence, these data impose an arbitrarily small initial value problem. However, the mode

$$|u(x,t)| = |a(k)|e^{\mathcal{R}[\sigma(k)]t} \tag{B.10}$$

grows exponentially as a function of k, and can for any fixed $t > 0$ be made as large as desired due to the fact that an exponential growth grows faster than a second order algebraic decay. Hence, arbitrarily small data can be made arbitrarily large for any $t > 0$. Our third criteria for well posed PDE problems are thereby not satisfied, and imply a ill posed problem.

/C

Discrete Fourier Transform

C.1 Matching the continuous Fourier transform with the one defined in the Python programming language

One of the numerous ways[1] one can define the Fourier transform and its inverse is the following:

$$F(\lambda) = \frac{1}{\sqrt{2\pi}} \int_{\mathbb{R}} \mathrm{d}x \; f(x) e^{-i\lambda x} \tag{C.1}$$

$$f(x) = \frac{1}{\sqrt{2\pi}} \int_{\mathbb{R}} \mathrm{d}\lambda \; F(\lambda) e^{i\lambda x} \, . \tag{C.2}$$

---

[1] There are different conventions for where one got the normalization factor and a minus sign in one of the exponents, but it does not matter as long as the transform of the either gives the other under the L^2 inner product $\langle f(x), g(x) \rangle_{L^2} = \int_D \mathrm{d}\mu \; f(x)\overline{g(x)}$

By introducing the discrete Fourier transform (DFT)

$$v_s = \frac{1}{\sqrt{n}} \sum_{r=0}^{n-1} u_r e^{-2\pi i \frac{rs}{n}} \qquad s = 0, 1, \ldots, n-1 \tag{C.3}$$

and its inverse, the inverse discrete Fourier transform (IDFT)

$$u_r = \frac{1}{\sqrt{n}} \sum_{s=0}^{n-1} v_s e^{2\pi i \frac{rs}{n}} \qquad r = 0, 1, \ldots, n-1 \tag{C.4}$$

as defined in the Python programming language, we want to get the definition of the Fourier transform (C.1) and its inverse (C.2) on the form of (C.3) and (C.4). We remark that the imminent calculations are based on the notes in [4], but that our calculations are based on the Python programming language, contrary to the Mathematica-based original notes.

To manage this we start by introducing a discretization for the domain axes

$$\alpha_j = (j - \tfrac{1}{2})\Delta x \qquad \text{for } j \in \mathbb{Z} \tag{C.5a}$$

$$\beta_l = (l - \tfrac{1}{2})\Delta \lambda \qquad \text{for } l \in \mathbb{Z}\ , \tag{C.5b}$$

where the relations

$$\alpha_{j+1} - \alpha_j = \Delta x \tag{C.6a}$$

$$\beta_{l+1} - \beta_l = \Delta \lambda \tag{C.6b}$$

are obtained. With (C.5) we define another set of discretizations for our domain axes

$$x_j = \frac{1}{2}(\alpha_{j+1} + \alpha_j) \tag{C.7a}$$

$$\lambda_l = \frac{1}{2}(\lambda_{l+1} + \lambda_l)\ , \tag{C.7b}$$

where we observe that

$$x_j = j\Delta x \tag{C.8a}$$

$$\lambda_l = l\Delta\lambda\ . \tag{C.8b}$$

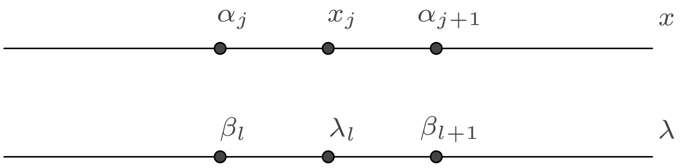

Figure C.1: A discretization for the Fourier domains

With this machinery in hand we have the picture as seen in figure C.1 for the domain axes. Applying the midpoint rule together with the integrals (C.1) and (C.2) our transforms turn into

$$\begin{aligned} F(\lambda) &= \frac{1}{\sqrt{2\pi}} \sum_{j=-\infty}^{\infty} \int_{\alpha_j}^{\alpha_{j+1}} \mathrm{d}x \; f(x) e^{-i\lambda x} \\ &\approx \frac{\Delta x}{\sqrt{2\pi}} \sum_{j=-\infty}^{\infty} f(x_j) e^{-i\lambda x_j} \end{aligned} \tag{C.9}$$

$$\begin{aligned} f(x) &= \frac{1}{\sqrt{2\pi}} \sum_{l=-\infty}^{\infty} \int_{\beta_l}^{\beta_{l+1}} \mathrm{d}\lambda \; F(\lambda) e^{i\lambda x} \\ &\approx \frac{\Delta \lambda}{\sqrt{2\pi}} \sum_{l=-\infty}^{\infty} F(\lambda_l) e^{i\lambda_l x} \; . \end{aligned} \tag{C.10}$$

To implement (C.9) and (C.10) on a computer, we need to truncate the series. By assuming that

$$F_l \equiv F(\lambda_l) \approx 0 \quad \text{for } |\mathrm{l}| > \mathrm{N} \tag{C.11a}$$

$$f_j \equiv f(x_j) \approx 0 \quad \text{for } |\mathrm{j}| > \mathrm{N} \tag{C.11b}$$

we can truncate the series (C.9) and (C.10) for some N such that the expressions for $F(\lambda)$ and $f(x)$ becomes

$$F(\lambda) = \frac{\Delta x}{\sqrt{2\pi}} \sum_{j=-N}^{N} f_j e^{-i\lambda x_j} \tag{C.12}$$

$$f(x) = \frac{\Delta \lambda}{\sqrt{2\pi}} \sum_{l=-N}^{N} F_l e^{i\lambda_l x} \; . \tag{C.13}$$

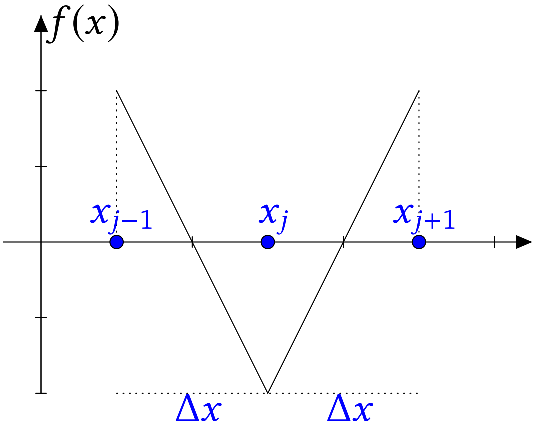

Figure C.2: Discretized spatial domain

This approximation demands certain assumptions and needs to made valid on the grids. In (C.13) we have approximated $f(x)$ with a periodic function where the largest and shortest periods are given by

$$P_{max} = \frac{2\pi}{\lambda_1} = \frac{2\pi}{\Delta\lambda} \tag{C.14a}$$

$$P_{min} = \frac{2\pi}{\lambda_N} = \frac{2\pi}{N\Delta\lambda} \ . \tag{C.14b}$$

This we need to match against our x_j grid, and from figure C.2 we have that the shortest possible period on the x_j grid is $2\Delta x$. That leads to the relation

$$2\Delta x \leq P_{min} \Longleftrightarrow \Delta x \leq \frac{\pi}{N\Delta\lambda} \tag{C.15}$$

where the optimal choise is $\Delta x\Delta\lambda = \frac{\pi}{N}$. Now $f(x)$ is well represented on the gridvalues x_j, and with the same argument as above $F(\lambda)$ is also defined on the grid λ_l. This leads to the expressions

$$F_l = \frac{\Delta x}{\sqrt{2\pi}} \sum_{j=-N}^{N-1} f_j e^{-i\pi\frac{jl}{N}} \quad \text{for } l \in -N, \ldots, N-1 \tag{C.16}$$

$$f_j = \frac{\Delta\lambda}{\sqrt{2\pi}} \sum_{l=-N}^{N-1} F_l e^{i\pi\frac{jl}{N}} \quad \text{for } j \in -N, \ldots, N-1 \tag{C.17}$$

where we have changed the upper limit of the sum such that $N \to N-1$. That maneuver is kosher since we must have

$$F_{\pm N} \approx 0 \quad \text{and} \quad f_{\pm N} \approx 0 \tag{C.18}$$

for (C.16) and (C.17) to be a good approximation of (C.1) and (C.2), and thus no accuracy is lost if $N \to N-1$. These summation expressions begin to resemble the Python versions of DFT and IDFT, and by introducing the index relations

$$r = N + j \quad \text{for } j \in -N, \ldots, N-1 \tag{C.19a}$$

$$s = N + l \quad \text{for } l \in -N, \ldots, N-1 \tag{C.19b}$$

(C.16) and (C.17) turn into

$$F_{s-N} = \frac{\Delta x}{\sqrt{2\pi}} \sum_{r=0}^{2N-1} f_{r-N} e^{-i\pi\frac{(r-N)(s-N)}{N}} \tag{C.20}$$

$$f_{r-N} = \frac{\Delta\lambda}{\sqrt{2\pi}} \sum_{s=0}^{2N-1} F_{s-N} e^{i\pi\frac{(r-N)(s-N)}{N}} \ . \tag{C.21}$$

To get rid off the extra exponent terms we define the scalings

$$F_{s-N} = \alpha_s v_s \quad \text{and} \quad f_{r-N}\beta_r u_r \tag{C.22}$$

where the constants α_s and β_r are given by

$$\alpha_s = \alpha_0 e^{i\pi s} \quad \text{and} \quad \beta_r = \beta_0 e^{i\pi N} e^{-i\pi r} \ . \tag{C.23}$$

Inserting the scalings in (C.20) and (C.21) gives

$$v_s = \sum_{r=0}^{2N-1} u_r \frac{\beta_0 \Delta x}{\alpha_0 \sqrt{2\pi}} e^{-i\pi\frac{rs}{N}} \tag{C.24}$$

$$u_r = \sum_{s=0}^{2N-1} v_s \frac{\alpha_0 \Delta\lambda}{\beta_0 \sqrt{2\pi}} e^{i\pi\frac{rs}{N}} \ . \tag{C.25}$$

By making

$$\frac{\beta_0 \Delta x}{\alpha_0 \sqrt{2\pi}} = 1 \quad \text{and} \quad \frac{\alpha_0 \Delta \lambda}{\beta_0 \sqrt{2\pi}} = 1 \tag{C.26}$$

where the one could be turned into the other using the optimal relation from (C.15), and letting $n = 2N$ we have transformed (C.1) and (C.2) on the form of (C.3) and (C.4).

C.2 Testing the transform

To test the numerical transform we take the function

$$f(x) = x^2 e^{-x^2} , \tag{C.27}$$

and its corresponding analytic transform

$$\widehat{f}(k) = \int_{\mathbb{R}} x^2 e^{-x^2} e^{ikx} \mathrm{d} \tag{C.28a}$$

$$= -\frac{e^{-\frac{k^2}{4}} \left(k^2 - 2\right)}{4\sqrt{2}} , \tag{C.28b}$$

and plot the numerically calculated $\widehat{f}(k)$ against the analytic expression (C.28). As figure C.3 illustrates, the numeric and the analytic transform matches.

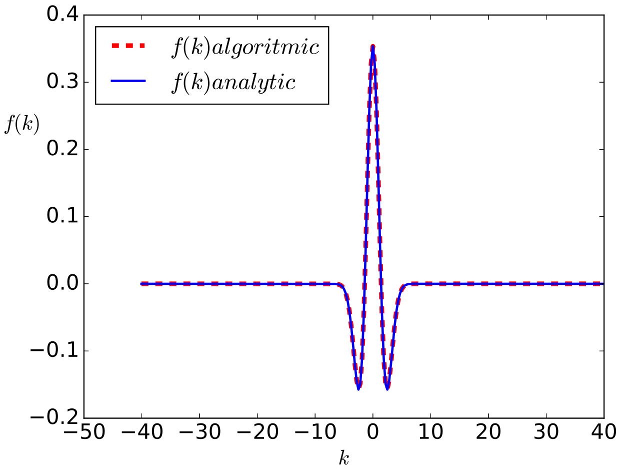

Figure C.3: Numerically tested, and analytically verified $\widehat{f(k)}$.

Bibliography

[1] Michael Cross and Henry Greenside. *Pattern formation and dynamics in nonequilibrium systems*. Cambridge University Press, 2009.

[2] Bengt Fornberg. Generation of finite difference formulas on arbitrarily spaced grids. *Mathematics of computation*, 51(184):699–706, 1988.

[3] Per Chr Hemmer. *Kvantemekanikk*. Tapir, 1985.

[4] Per Jacobsen. Lecture notes on the fourier transform. 2012.

[5] Steven G Johnson. Notes on perfectly matched layers (pmls), 2007.

[6] Timothy Sauer. *Numerical Analysis*, volume 2. Pearson, 2012.

[7] William E Schiesser and Graham W Griffiths. *A compendium of partial differential equation models: method of lines analysis with Matlab*. Cambridge University Press, 2009.

[8] Erich Zauderer. *Partial differential equations of applied mathematics*, volume 71. John Wiley & Sons, 2011.